Titre: Title:	Multi-Material Three-Dimensional Printing of Piezoelectric Devices for Sensing and Energy Harvesting Applications
Auteur: Author:	Rui Tao
Date:	2022
Type:	Mémoire ou thèse / Dissertation or Thesis
Référence: Citation:	Tao, R. (2022). Multi-Material Three-Dimensional Printing of Piezoelectric Devices for Sensing and Energy Harvesting Applications [Thèse de doctorat, Polytechnique Montréal]. PolyPublie. https://publications.polymtl.ca/10291/

URL de PolyPublie: PolyPublie URL:	https://publications.polymtl.ca/10291/
Directeurs de recherche: Advisors:	Daniel Therriault
Programme: Program:	PhD.

POLYTECHNIQUE MONTRÉAL

affiliée à l'Université de Montréal

MULTI-MATERIAL THREE-DIMENSIONAL PRINTING OF PIEZOELECTRIC DEVICES FOR SENSING AND ENERGY HARVESTING APPLICATIONS

RUI TAO

Département de génie mécanique

Thèse présentée en vue de l'obtention du diplôme de *Philosophiæ Doctor*

Génie mécanique

Mai 2022

POLYTECHNIQUE MONTRÉAL

affiliée à l'Université de Montréal

Cette thèse intitulée :

MULTI-MATERIAL THREE-DIMENSIONAL PRINTING OF PIEZOELECTRIC DEVICES FOR SENSING AND ENERGY HARVESTING APPLICATIONS

présentée par **Rui TAO**

en vue de l'obtention du diplôme de *Philosophiæ Doctor*

a été dûment acceptée par le jury d'examen constitué de :

Maksim SKOROBOGATIY, président
Daniel THERRIAULT, membre et directeur de recherche
Sampada BODKHE, membre
Sharmistha BHADRA, membre externe

DEDICATION

To everyone who supported me during my PhD.

ACKNOWLEDGEMENTS

I wish to thank all the people who are always here to help me and stay with me during my Ph.D. in Montreal, Canada.

First of all, I would like to express my special thanks to my supervisor Prof. Daniel Therriault for accepting me as his student and giving me such an interesting research topic. He kindly provided me with all the support for my study and life in Montreal. I have learned a lot of speaking, writing and researching skills from him. His serious and responsible academic attitude deeply influenced me. Also, he always cares more on students' physical and mental health than the scientific research achievements. I could not have accomplished my study without his patient guidance.

It was my great pleasure to work in such a harmonious lab - Laboratory for Multiscale Mechanics (LM^2). I would like to thank my co-worker Floriane Granier for her hardwork during the collaboration of two projects. I thank Rouhollah Farahani for providing me with constructive comments on my three papers. I thank Shibo Zou for giving me countless advice and help on my project and life all the time. I thank Kambiz Chizari, Mohammad Rafiee, Yanik Landry-Ducharme, Isabelle Nowlan, Somayeh Hossseini Rad, Benedict Besner, Nour Aimene and Fabrice Danet for their technical advice and support. I cherish the time spent with my colleagues: Hongqiu Wei, Qinghua Wu, Chao Xu, Sampada Bodhke, Ilyass Tabiai, Lachlan Leech, Filippo Lervolino, Audrey Diouf Lewis, Yahya Abderrafai, Juliette Pierre, Jean-François Chauvette, Lingyu Yue, Mohammadreza Moeini, Chi Zhang, Iee Lee Hia, Josué Costa Baptista, Olivier Duchesne, Paul Gregorio, David Brzeski, Alessandra Lingua, Facundo Sosa-Rey, Anamaria Serbescu, Ferran Santonja, Dogan Arslan, Etienne Gourcerol, Gabriel Chenier, Thibault Le Gentil, Mathieu Verville, David Brassard and Anton Trofimov.

I am thankful for the instrument and the lab access kindly provided by Prof. Martin Lévesque, Prof. Frederick Gosselin, Prof. Abdolhamid Akbarzadeh, Prof. Frédéric Sirois, Prof. Ajji, Abdellah, Prof. Mickael Begon and Prof. Sharmistha Bhadra. I thank Jiahao Shi, Matthieu Gauthier, Claire Cerclé,

Edith-Roland Fotsing, Richard Silverwood, Robert Delisle, Kiran Kumar Sappati, and Laurent Mouden for their technical advice and support. I thank Nadine Bernardini for her help on all the purchases.

Also, I thank Prof. Daniel Therriault and Mr. Martin Levesque for providing the opportunity to have a wonderful 8 months' internship at Hutchinson Montreal in 2020. It was a good experience working with my internship supervisor Mr. Linus Lehnert and all the colleagues there.

I acknowledge the financial support from National Science and Engineering Research Council (NSERC), the Department of National Defence (DND) and China Scholarship Council (CSC).

I shall also not forget the happy times I spent with my friends: Fan Zhang, Xin Zong, Lu Wang, Xiaoxuan Cao and Dingwen Zhang.

Finally, I am grateful to my whole family, my friends and my teachers in China and France for making me who I am today. I appreciate the happiness my cat Miracle brings me. A huge thank you to my beloved husband Thomas Sam-Yin-Yang for supporting me in the happy and hard times.

Sincerely,

Rui

RÉSUMÉ

Les matériaux piézoélectriques servent de transducteurs pour convertir linéairement l'énergie mécanique en énergie électrique, et vice versa. Sur la base de cette capacité, une variété de dispositifs piézoélectriques avec la géométrie, la performance et la fonction désirées ont été fabriqués pour des applications de détection, de récolte d'énergie et d'actionnement. Parmi eux, les dispositifs composites piézoélectriques tridimensionnels (3D) flexibles et conformes (particules céramiques hautement piézoélectriques comme charge; polymères flexibles comme matrice) sont très en demande dans de nombreux domaines tels que les peaux artificielles intelligentes, les capteurs et les collecteurs d'énergie portables sans-batterie, et la robotique flexible. Les méthodes conventionnelles de fabrication des dispositifs piézoélectriques, telles que le moulage en solution, l'enduction par centrifugation, l'extrusion par fusion et l'électrospinning, limitent la complexité des structures fabriquées. Ainsi, les techniques d'impression 3D, telles que l'écriture directe à l'encre (DIW), la stéréolithographie (SLA), le traitement numérique de la lumière (DLP) et la fabrication de filaments fondus (FFF) sont de plus en plus utilisées à cette fin.

En outre, pour établir la connexion électrique entre les structures piézoélectriques et les interfaces, une étape supplémentaire est généralement nécessaire pour ajouter des électrodes sur les structures piézoélectriques par peinture, pulvérisation et fixation de rubans ou de tissus conducteurs. L'émergence de la technique d'impression 3D multi-matériaux offre un moyen efficace de combiner les processus de fabrication de la structure piézoélectrique et des électrodes. L'objectif de cette thèse est de développer des dispositifs composites piézoélectriques flexibles 3D avec des électrodes pour des applications de détection piézoélectrique et de récolte d'énergie basées sur la technique d'impression 3D multi-matériaux.

Tout d'abord, pour trouver le matériau piézoélectrique le plus approprié pour le processus d'impression 3D multi-matériaux, nous avons imprimé des films de polyfluorure de vinylidène (PVDF) à partir du filament de PVDF disponible dans le commerce en utilisant une imprimante 3D FFF. Nous avons constaté que les films PVDF, tels qu'imprimés, ont une faible teneur en phase β électroactive (F_β) de 39%, il faut donc un processus de post étirement pour augmenter la F_β. Les films PVDF étirés et polarisés d'une dimension de 40 × 20 × 0,06 mm^3 (longueur × largeur × épaisseur) ont un coefficient piézoélectrique (d_{33}) de 7,29 pC/N et un F_β de 65 % à un rapport

d'étirement (R) de 4 après avoir été polarisés sous un champ électrique de 30 V/µm. Bien que le d_{33} résultant des films de PVDF fabriqués ait été considérablement amélioré de ~ 10-100 fois supérieur aux valeurs rapportées connexes, le processus d'étirement limite les possibilités de réaliser des géométries complexes avec le PVDF.

Par la suite, nous avons incorporé des nanoparticules de titanate de zirconate de plomb (PZT) hautement piézoélectriques dans une matrice flexible de polyuréthane thermoplastique (TPU) et extrudé le matériau composite en un filament imprimable par FFF (~1,75 mm). Le matériau composite piézoélectrique, TPU/30vol% PZT, développé présente un allongement à la rupture importante de ~56% et une valeur d_{33} de 6,8 pC/N après avoir été polarisé par les paramètres de polarisation appropriés. Une technique d'impression 3D multi-matériaux FFF a ensuite été utilisée pour fabriquer des treillis composites piézoélectriques flexibles 3D avec des électrodes à l'aide du filament composite piézoélectrique que nous avons développé et d'un filament composite conducteur (TPU/noir de carbone) disponible dans le commerce. Quatre types de réseaux composites piézoélectriques 3D: cubique simple (SC), cubique centré sur le corps (BCC), cuboctaèdre (CH) et treillis en octuple (OT) (et un solide entièrement dense (FD) comme référence) ont été conçus et fabriqués. Les performances piézoélectriques des treillis ont été comparées au moyen de méthodes expérimentales et d'analyse par éléments finis (FEA). Pour une même force de compression maximale, le réseau OT peut générer une tension de sortie environ deux fois supérieure à celle de l'échantillon FD. À titre de démonstration, une semelle de chaussure composite piézoélectrique OT originale et multi-matériaux peut générer une tension crête à crête élevée (V_{pp}) de ~20 V par le piétinement humain.

De plus, pour fabriquer des structures piézoélectriques flexibles de forme libre ou conforme, nous avons réalisé un processus d'impression 3D DIW multi-matériaux dans un fluide de support. Le fluide de support développé, composé d'huile minérale et de 6% (w/v) de silice pyrogénée, avec une limite d'élasticité appropriée, se comporte comme un fluide de Herschel-Bulkley. Pendant le processus d'impression, le réseau de silice fumée réticulée s'écoule temporairement sous la contrainte générée par le mouvement de l'aiguille de distribution, puis revient rapidement à l'état solide pour retenir l'encre déposée. Les compositions des encres sont les suivantes : polydiméthylsiloxane (PDMS)/30vol% de PZT pour l'encre composite piézoélectrique et PDMS/25vol% d'argent (Ag) pour l'encre composite conductrice. Une caractérisation complète des

propriétés des encres (c'est-à-dire les comportements piézoélectrique ou conducteur, les propriétés rhéologiques et mécaniques) et du comportement rhéologique du fluide de support avec les différentes compositions a été réalisée. Trois démonstrateurs : un film plan multicouche, un hémisphère non plan conforme et une structure 3D composée de six spirales imprimées verticalement entre deux couches hexagonales (spirale-hexagone de forme libre) ont été fabriqués et testés respectivement en tension ou en compression. Par exemple, en comprimant cycliquement la structure spirale-hexagone de forme libre à 8 Hz pendant plus de 800 cycles, un V_{pp} de 86.39 ± 1,145 mV a été obtenu, ce qui montre la bonne durabilité du capteur piézoélectrique spirale-hexagone développé et le potentiel de cette technique à être utilisée pour fabriquer des structures piézoélectriques de forme libre avec des électrodes.

ABSTRACT

Piezoelectric materials serve as transducers to linearly convert mechanical energy to electrical energy and vice versa. Based on this capability, a variety of piezoelectric devices with desired geometry, performance and function have been fabricated for sensing, energy harvesting and actuating applications. Among them, three-dimensional (3D) flexible and conformal piezoelectric composite devices (high piezoelectric ceramic particles as filler; flexible polymers as matrix) are in great demand in many fields such as smart artificial skins, battery-free wearable sensors and energy harvesters, and soft robotics. Conventional manufacturing methods for making the piezoelectric devices such as solution casting, spin-coating, melt-extrusion, electrospinning, limit the complexity of the fabricated structures. Thus, 3D printing techniques such as direct-ink writing (DIW), stereolithography (SLA), digital light processing (DLP) and fused filament fabrication (FFF) have been increasingly used for this purpose.

Additionally, to make the electrical connection between the piezoelectric structures (fabricated using conventional or 3D printing techniques) and the interfaces, there is usually an additional step to add electrodes on the piezoelectric structures by painting, sputtering, or attaching conductive tapes or fabrics. The emergence of multi-material 3D printing technique provides an efficient way to combine the piezoelectric structure and electrodes fabrication processes. The purpose of this dissertation is to develop 3D flexible piezoelectric composite devices with electrodes for piezoelectric sensing and energy harvesting applications based on multi-material 3D printing technique.

First, to find out the most suitable piezoelectric material for the multi-material 3D printing process, we printed polyvinylidene fluoride (PVDF) films from the commercially available PVDF filament using a FFF 3D printer. We found that the as-printed PVDF films have a low electroactive β phase content (F_β) of 39%, thus it requires post stretching process to increase the F_β. The stretched and polarized PVDF films with a dimension of 40 × 20 × 0.06 mm^3 (length × width × thickness) have a piezoelectric coefficient (d_{33}) of 7.29 pC/N and a F_β of 65 % at a stretching ratio (R) of 4 after being polarized under an electric field of 30 V/μm. Although the resulting d_{33} of the fabricated PVDF films has been substantially enhanced by ~10-100 times higher than the related reported values, the stretching process limits the possibilities of making complex geometries with PVDF.

Subsequently, we incorporated high piezoelectric lead zirconate titanate (PZT) nanoparticles into flexible thermoplastic polyurethane (TPU) matrix and extruded the composite material into an FFF-printable filament (~1.75 mm). The developed TPU/30 vol% PZT piezoelectric composite material has a large elongation at breakage of ~56% and a d_{33} value of 6.8 pC/N after being polarized by the appropriate poling parameters. A multi-material FFF 3D printing technique was then utilized to fabricate 3D flexible piezoelectric composite lattices with electrodes with our developed piezoelectric composite filament and a commercially available conductive composite (TPU/carbon black) filament. Four types of 3D piezoelectric composite lattices: simple cubic (SC), body-centered cubic (BCC), cuboctahedron (CH) and octet truss (OT) (and one fully dense solid (FD) used as a benchmark) were designed and fabricated. The piezoelectric performance of the lattices was compared by means of experimental and finite element analysis (FEA) methods. At the same maximum compressive force, OT lattice can generate ~two times superior voltage output than FD sample. As a demonstrator, an original multi-material OT piezoelectric composite shoe sole can generate a high peak-to-peak voltage (V_{pp}) ~ 20 V by human stomping.

Further, to fabricate freeform or conformal flexible piezoelectric structures, we conducted a multi-material DIW 3D printing process in a supporting fluid. The developed mineral oil/6% (w/v) fumed silica supporting fluid with appropriate yield stress behaves as a Herschel-Bulkley Fluid. During the printing process, the crosslinked fumed silica network temporarily flows under the stress generated by the moving dispensing needle, and then rapidly recover to a solid state to hold the deposited ink. The compositions of the inks are: polydimethylsiloxane (PDMS)/30 vol% PZT as the piezoelectric composite ink and PDMS/25 vol% silver (Ag) as the conductive composite ink. A comprehensive characterization of the inks' properties (i.e., piezoelectric or conductive behaviors, rheological and mechanical properties) and the rheological behavior of the supporting fluid with different compositions were performed. Three demonstrators: a multi-layer planar film, a conformal non-planar hemisphere and a 3D structure composed of six spirals printed vertically between two hexagon layers (freeform spiral-hexagon) were fabricated and tested under tension or compression tests, respectively. For example, by cyclically compressing the freeform spiral-hexagon structure at 8 Hz for more than 800 cycles, a V_{pp} of 86.39 $\pm$ 1.145 mV was obtained, which shows the good durability of the developed piezoelectric spiral-hexagon sensor and the

potential of this technique to be used for fabricating compact freeform piezoelectric structures with electrodes.

TABLE OF CONTENTS

LIST OF TABLES

LIST OF FIGURES

LIST OF SYMBOLS AND ABBREVIATIONS

1D	One-dimensional
2D	Two-dimensional
3D	Three-dimensional
Ag	Silver
AM	Additive manufacturing
$BaTiO_3$	Barium titanate
DIW	Direct-ink writing
DIC	Digital image correlation
DLP	Digital light processing
DMAc	N, N-dimethylacetamide
DMF	Dimethylformamide
DMSO	Dimethyl sulfoxide
FFF	Fused filament fabrication
FTIR	Fourier transform infrared spectroscopy
ITO	Indium tin oxide
N/A	Not applicable
PDMS	Polydimethylsiloxane
PU	Polyurethane
PVA	Polyvinyl alcohol
PVDF	Polyvinylidene fluoride
PVDF-CTFE	Polyvinylidene fluoride-co-chlorotrifluoroethylene
PVDF-HFP	Polyvinylidene fluoride-co-hexafluoropropylene

PVDF-TrFE	Polyvinylidene fluoride-co-trifluoroethylene
PZT	Lead zirconate titanate
SEM	Scanning electron microscopy
SLA	Stereolithography
TPU	Thermoplastic polyurethane
UV	Ultraviolet
A_α	Absorption fraction of α phase
A_β	Absorption fraction of β phase
d^c	Converse piezoelectric coefficient
d^d or d	Direct piezoelectric coefficient
D	Electrical displacement
E	Electric field
F_β	β phase fraction
k	Electromechanical coupling factor
K	Consistency index
n	Flow index
η	Viscosity
η_a	Apparent viscosity
P	Power
r	Resistance
R	Stretching ratio
$\dot{\gamma}$	Shear rate
s	Elastic compliance
s^D	Elastic compliance at constant electric displacement

S	Strain
T_c	Curie temperature
τ	Shear stress
τ_0	Yield stress
V_{pp}	Peak-to-peak voltage
ν	Poisson's ratio
Y	Young's modulus
ε	Dielectric permittivity
ε_γ	Relative dielectric permittivity
ε_0	Dielectric permittivity of a vacuum (8.854×10^{-12} F/m)
ε^σ	Dielectric permittivity at constant stress
ρ	Density

CHAPTER 1 INTRODUCTION

1.1 Background

Having the ability to interconvert electrical and mechanical energy, piezoelectric materials have been widely used in sensing, energy harvesting, and actuating applications [1]. For the direct piezoelectric effect (i.e., sensing and energy harvesting applications), electrical power can be generated from human kinematics, machine operations, environmental energy such as sea waves and wind. The generated electrical charges can be stored as energy harvesters or be readable as self-powered sensors. For the converse piezoelectric effect (i.e., actuating applications), based on the inherent properties of high displacement accuracy and high response speed in the presence of an applied electric field [2], piezoelectric materials can be made into implantable cardiac pacemaker, actuation parts for soft robotics, and metrology tools [3], [4].

The conventional piezoelectric materials are polymer polyvinylidene fluoride (PVDF) and its copolymers such as polyvinylidene fluoride-co-trifluoroethylene (PVDF-TrFE), and ceramics such as lead zirconate titanate (PZT) and barium titanate ($BaTiO_3$). Piezoelectric polymers have the advantages of good flexibility, lightweight, low acoustic impedance compared to the more brittle piezoelectric ceramics. However, piezoelectric polymers have a lower piezoelectric coefficient compared to the best piezoelectric ceramics [5]. To improve the shortcomings existing in the piezoelectric polymers and ceramics, piezoelectric composite materials are increasingly developed by incorporating high piezoelectric ceramic particles into the flexible polymer matrix [6]–[13].

The advent of three-dimensional printing techniques, such as stereolithography (SLA) [14], digital light processing (DLP) [1], [15], direct-ink writing (DIW) [16], [17], and fused filament fabrication (FFF) [18], brought great opportunities to increase the designability of piezoelectric response and improve the geometrical conformality of the piezoelectric devices by building various complex architectures. Among them, FFF and DIW 3D printing techniques are the most promising 3D printing technique for manufacturing piezoelectric composite materials due to the breadth of available and compatible materials. The mechanism of FFF 3D printing technique is to employ a heated nozzle to melt the thermoplastic filament, while the one of DIW is to extrude a liquid ink out of the dispensing nozzle controlled by a pressure system and the shape retention is achieved by either ultraviolet (UV) curing, volatile solvent evaporation, etc. [19]. Additionally, there is usually

an extra step to add electrodes on the piezoelectric elements for collecting the generated charges. Multi-material 3D printing technique is an efficient method for producing 3D multi-functional structures with two or more independent printing heads (DIW or FFF). The flexibility of the multi-material 3D printing technique can enable also the co-fabrication of electrodes in the same process of piezoelectric sensing parts. However, the geometries of the existing multi-material 3D printed piezoelectric structures are limited into one-dimensional (1D) fiber [20], two-dimensional (2D) film [21] or simple 3D scaffold shape [22]. In this dissertation, we seek to build geometrically more complex 3D flexible high-performance piezoelectric composite devices with electrodes based on the multi-material 3D printing technique.

1.2 Dissertation structure

This dissertation includes seven chapters. Chapter 1 introduces the background of the study and the structure of the dissertation. Chapter 2 provides a literature review of the piezoelectricity, the commonly used piezoelectric materials and their conventional and state-of-the-art manufacturing techniques. Chapter 3 presents the research objectives and the coherence of the articles. The main results of this dissertation are given in the form of three articles submitted to peer-reviewed scientific journals in Chapters 4 to 6. Chapter 4 presents the FFF printed polyvinylidene fluoride films with tailored stretching and poling parameters for piezoelectric sensing and energy harvesting applications. Chapter 5 demonstrates the comparison of the piezoelectric performance of four types of multi-material FFF 3D printed flexible piezoelectric composite lattices (and one fully dense solid for benchmark) with electrodes by means of experimental and finite element analysis (FEA) methods. Chapter 6 illustrates the multi-material freeform direct-ink writing (DIW) 3D printed flexible piezoelectric composite sensors with electrodes in a mineral oil/fumed silica supporting fluid. Chapter 7 provides a general discussion of the research. Chapter 8 summarizes the conclusion of the research and gives several recommendations for future work.

CHAPTER 2 LITERATURE REVIEW

The literature review contains three main sections introducing the piezoelectric effect and the piezoelectric coefficient, the commonly used piezoelectric materials (e.g., polymers, ceramics), and their conventional and the state-of-the-art manufacturing techniques.

2.1 Piezoelectricity

2.1.1 Background of piezoelectricity

The term piezoelectric comes from the Greek word *piezein*, meaning squeeze. Piezoelectricity was discovered in 1880 by the brothers Jacques Curie and Pierre Curie. They found that upon mechanical stress (tension or compression), some crystals, such as tourmaline, quartz, topaz, cane sugar, and Rochelle salt (sodium potassium tartrate tetrahydrate) can generate electric charges which is proportional to the applied load. This phenomenon was called direct piezoelectric effect (Figure 2.1a) [23]. Shortly, the converse (indirect) piezoelectric effect (Figure 2.1b) was predicted by Fabriel Lippman in 1881 via mathematical deduction from fundamental thermodynamic principles [24] and confirmed by the Curie brothers via experiments [25], in which the mechanical deformations occur when an electric field is applied to such materials.

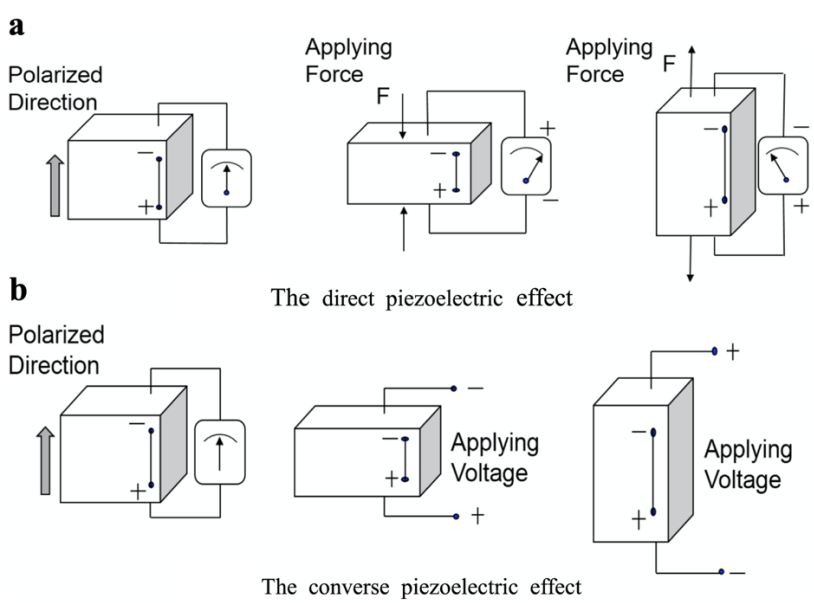

Figure 2.1 Schematic illustrations of two types of piezoelectric effects: (a) direct piezoelectric effect, and (b) converse piezoelectric effect [26].

Direct piezoelectric effect is widely used to fabricate piezoelectric sensors and energy harvesters to detect or store the electrical energy induced by the mechanical strain. Converse piezoelectric effect is the basis for piezoelectric actuators. The mechanism is to apply a sufficiently high drive voltage on the piezoelectric materials to make them experience a mechanical deformation (contraction or stretch). The advantages and disadvantages of three types of piezoelectric applications are summarized in Table 2.1.

Table 2.1 The applications of two types of piezoelectric effects and their pros and cons.

Type	Application	Advantage	Disadvantage	Ref
Direct	Sensor	High sensitivity Wide frequency response range No need of external power source	Not capable of detecting static force	[27]
	Energy harvester	High voltage output High power density	Low current output High output impedance	[28]
Converse	Actuator	High displacement accuracy High response speed	Small displacement under a high drive voltage	[2]

The piezoelectricity originates from the dipole moments of the piezoelectric materials. The dipole moments arise from differences in electronegativity below a specific transformation temperature called Curie temperature (T_c) [29]. As shown in Figure 2.2, the aim of the poling process in the manufacturing of piezoelectric materials is to align the randomly dispersed dipoles moments in the crystals to generate a net polarization by applying a sufficiently strong electric field at temperature below T_c [30]. The direction along which the dipoles align known as the poling direction. Similar to piezoelectricity, pyroelectricity is the ability of the material to generate electric charges upon temperature changes. The ferroelectricity refers to the property of certain materials having a spontaneous electric polarization that can be reversed by the application of an opposite electric field [31].

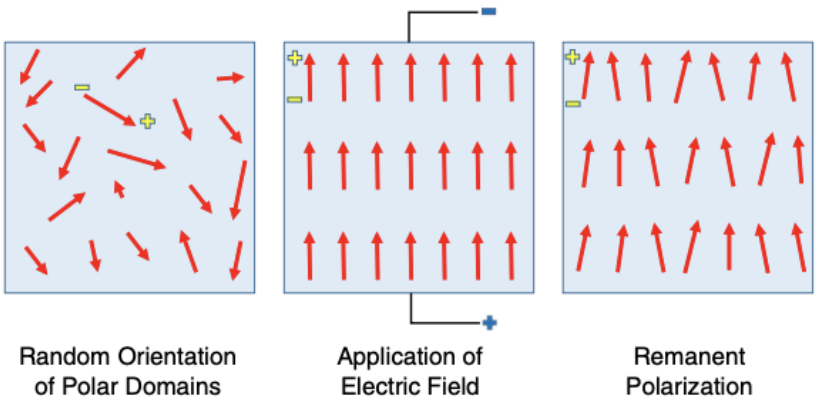

Figure 2.2 Schematic of dipole moments orientation: before, during and after the poling process (the red arrows represent the dipole moments in the crystals) [32].

2.1.2 Definition of piezoelectric coefficient

The piezoelectric coefficient, d_{ij}, also known as piezoelectric constant or piezoelectric modulus, is the net polarization generated per unit of mechanical stress applied or the induced mechanical strain per unit of electric field strength. There are two subscripts to d_{ij}: one is the direction of generated polarization or the applied electric field; the other is the direction of the applied mechanical stress or the induced mechanical strain, respectively [33]. Figure 2.3a presents the direction of the applied force. We suppose that poling direction is coincide with the Z-axis in a XYZ-axes system. Direction X, Y, or Z is represented by the number 1, 2, or 3, respectively, and shear to one of these axes by the number 4, 5, or 6, respectively. Three commonly investigated piezoelectric modes are shown in Figure 2.3b: longitudinal (d_{33}), transverse (d_{31}) and shear (d_{15}) modes.

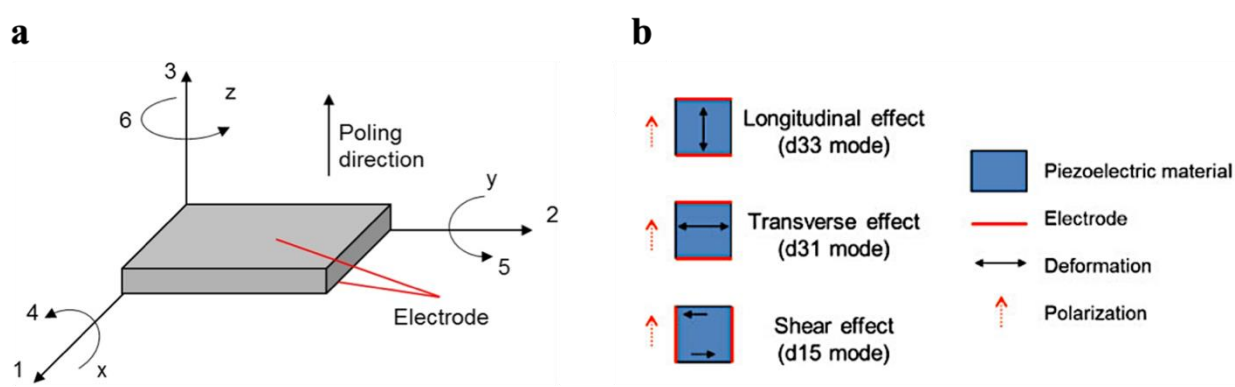

Figure 2.3 (a) Piezoelectric mode determined by the direction of applied force [26]. (b) Three commonly used piezoelectric modes: d_{33}, d_{31} and d_{15} [34].

The constitutive relations for direct or converse piezoelectric effects are described based on IEEE Standard-1987 [35]:

For the direct piezoelectric effect, the electric displacement D (C/m^2) can be calculated as:

$$D = \varepsilon^{\sigma} E + d^{d} \sigma \tag{2.1}$$

which can be rewritten in expanded notation as:

$$\begin{bmatrix} D_1 \\ D_2 \\ D_3 \end{bmatrix} = \begin{bmatrix} \varepsilon^{\sigma}{}_{11} & \varepsilon^{\sigma}{}_{12} & \varepsilon^{\sigma}{}_{13} \\ \varepsilon^{\sigma}{}_{21} & \varepsilon^{\sigma}{}_{22} & \varepsilon^{\sigma}{}_{23} \\ \varepsilon^{\sigma}{}_{31} & \varepsilon^{\sigma}{}_{32} & \varepsilon^{\sigma}{}_{33} \end{bmatrix} \begin{bmatrix} E_1 \\ E_2 \\ E_3 \end{bmatrix} + \begin{bmatrix} d^{d}{}_{11} & d^{d}{}_{12} & d^{d}{}_{13} & d^{d}{}_{14} & d^{d}{}_{15} & d^{d}{}_{16} \\ d^{d}{}_{21} & d^{d}{}_{22} & d^{d}{}_{23} & d^{d}{}_{24} & d^{d}{}_{25} & d^{d}{}_{26} \\ d^{d}{}_{31} & d^{d}{}_{32} & d^{d}{}_{33} & d^{d}{}_{34} & d^{d}{}_{35} & d^{d}{}_{36} \end{bmatrix} \begin{bmatrix} \sigma_1 \\ \sigma_2 \\ \sigma_3 \\ \sigma_4 \\ \sigma_5 \\ \sigma_6 \end{bmatrix} \tag{2.2}$$

where ε^{σ} is the dielectric permittivity (F/m) at constant stress σ (N/m^2), E is the electric field (V/m) generated by the strain, and d^{d} is the direct piezoelectric coefficient (pC/N). Equation 2.2 describes d^{d} with respect to different types of deformations.

For the converse piezoelectric effect, the strain S generated by the application of electric displacement can be calculated as:

$$S = s^{D} \sigma + d^{c} D \tag{2.3}$$

where d^{c} is the converse piezoelectric coefficient (m/V) and s^{D} is the elastic compliance (m^2/N) at constant electric displacement.

The relationship between the direct and converse piezoelectric coefficients are as below:

$$d^{d} = \varepsilon_{\gamma} \varepsilon_{0} d^{c} \tag{2.4}$$

where ε_{γ} and ε_{0} (8.854×10^{-12} F/m) are the relative dielectric permittivity of the piezoelectric material and the dielectric permittivity of the vacuum, respectively.

2.2 Piezoelectric materials

Piezoelectric materials can be classified into two groups: natural or man-made. The natural piezoelectric materials include crystal materials: quartz, Rochelle salt, Topaz, Tourmaline-group minerals and some organic substances: silk, wood, enamel, dentin, bone, and hair. Man-made piezoelectric materials are crystals that are quartz analogs, ceramics (e.g. lead zirconate titanate

(PZT), barium titanate ($BaTiO_3$)), polymers (e.g. polyvinylidene fluoride (PVDF) and its copolymers polyvinylidene fluoride-co-trifluoroethylene (PVDF-TrFE)) and their composites [36]. Table 2.2 presents the comparison of the commonly used piezoelectric materials. The advantages and disadvantages of piezoelectric materials are also compared in

Table 2.3. PVDF has the advantages of lightweight, flexibility, biocompatibility, and a low acoustic impedance close to water – 1.48 MRayl (i.e., PVDF can be fabricated into underwater sensors). PZT is brittle in nature and toxic (lead), but it has a high piezoelectric performance and low material cost compared to PVDF.

Table 2.2 Comparison of properties of the commonly used piezoelectric materials.

Properties	PZT	$BaTiO_3$	PVDF	PVDF-TrFE
Density ρ (g/cm^3)	7.6	5.7	1.78	1.82
ε_γ	1,900	1,700	12-13	7-8
d_{33} (pC/N)	400	191	33	24-30
-d_{31} (pC/N)	175	78	23	11
d_{15} (pC/N)	590	270	N/A	N/A
Electromechanical coupling factor k_{33}	72%	49%	20%	29%
k_{31} (at 1 kHz)	36%	21%	12%	20%
Acoustic impedance (MRayl)	31.5	30	2.7	4.5
Young's modulus Y (GPa)	60	59.2	2-4	3-5
T_c (℃)	360	130	N/A	115
Price (CAD/kg)	~193 APC 850 APC Int. Ltd.	~157 #5622ON-01 Inframat®	~1,464 #182702 Sigma-Aldrich®	~8,960 FC25 Piezotech®
Ref	[37]	[5], [38]	[5], [39]	[5], [39]

Table 2.3 Comparison between piezoelectric ceramic and piezoelectric polymer [5].

Type	Advantages	Disadvantages
Piezopolymer (PVDF)	• Flexibility • Light weight • Biocompatibility (non-toxic) • Low manufacturing cost • Low acoustic impedance	• Low piezoelectric coefficient • Low operating temperature • Low electromechanical coupling
Piezoceramic (PZT)	• High piezoelectric coefficient • High operating temperature	• Brittleness • Toxicity (lead) • Low material cost

2.2.1 Piezoelectric polymer PVDF

Kawai discovered the piezoelectricity of PVDF in 1969 [40]. As a semi-crystalline (crystalline fraction of 35-70%) fluoropolymer, PVDF exists in five phases (also known as polymorphs): α, β, γ, δ and ε, as reported by Lando *et al*. [41]. The chemical structure of PVDF has a repeating unit of $-CF_2-CH_2-$ [21]. The phases of PVDF are classified by the relative position of the fluorine and hydrogen atoms to the C – C backbone.

The most common and stable phase of PVDF is the α phase, which is a nonpolar phase readily obtained during the process of crystallization from the melt or polymerization [42]. The conformation of α phase is trans-gauche-trans-gauche' (TGTG'). Under specific processes such as mechanical stretching, annealing, and electric poling, α phase can be transformed into β, γ and δ phases, respectively. Among them, the electroactive (polar) β phase is the most important polymorph due to its highest spontaneous polarization resulting in higher piezoelectricity and pyroelectricity in PVDF [43]. The β phase is found in all trans (TTTT) planar zigzag conformation and has a strong dipole moment (7×10^{-30} Cm) due to the fact that fluorine atoms and hydrogen atoms occupy each side of the β phase molecular chains [44]. The polar γ phase can also be obtained

in crystallization from polar solvent such as dimethyl sulfoxide (DMSO), or at high pressures, high temperatures. It appears in a TTTGTTTG' conformation. As for the polar δ phase (TGTG'), it can be formed by the application of electric field on α phase. The configuration of nonpolar ε phase is similar to γ phase in a TTTGTTTG' form [45]. Figure 2.4 a (I-III) shows the molecular structures of α, β and γ phases, respectively. (IV-VI) shows the molecular structures of copolymers: PVDF-TrFE, polyvinylidene fluoride-co-hexafluoropropylene (PVDF-HFP) and polyvinylidene fluoride-co-chlorotrifluoroethylene (PVDF-CTFE). As shown in Figure 2.4 b, the morphology of semi-crystalline PVDF consists of crystalline regions dispersed in amorphous regions. Mechanically stretching the polymer aligns the amorphous regions along with the stretch direction, and electrically poling permanently orients the dipole moments in PVDF in a desirable direction.

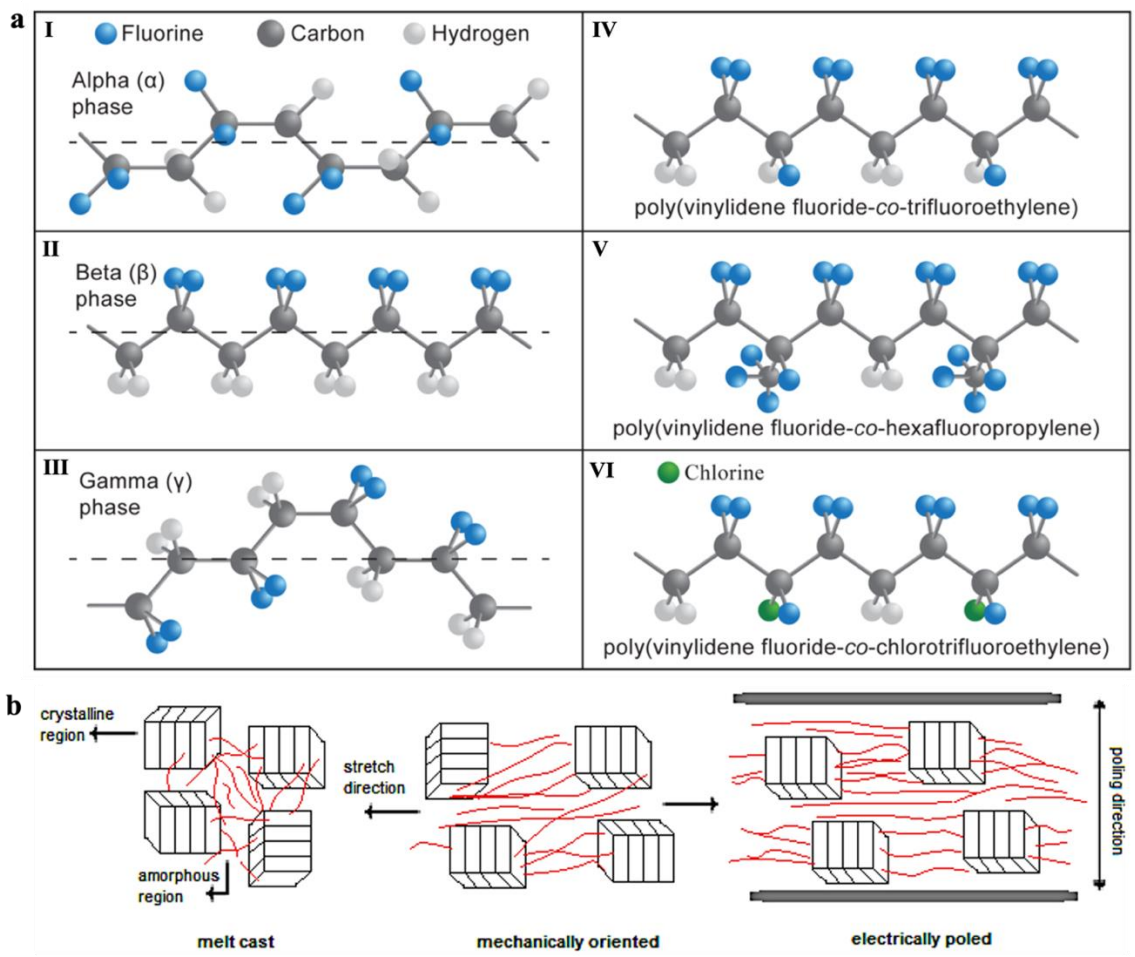

Figure 2.4 (a) The molecular structures of I-III: PVDF phases, and IV-VI: PVDF copolymers [46]. (b) Orientation of PVDF molecules by mechanical stretching and electrical poling processes [47].

Fourier transform infrared spectroscopy (FTIR) technique is used to identify and quantify the presence of different phases in PVDF. In Figure 2.5, the α phase of PVDF presents a large number of characteristic peaks at 766, 795, 855 and 976 cm^{-1}. However, the β and γ phase have a similar number of peaks and these peaks almost appear at similar wavenumber due to the similar polymer chain conformation. Recently, it has been agreed that the peak at 840 cm^{-1} is common to both phases, but it is a strong peak for the β phase only. In addition, the band at 1279 cm^{-1} is exclusive for β phase, while 431, 776, 812, 833 and 1233cm^{-1} are exclusive for the γ phase [48]. The modified Beer-Lambert law is utilized to calculate the fraction of β phase (F_β) in PVDF. The equation is shown below [49]:

$$F_\beta\,(\%) = \frac{A_\beta}{1.26A_\alpha + A_\beta} \tag{1}$$

where A_α and A_β are the absorbance of α and β phases at 763 and 840 cm^{-1}, respectively, and 1.26 is the ratio of absorption coefficient at the corresponding wavenumber of 6.1×10^4 and 7.7×10^4 cm^2mol^{-1} for α and β phases, respectively.

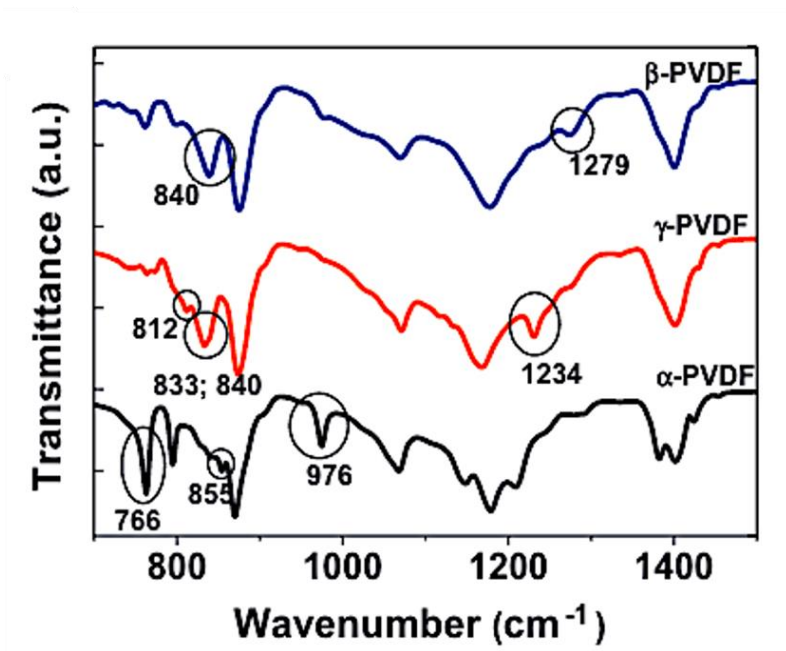

Figure 2.5 FTIR spectra of three phases in PVDF: α, β and γ phases, respectively [50].

2.2.2 Piezoelectric ceramic

The discovery of piezoelectric perovskite ceramic crystals $BaTiO_3$ and PZT in the 1940s and 1950s expanded the commercial use of piezoelectric devices benefiting from their excellent dielectric and piezoelectric properties. The perovskite structure (ABO_3) is the arrangement where the corner-sharing oxygen octahedra are linked together in a cubic array with smaller cations (Ti, Zr, Sn, Nb etc.) occupying the central octahedral B-site, and larger cations (Pb, Ba, Sr, Ca, Na etc.) filling the interstices between octahedra in A-sites [51]. As shown in Figure 2.6, above T_c, perovskite crystal is a centrosymmetric structure with no dipole moment, i.e., no piezoelectricity; below T_c, it is in non-centrosymmetric tetragonal structure with a dipole moment [52].

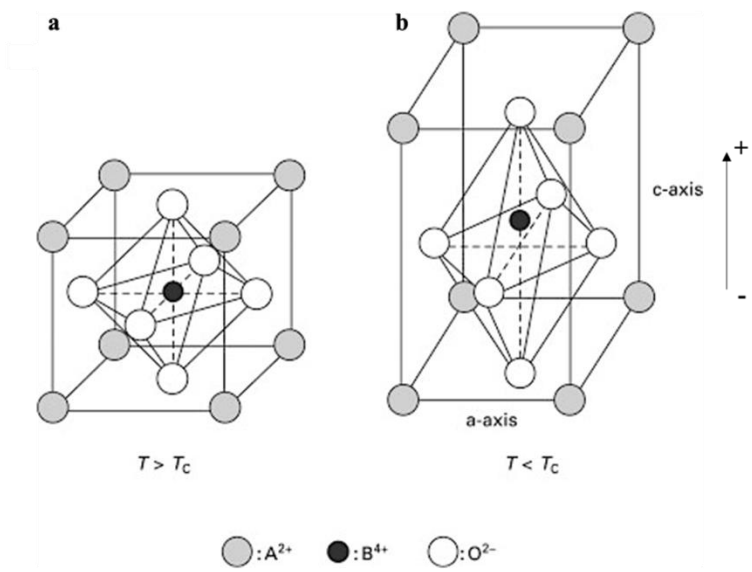

Figure 2.6 Crystal structures of perovskite ceramic: (a) above T_c, and (b) below T_c [53].

2.2.3 Piezoelectric ceramic composites

In order to overcome the shortcomings of the piezoelectric ceramics i.e., brittleness and complex manufacturing process, and the shortcomings of the piezoelectric polymers i.e., low piezoelectric coefficient, simple structures limited by the stretching process, many researchers developed piezoelectric ceramic based composites by adding the ceramic fillers into various types of polymer matrix. Although the piezoelectric performance of the piezoelectric ceramic composites is lower compared to the pure ceramic, it broadens the way of creating flexible and durable piezoelectric devices. Table 2.4 lists the composition and the piezoelectric performance of the piezoelectric

ceramic composites developed in some of the related published works. We observe that PVDF and its copolymers, and flexible polymers such as polyurethane (PU), polydimethylsiloxane (PDMS) are used as matrix in most of the works. The maximum filler content is up to 50 vol% due to the increased viscosity of the composite.

Table 2.4 The composition and piezoelectric property of piezoelectric ceramic composites.

Ceramic filler type	Filler content	Polymer matrix type	Piezoelectric performance	Ref
PZT	48 vol%	PVDF-TrFE	d_{31} = - 56 pm/V	[54]
	50 vol%	PU	d_{33} = 13 pC/N	[55]
	32 vol%	Polydimethylsiloxane (PDMS)	d_{33} = ~95 pC/N	[56]
	50 vol%	PDMS	d_{33} = 25 pC/N	[57]
	28 vol%	PDMS	d_{33} = 78.33 pC/N	[58]
	37 vol%	PVDF	d_{33} = 10.51 pC/N	[59]
	50 vol%	PU	d_{33} = ~18 pC/N	[60]
$BaTiO_3$	50 vol%	Epoxy	d_{33} = ~3.8 pC/N	[61]
	5 vol%	PVDF-TrFE	~200 mV (finger tap)	[62]
	8 vol%	PVDF	~6 V (12 N)	[63]
	8 vol%	PDMS	~30 V (0.13 MPa)	[64]
	10 vol%	PVDF-HFP	~75 V (0.23 MPa)	[65]

2.3 Methods for manufacturing piezoelectric materials

Since the advent of piezoelectric materials, many techniques have been employed to fabricate piezoelectric structures to meet different shape, function, and material requirements. In this section, poling process, various types of conventional techniques used to fabricate piezoelectric polymer, ceramic and their composites will be presented.

2.3.1 Poling process

As illustrated in Figure 2.2, the poling process is beneficial in the manufacturing of piezoelectric materials in order to create a strong net polarization (i.e., piezoelectricity) through the alignment of dipole moments under a sufficiently high electric field at an elevated temperature. Before the poling process, electrodes are required on the surfaces of piezoelectric elements by painting [66], screen printing [12], sputtering [67], or attaching conductive tape or fabrics [68], [69].

Figure 2.7 shows two types of poling methods: contact poling and corona poling processes [70]. In the contact poling process, a sufficiently high electric field is applied directly on the top and bottom electrodes of the piezoelectric materials. The electrical breakdown will happen when the poling voltage exceeds the dielectric strength of the material or when the imperfections exist in the poled materials [71]. During the electrical breakdown process, the electrical insulating material suddenly changes to a conductor and electric current flows through it [72]. Once electrical breakdown occurs, the material is destroyed. Thus, the contact poling process should be performed in a vacuum chamber or silicone oil insulating bath.

In the corona poling process, air molecules are ionized above the poled material by applying a high voltage on a needle. The ionized charges are deposited on the top surface of the poled material. A grid voltage is added to make sure the charges are uniformly distributed on the top surface of the poled material. The advantage of the corona poling process is that when an electrical breakdown happens at one point, since there is no need to paint electrode on the top surface of the material in the corona poling process, the resulted conductive path is limited to this point, the poling process in other places can continue [73].

Three poling parameters will significantly affect the poling results: poling voltage, time and temperature. Poling voltage should be sufficiently high and poling time should be long enough to align the dipole moments. An elevated temperature can increase the mobility of the dipoles [74]. Table 2.5 lists the poling parameters for the commonly used PVDF (and its copolymers), PZT and their composites in some of the related published works. We summarize the range (minimum-maximum values) of the poling parameters. For the contact poling of PVDF: 10-125 kV/mm; 60-360 min; 30-90℃. PZT has a relatively low poling field of 2-20 kV/mm, shorter time ~20 min and higher temperature ~100℃ compared to the contact poling parameters of PVDF. For the corona

poling, the electric field is higher and the time is shorter for both PVDF and PZT compared to the contact poling.

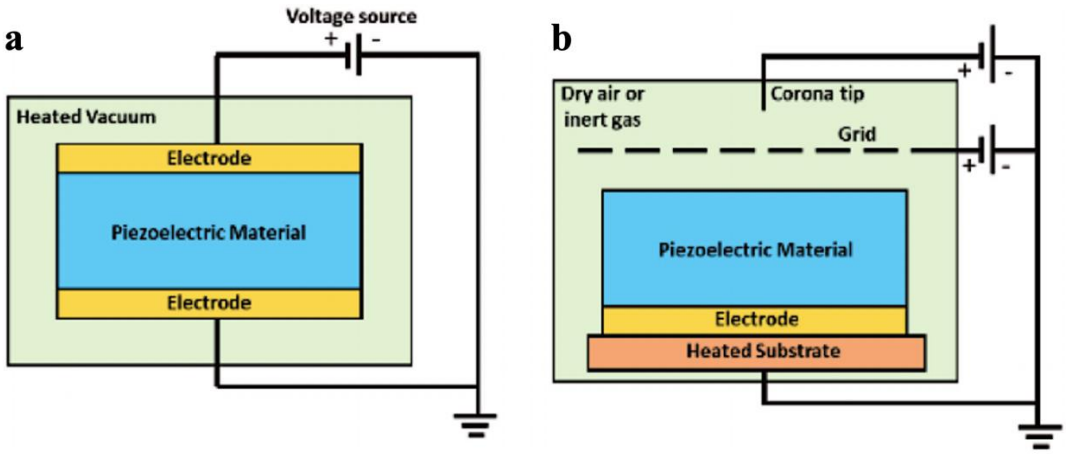

Figure 2.7 Schematic of (a) Contact poling, and (b) Corona poling setups [70].

Table 2.5 Poling parameters for PVDF (and its copolymers), PZT and their composites.

Material	Method	Time (min)	Electric field (kV/mm)	Temperature (℃)	Ref
PVDF	Contact	60	125	90	[75]
	Contact	120	10	50	[76]
	Contact	360	30	30	[77]
	Corona	1	625	60	[75]
	Corona	10	180	103	[78]
	Corona	30	55	80	[79]
	Corona	N/A	10	80	[80]
PVDF-TrFE	Corona	N/A	60	60	[81]
PVDF-HFP	Corona	N/A	160	65	[82]
PZT/PDMS	Contact	40	18	150	[7]

PZT	Contact	20	2	120	[83]
	Corona	N/A	2	80	[84]
PZT/PVDF	Contact	0.5	20	20	[85]
	Corona	0.5	2	20	[85]

2.3.2 Conventional methods for manufacturing PVDF

The conventional techniques to fabricate PVDF based piezoelectric devices include solution casting, spin-coating, electrospinning and melt-extrusion [86]. The procedure and the related published works of each main technique are explained in this section. During or after the PVDF fiber or film fabrication process, stretching process is usually required to increase the electroactive F_β by stretching the PVDF fiber or film with an appropriate stretching ratio (R). The R is the ratio of the final length to the original length. Mechanical stretching of PVDF fiber or film with R of 4.5 to 6 at a suitable temperature are usually used in most of the works [87].

Solution casting and spin-coating (Figure 2.8) are two simple methods to fabricate PVDF films by dissolving PVDF powder in solvent such as N, N-dimethylacetamide (DMAc) [88], dimethylformamide (DMF), N-methyl-2-pyrrolidinone (NMP), DMSO [89], and methyl ethyl ketone (MEK) [85], and spreading the obtained solution on a clean substrate or a rotational plate. The solution is dried under the fume hood in order for the solvent to evaporate. Then the PVDF film is peeled off from the substrate. An elevated temperature can be applied to accelerate the solvent evaporation process [88].

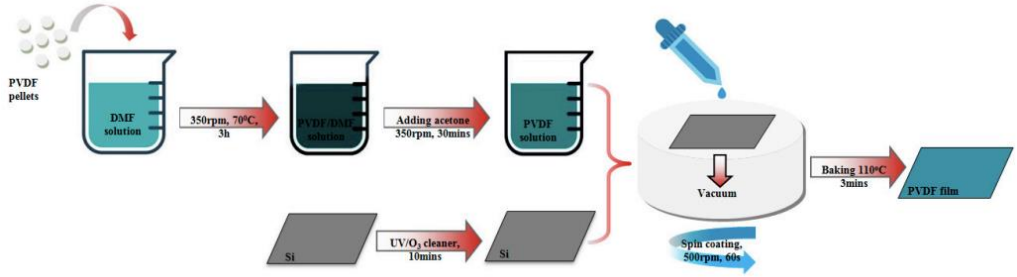

Figure 2.8 Schematic of the spin-coating of a PVDF film: substrate cleaning, solution mixing (PVDF/DMF), spin-coating, and oven drying [90].

Electrospinning, invented by Formhals in 1934 [91], is a process to manufacture one dimensional (1D) fine piezoelectric fibers, two-dimensional (2D) thin mats and membranes by applying the electric force to draw the charged threads from the polymer solution or melt. The produced fibers possess the diameters ranging from tens of nanometers to several micrometers [92]. A typical electrospinning process to fabricate PVDF membranes is shown in Figure 2.9. The setup consists of a high voltage power supply, a syringe with a metallic needle, and a grounded collector. The collector is a stationary or rotational metal plate or cylinder. The mixture of DMF and acetone solvent is usually used as the solvent system for PVDF. Near-field electrospinning process is evolved from the conventional electrospinning process to a more efficient in-situ poling assisted electrospinning process [93]–[100]. Like its name, the distance between the extrusion nozzle and the collector is reduced, which results in the orientation of the dipole moments in PVDF [93].

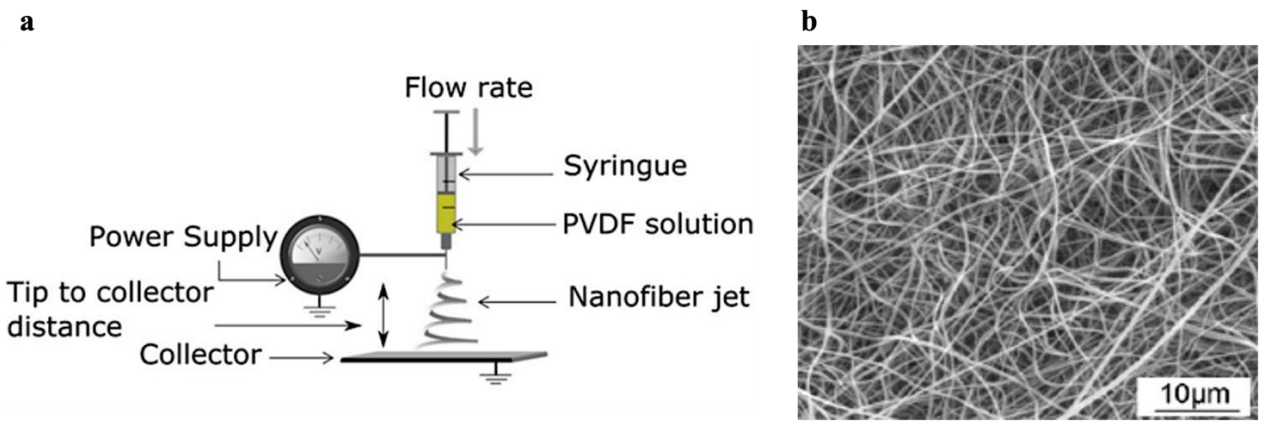

Figure 2.9 (a) Schematic of the electrospinning of PVDF membrane [99]. (b) Scanning electron microscopy (SEM) image of the electrospun PVDF membrane [100].

Melt-extrusion process is to fabricate piezoelectric PVDF filament (or fiber) or film directly from the molten state [101], [102]. The PVDF powder or pellets are fed into the inlet hopper and melted usually at the temperature 10℃ above the melting point (melting temperature of PVDF: ~172℃) (Figure 2.10a) [103]. In addition, a novel multi-material fiber drawing technique was developed by Lu *et al*. to fabricate micro- and nanostructured piezoelectric fibers with electrodes from the multi-layer alternating sheets of the commercial conductive sheets and the fabricated electrospun PVDF/PZT or PVDF/$BaTiO_3$ piezoelectric composite sheets (Figure 2.10b) [11], [104]. The

piezoelectric fiber with electrodes were further weaved into a cotton textile for sensing and energy harvesting applications.

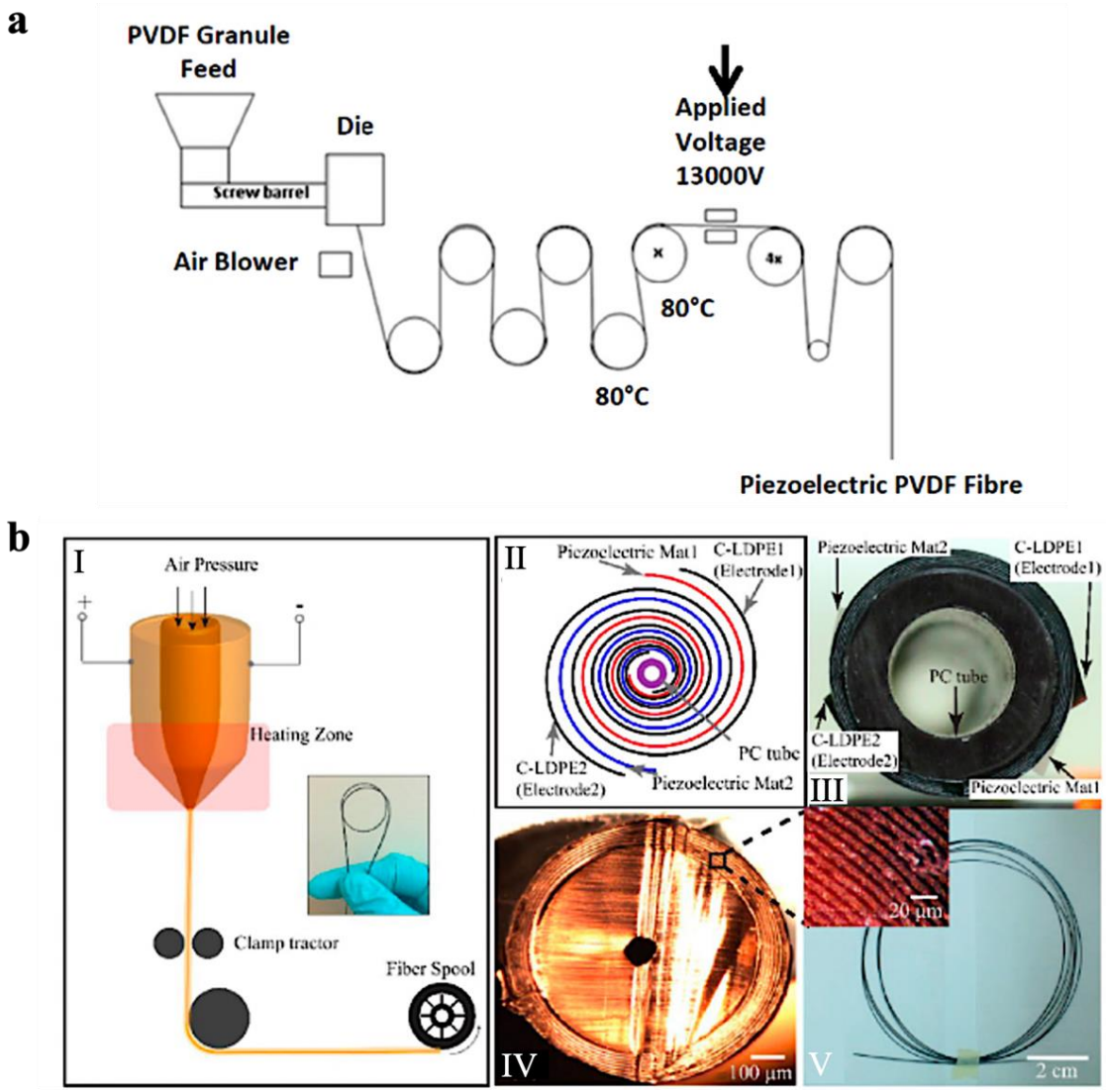

Figure 2.10 (a) Schematic of the piezoelectric PVDF fibers melt-extrusion, stretching and poling processes [105]. (b) Multi-material melt-drawing of piezoelectric fibers with electrodes: (I) Schematic of a piezoelectric fiber melt-drawing process. (II) Schematic of the multilayer structure with alternating piezoelectric and electrode layers in the preform. (III) Photo of the cross-section view of a preform. (IV) Photo of the cross-section view of a preform with a diameter of ~900 μm (drawn voltage: 2 kV). Inset: Magnified view of a multilayer structure. (V) Spool of a piezoelectric fiber with electrodes [11].

2.3.3 Conventional techniques for manufacturing PZT

The fabrication of PZT piezoelectric devices consists of three steps: the first step is to shape the PZT powder into the desired shapes such as fiber, disc, ring or cylinder by mixing with a binder - polyvinyl alcohol (PVA). The second step is to decompose the binder and sinter the PZT structure by heating the structures at high temperature (~1200℃) in a furnace. The dense PZT structure is then coated with electrode materials and polarized according to the desired poling time, temperature and voltage parameters [106]. Although the fabricated PZT devices with high piezoelectric performance have been widely used in the sensing and actuating applications, they are brittle and susceptible to cracking during usage [107]. Also, the shapes are mainly in 1D fiber, 2D disc or simple 3D structures (e.g., hollow cylinder).

2.4 3D printing techniques for manufacturing piezoelectric materials

3D printing, also known as additive manufacturing (AM), is a family of processes for the creation of 3D objects with increasing successive layers of materials based on sliced 3D model files. When compared to the conventional fabrication techniques, 3D printing technology has many advantages such as fast design and production, less energy-consumption and the ability to fabricate 3D structures featuring conformal and complex geometries [108]. As a highly flexible manufacturing technique, 3D printing techniques can be applied to a diverse range of materials such as plastics, metals, ceramics, concrete and biomaterials. Over the past decade, several types of 3D printing techniques have increasingly been utilized to fabricate smart materials [17], [87], [109]–[116] including piezoelectric materials i.e., direct-ink writing (DIW), stereolithography (SLA), digital light processing (DLP), and fused filament fabrication (FFF) 3D printing techniques. In addition, multi-material 3D printing process provides an efficient way to fabricate piezoelectric structures and electrodes in a single manufacturing process.

3D piezoelectric structures have three main advantages over 1D or 2D piezoelectric structures: improved electromechanical response and accessible strain extractable from 3D designs, and there is a coupling effect between the three types of modes (longitudinal, transverse and shear modes) of piezoelectric coefficients.

2.4.1 Direct-ink writing

DIW 3D printing technique is a flow-based technique to build 3D structures by extruding the ink using a pneumatic-driven pressure system mounted on an XYZ-3 axes moving extrusion head. Bodkhe *et al*. used a solvent-evaporation assisted DIW method to fabricate piezoelectric film and 3D cylindrical sensors with PVDF/10 wt% $BaTiO_3$ nanocomposites dissolved in a mixture of DMF, acetone and DMSO solvent. The schematic of the solvent-evaporation assisted DIW 3D printing process and the fabricated sensors are shown in Figure 2.11. The volatile solvent plays an important role in shape retention. The viscosity of ink is adjusted by changing the concentration of the polymer composite in the solvent to exhibit a shear-thinning behavior. In addition to the concentration of the ink, the printing parameters such as the printing speed, applied extrusion pressure, ambient temperature and humidity, inner diameter of the nozzle have to be properly adjusted for successful fabrication. The piezoelectric coefficient of the developed sensor in their work was 18 pC/N, which is close to the value of commercial PVDF film sensors. But there are two drawbacks of this technique: short shelf life for the developed ink i.e., the liquid ink dries quickly in an hour, and the solvent is highly toxic.

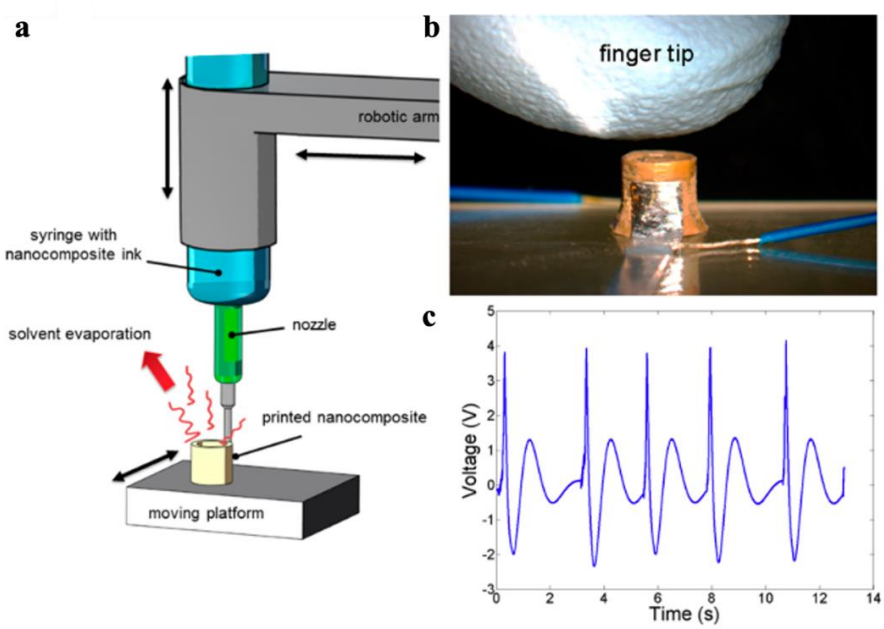

Figure 2.11 (a) Schematic of solvent evaporation-assisted DIW 3D printing of a cylindrical PVDF piezoelectric sensor. (b) Photo of the finger-tap test on a 3D cylindrical sensor. (c) The piezoelectric voltage output upon five consecutive finger-tap test [17].

2.4.2 Stereolithography and digital light processing

The mechanisms of the SLA and DLP 3D printing techniques are the same: using ultraviolet (UV) light to selectively cure the UV-curable resin and its composites. The only difference between these two techniques is the type of light source: SLA has a UV light beam, which cures the resin in a point-to-line, line-to-layer way; while DLP has a digital projector to cure a layer of resin [117]. Cui *et al*. fabricated piezoelectric composite lattices with designed anisotropy and directional response by DLP 3D printing technique [1]. The ink is composed of UV-curable resin and 50 vol% functionalized PZT particles using a functionalization agent - trimethoxysilyl propyl methacrylate. The piezoelectric performance of the fabricated piezoelectric lattices is compared with experimental and finite element analysis (FEA) methods. The drawbacks of these two techniques are that the UV-curable inks are sensitive to light, and the material is limited to photosensitive resins.

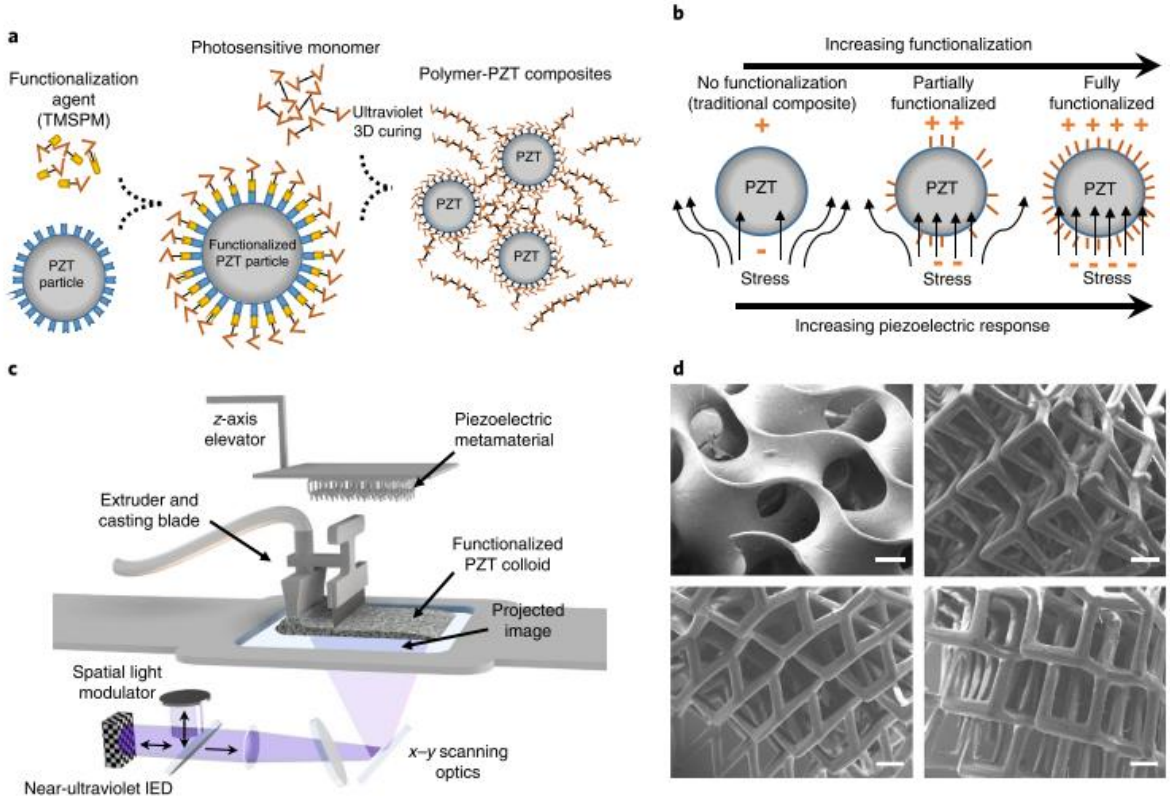

Figure 2.12 Schematic illustrations of (a) Strong bonding between the surface functionalized PZT particles and the polymer matrix after the UV curing process. (b) Increasing piezoelectric response

with the increase of functionalization (increasing stress transfer). (c) The DLP manufacturing process: a piezoelectric metamaterial is printed by being exposed to a near-UV light. (d) SEM images of the fabricated piezoelectric lattices. Scale bars, 300 μm [1].

2.4.3 Fused filament fabrication

FFF 3D printing, one of the most popular 3D printing technologies, is widely used in scientific and industrial fields. It is a melt-extrusion based approach to use a heated extrusion head to create 3D objects layer-by-layer from the thermoplastic filament on a heated build platform [118]. Evolved from the conventional FFF 3D printing technique, as seen in Figure 2.13, electric poling-assisted additive manufacturing (EPAM) technique emerged by adding a high poling electric field between the extrusion nozzle and the conductive printing bed. This electric field achieves in-situ poling of the extruded PVDF filaments, thus creating a net dipole moment in them [119]. However, a high voltage of 12 kV used in this process is dangerous for the users of the FFF 3D printers.

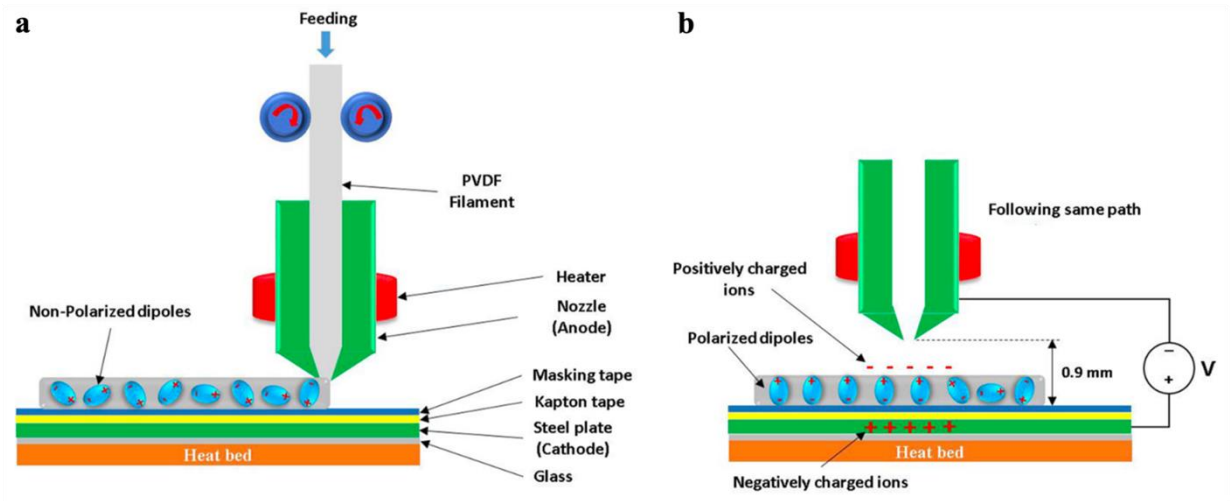

Figure 2.13 Schematic illustrations of the orientation of dipole moments in (a) FFF printed PVDF filament, and (b) EPAM printed PVDF filament (a high poling electric field is applied between the extrusion nozzle and the printing bed) [119].

2.4.4 Multi-material 3D printing

Multi-material 3D printing technique provides a useful way to fabricate multi-functional structures in a single manufacturing process by using either co-extrusion printing head, or two or more

printing heads (e.g., FFF or DIW). Multi-material 3D printing shows a great potential in the manufacturing of piezoelectric devices by combining the piezoelectric structures and electrodes manufacturing processes. To date, only a few studies have been published on the multi-material 3D printed piezoelectric structures with electrodes.

Figure 2.14 shows the work of Bodkhe *et al*. who developed a co-extrusion solvent evaporation-assisted DIW 3D printing process by applying two lines of conductive silver inks on the two inner sides of the syringe, and pouring the PVDF/10 wt% $BaTiO_3$ piezoelectric composite inks in-between [20]. After being extruded out of the nozzle, the filament exhibits the desired configuration: the silver electrodes are formed on a small region on the outer surface of the piezoelectric filament.

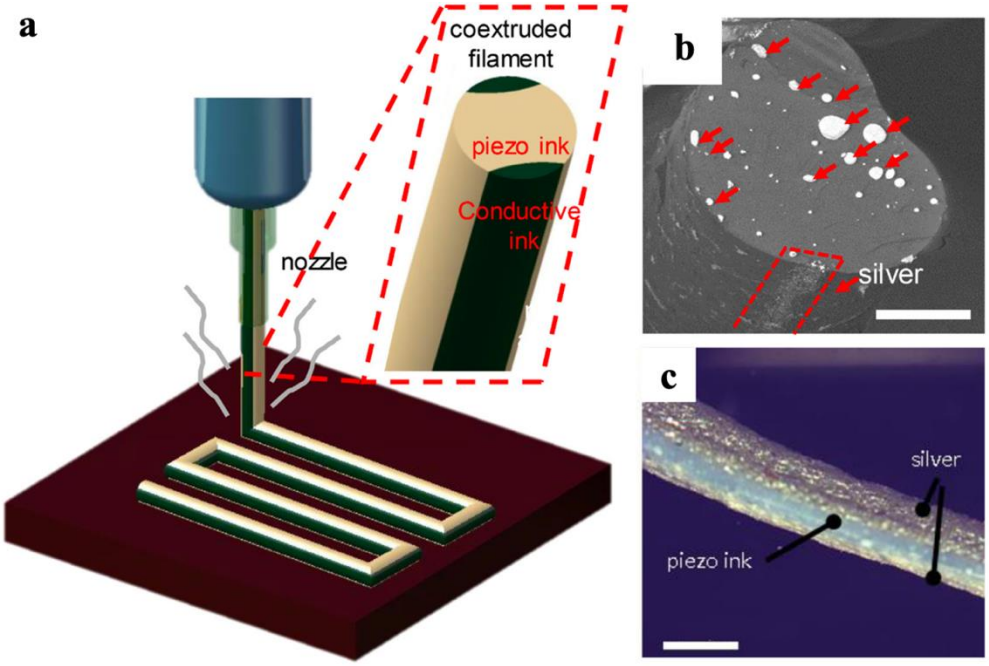

Figure 2.14 (a) Schematic of the co-extrusion solvent evaporation-assisted DIW process. (b) SEM, and (c) Microscopic images of the co-extruded filament. Scale bar, 500 μm and 1 mm, respectively [20].

Zhou *et al*. used two solvent evaporation-assisted DIW printing heads in their work to fabricate stretchable piezoelectric strain sensing and energy harvesting devices with electrodes. Figure 2.15 schematically illustrates the printing sequences to fabricate a piezoelectric strain device: print piezoelectric layer on a conductive indium tin oxide (ITO) coated glass substrate; print the top

electrode; polarize in the silicone oil bath; flip the direction of the printed part to print the bottom electrode. The piezoelectric ink was made of PVDF-TrFE/30 wt% $BaTiO_3$ composite dissolved in the DMF solvent, and the conductive ink was made of PVDF-TrFE/66 wt% silver flakes composites dissolved in the DMF solvent [21]. The fabricated strain gauge can be stressed under large strain up to 300% without degradation in piezoelectric voltage output. Similar to Bodkhe's work, highly toxic solvent DMF was used and the ink has a shelf life. Another drawback of this technique is that the printed structure needs to be flipped to print the bottom electrode.

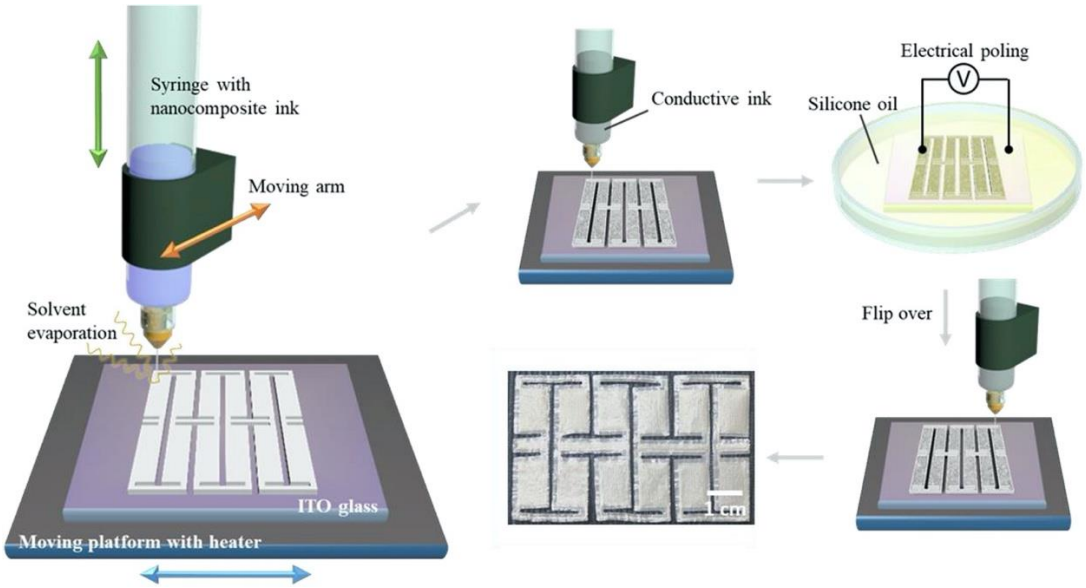

Figure 2.15 Schematic of the multi-material DIW 3D printing of a piezoelectric strain sensor: print piezoelectric ink on a conductive ITO glass; print the top electrode; poling process; flip the direction of the printed part to print the bottom electrode. [21].

Yan *et al*. also used two DIW printing heads in their work to fabricate flexible multi-layer piezoelectric grid with electrodes. Figure 2.16 schematically illustrates the printing sequences to fabricate a piezoelectric multi-layer grid [22]: one head was for printing top and bottom silver electrode layers; the other head was for printing PDMS/10 wt% PZT piezoelectric composite layers. The process does not require toxic solvent, and this technique could be further employed to fabricate geometrically more complex piezoelectric structures.

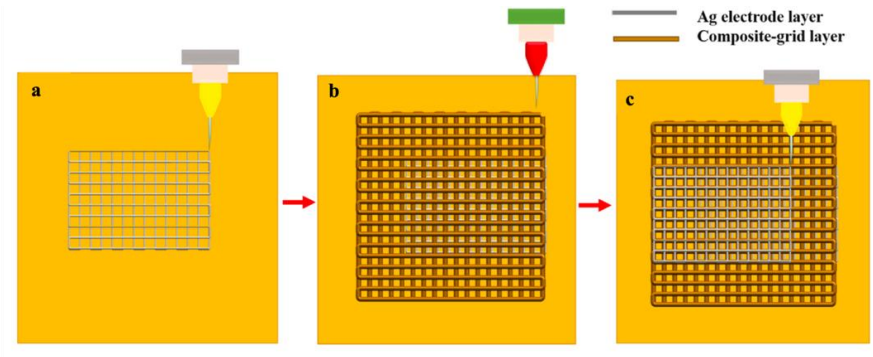

Figure 2.16 Schematic of the multi-material DIW 3D printing of a multi-layer grid: (a) bottom silver electrode, (b) middle piezoelectric composite grid, and (c) top silver electrode [22].

2.5 Summary of literature review

Flexible piezoelectric composite devices have emerged during the past decade to overcome the shortcomings of the piezoelectric polymers and ceramics. The working principle is to use the high piezoelectric property of the piezoelectric ceramic fillers while preserving the flexibility or extensibility of the polymer matrix. As reviewed in Section 2.3.2, conventional manufacturing methods for fabricating PVDF such as: solution casting, spin-coating, melt-extrusion, and electrospinning are also used with piezoelectric composite materials. However, these techniques limit the geometries into one-dimensional fiber or two-dimensional film. The advent of additive manufacturing technology enhances the possibilities of producing piezoelectric devices with complex geometries and designability as reviewed in Section 2.4.

The electrodes are usually fabricated by painting, sputtering, or attaching conductive tapes or fabrics on the piezoelectric sensing structures, which is separate from the piezoelectric element fabrication process. Also, the electrodes of the commonly used commercial PVDF film and PZT disc sensors tend to crack or wear in a short service time. Multi-material 3D printing technique shows a great potential to co-fabricate electrodes using the second printing head. So far, three studies have employed multi-material 3D printing technologies to fabricate piezoelectric composite devices with co-fabricated electrodes. Nevertheless, the geometries are limited into one-dimensional co-extruded fiber [20], two-dimensional multi-layer film [21], or simple 3D multi-layer scaffold [22]. The challenges existing in the manufacturing of piezoelectric devices have led

to the goal of this dissertation: develop geometrically more complex 3D flexible piezoelectric composite devices with integrated electrodes through multi-material 3D printing technique.

CHAPTER 3 RESEARCH OBJECTIVES AND COHERENCE OF ARTICLES

3.1 Problem identification

Multi-material three-dimensional (3D) printing technique shows a great potential for manufacturing piezoelectric structures with electrodes into a wide range of sensing and energy harvesting applications. However, the following issues concerning this approach need to be solved:

- Piezoelectric polymer polyvinylidene fluoride (PVDF) has not been used in the multi-material fused filament fabrication (FFF) 3D printing process.
- In previous studies, the multi-material 3D printed piezoelectric devices with co-fabricated electrodes were mainly in 1D fiber, 2D film or simple 3D scaffold shapes.
- Multi-material freeform or conformal 3D printing of piezoelectric devices with electrodes has not been previously developed, while many of the sensing and energy harvesting applications could highly benefit from freeform or conformal shapes.

3.2 Research objectives

The main objective of this research is to design and fabricate 3D flexible piezoelectric devices with co-fabricated electrodes based on a multi-material 3D printing technique. The specific objectives are presented as the following:

I. **Verify the suitability of piezoelectric polymer PVDF to be used in the multi-material 3D printing process:** fabricate PVDF films using a FFF 3D printer; tailor the stretching parameters to increase electroactive β phase content (F_β) and poling parameters to increase piezoelectric coefficient d_{33}; characterize the sensing and energy harvesting behaviors of the fabricated PVDF films.

II. **Develop 3D flexible piezoelectric composite lattices based on multi-material FFF 3D printing technique:** develop a flexible piezoelectric composite filament by incorporating high piezoelectric ceramic lead zirconate titanate (PZT) particles into a flexible polymer thermoplastic polyurethane (TPU); multi-material 3D printing of different types of piezoelectric composite lattices made of the developed piezoelectric composite filament

and the commercial conductive TPU/carbon black composite filament; tailor the poling parameters to increase piezoelectric coefficient d_{33}; compare the piezoelectric performance of the 3D piezoelectric composite lattices in two conditions: under the same maximum applied force and under the same maximum imposed displacement; use finite element analysis (FEA) method to compare the piezoelectric voltage output of the octet truss and a fully dense solid sample under the same maximum applied force; fabricate sensing and energy harvesting demonstrators to prove the concept.

III. **Use a supporting fluid-assisted multi-material 3D printing technology to fabricate flexible conformal and freeform piezoelectric composite sensors:** develop a mineral oil/fumed silica supporting fluid; characterize the rheological and support behaviors of the supporting fluid; develop thermoset-based piezoelectric and conductive composite inks that are thermally cured; characterize piezoelectric and conductive, rheological, morphological and mechanical properties of the ink materials; multi-material direct-ink writing (DIW) 3D printing of a multi-layer planar film, a conformal non-planar hemisphere and a freeform spiral-hexagon in the supporting fluid and characterize their piezoelectric performance.

3.3 Coherence of articles

The main results of this research are presented in the form of submitted peer-reviewed journal articles in Chapter 4, 5, and 6, which achieve the above-mentioned research objectives I, II, and III, respectively.

Chapter 4 presents the article, "*Fused filament fabrication of PVDF films for piezoelectric sensing and energy harvesting applications*", published in Materials Advances on May 2 2022. In this work, FFF printed PVDF films were stretched at a stretching ratio of 4 and polarized under an electric field of 30 V/μm using a custom-made poling setup. The obtained PVDF films possess a d_{33} of 7.29 pC/N and a F_β of 65 %, which is ~10 – 100 times higher than the related published works. The fabricated PVDF films were tested for two sensing applications: cantilever bending and compression tests, and for one wind energy harvesting application. Mrs. Tao designed and carried out the experiments, analyzed the data, and drafted the article under the supervision of Prof. Therriault and Prof. Akbarzadeh. Mr. Shi assisted in the stretching process of the PVDF films with the help of Mrs. Tao. Mr. Rafiee advised on the experiment and the draft.

Chapter 5 presents the article, "*Multi-material fused filament fabrication of flexible 3D piezoelectric nanocomposite lattices for pressure sensing and energy harvesting applications*", submitted to Applied Materials Today on April 19 2022. In this work, four types of 3D piezoelectric composite lattices: simple cubic (SC), body-centered cubic (BCC), cuboctahedron (CH) and octet truss (OT) (and one fully dense solid (FD) for benchmark) were designed and fabricated based on multi-material FFF 3D printing technique. Piezoelectric TPU/30 vol% PZT and a commercial conductive TPU/carbon black composite filaments were used to fabricate the piezoelectric structures and electrodes, respectively. The piezoelectric performance of the 3D piezoelectric composite lattices was compared. The OT lattice and FD sample were compared using both the experimental and finite element analysis (FEA) methods. The OT lattice shows the highest voltage output under the same maximum applied force, which is ~ twice the value of the FD sample. A multi-material OT piezoelectric composite shoe sole was fabricated as a demonstrator, it generates a high peak-to-peak voltage of ~ 20 V by a single human stomping. Mrs. Tao designed and carried out the experiments, analyzed the data, and drafted the article under the supervision of Prof. Therriault and Prof. Akbarzadeh. Mr. Shi designed the four types of lattices and conducted the FEA. Mrs. Granier assisted Mrs. Tao with the fabrication of piezoelectric composite filament, samples for mechanical and piezoelectric tests. Mr. Moeini designed the PLA foot replica and assisted Mrs. Tao with the cyclic compression test on the multi-material OT composition shoe sole.

Chapter 6 presents the article, "*Multi-material freeform 3D printing of flexible piezoelectric composite sensors using a supporting fluid*", submitted to Additive Manufacturing on March 25 2022. In this work, a multi-material freeform 3D printing process was developed for the manufacturing flexible piezoelectric structures with electrodes. During the printing process, the developed mineral oil/fumed silica supporting fluid with the appropriate yield strength can support the deposited filament. We used two DIW printing heads: one is for PDMS/30 vol% PZT composite ink to fabricate the piezoelectric structures; the other is for PDMS/25 vol% silver (Ag) composite ink to fabricate the electrodes. Three demonstrators: a multi-layer planar film, a conformal non-planar hemisphere, and a freeform spiral-hexagon structure were fabricated and tested. Mrs. Tao designed and carried out the experiments, analyzed the data, and drafted the article under the supervision of Prof. Therriault. Mrs. Granier assisted Mrs. Tao with the ink development, samples fabrication and characterization processes, and some of the results analysis.

CHAPTER 4 ARTICLE 1: FUSED FILAMENT FABRICATION OF PVDF FILMS FOR PIEZOELECTRIC SENSING AND ENERGY HARVESTING APPLICATIONS

Rui Tao[1,2], Jiahao Shi[2,3], Mohammad Rafiee[1,2], Abdolhamid Akbarzadeh[2,3,4] and Daniel Therriault[1,2*]

[1] Laboratory for Multiscale Mechanics (LM^2), Department of Mechanical Engineering, Polytechnique Montreal, Montreal, QC, H3T 1J4, Canada

[2] Research Center for High Performance Polymer and Composite Systems (CREPEC), Montreal, QC, H3T 1J4, Canada

[3] Advanced Multifunctional and Multiphysics Metamaterials Laboratory (AM^3L), Department of Bioresource Engineering, McGill University, Montreal, QC, H9X 3V9, Canada

[4] Department of Mechanical Engineering, McGill University, Montreal, QC, H3A 0C3, Canada

Published in Materials Advances on May 2nd, 2022

Abstract

Fused filament fabrication (FFF) of piezoelectric polymer polyvinylidene fluoride (PVDF) provides a simple manufacturing technique for the creation of lead-free piezoelectric devices compared to the traditional manufacturing methods, such as large-scale film extrusion and solution casting. Here, we investigate the effects of the stretching and the poling parameters on the enhancement of piezoelectric performance of the printed PVDF films. The stretched and polarized PVDF films with a dimension of 40 × 20 × 0.06 mm (length × width × thickness) possess a piezoelectric charge coefficient (d_{33}) of 7.29 pC/N and a fraction of β phase (F_β) of 65 % at a stretching ratio (R) of 4 after being polarized under an electric field of 30 V/μm. The resulting d_{33} of the fabricated PVDF films has been substantially enhanced by ~ 10-100 times higher than the related reported values of the FFF printed PVDF films. The fabricated PVDF films are capable of detecting compression (d_{33}) and vibration (d_{31}). By blowing four piezoelectric films connected in parallel for 3 min, the energy stored in the capacitor can make a red LED blink. Our fabricated piezoelectric PVDF films could be used in the field of pressure sensing, vibration sensing and energy harvesting applications.

4.1 Introduction

Piezoelectric materials are used in various applications such as in pressure sensing,[1,2] strain sensing,[3,4] actuation[5,6] and energy harvesting[7,8] because of their capabilities of converting mechanical energy to electrical energy and vice versa.[9,10] Compared to the high piezoelectric ceramics such as lead zirconate titanate (PZT) and barium titanate ($BaTiO_3$), the piezoelectric polymer polyvinylidene fluoride (PVDF) has been increasingly used owing to its lightness, high flexibility, durability and biocompatibility.[11,12] PVDF is a semicrystalline polymer with a repeating unit of $CH_2{-}CF_2$ monomer.[13] It has two main phases: non-polar α phase and polar β phase.[14,15] The dipole moments in PVDF originate from its high electronegativity of fluorine atoms and smaller electronegativity of hydrogen atoms.[16,17] The α phase with a trans-gauche-trans-gauche' (TGTG') conformation is not piezoelectric as a result of the cancellation of the dipole moments, while β phase with an all trans (TTTT) conformation possesses the largest polarization due to the alignment of the dipole moments in the same direction.[15] However, PVDF usually crystallizes into the thermally stable α phase.[19,20] Several methods have been used to induce the conversion from the α phase to β phase such as mechanical stretching[21–23] and hot-pressing.[24,25] In addition to the requirement of high content of β phase (F_β) in PVDF, an electrical poling treatment is often essential to align the randomly dispersed β phase in order to obtain a net polarization.[26–29] Poling parameters (e.g. time, temperature and poling voltage) have to be properly adjusted in order to maximize the poling process efficiency.[30,31] Piezoelectric strain coefficient (d_{31} and d_{33}) with double subscripts is used to illustrate the piezoelectric performance: the first subscript indicates the direction of the charge generation, and the second subscript indicates the direction of the applied mechanical strain.

Over the past decade, additive manufacturing technology (or 3D printing) has increasingly been utilized to fabricate smart materials including piezoelectric materials.[1,2,32–39] The traditional manufacturing methods for the creation of PVDF films such as solution casting[40–42] and electrospinning[43–45] require toxic solvent, while extrusion molding[19,42] requires careful control on the melt temperature and the material feeding rate. Thus, fused filament fabrication (FFF) offers a maneuverable and eco-friendly approach for fabrication of piezoelectric PVDF devices, i.e., recyclable and no need of toxic solvent. Several studies demonstrated FFF 3D printing of piezoelectric PVDF films. Lee *et al.*[35] and Kim *et al.*[33] integrated FFF 3D printing and electrical

poling steps to achieve one-step fabrication of piezoelectric PVDF films. Porter *et al.*[32] investigated the effects of printing parameters on the piezoelectric performance of the PVDF films. However, the reported piezoelectric coefficient of these works (Kim *et al.*[33]: d_{33} = 0.048 pC/N; Porter *et al.*[32]: d_{31} = 1.19 pC/N) are much lower than the commercial hot-pressed piezoelectric PVDF films, which is 28-32 pC/N.[46] In addition, some researchers incorporated the fillers to induce the creation of β phases in the FFF 3D printed PVDF films. Pei *et al.*[47] added 5 wt% tetraphenylphosphonium chloride (TPPC) nano particles to obtain 83.8 % β phases, while 28.9% of β phase content for pure PVDF. Liu et al.[48] enhanced the β phase content of PVDF filament to 93 % by adding 15 wt% ionic liquid comparing to only 13.5% of the β phase in pure PVDF.

Our novel strategy in this work is to fabricate piezoelectric PVDF films with highly enhanced d_{33} compared to the related reported values[33] using the facile FFF 3D printing technique and two tailored post-treatments: mechanical stretching and electrical poling. Four different stretching ratios (R = final length/original length, R = 1, 2, 3 and 4) are investigated to achieve the high polar β phase content. We then used the polarized printed piezoelectric PVDF films in three applications: a frequency detector, a pressure sensor and energy harvesters to convert wind energy to electricity. We believe that FFF 3D printing technology with the proper post-treatments investigated herein is promising for the construction of flexible PVDF piezoelectric sensors and energy harvesters for more advanced applications in areas ranging from medical to aerospace and beyond.

4.2 Results and discussion

Figure 4.1a-c schematically shows the fabrication process of a piezoelectric PVDF film based on FFF printing, stretching (R = 4) and poling processes. The FFF printed one-layer PVDF films are stretched along the printing direction at R = 4 (i.e., from 4 cm to 16 cm) to induce β phase (Figure 4.1a and 4.1b). Then, the stretched PVDF films are cut to 40 × 20 mm and polarized along the thickness direction by a contact poling setup to align the randomly oriented dipole moment (Figure 4.1c). Figure 4.1d shows the photo of the printed PVDF films (60 × 40 × 0.15 mm). For an efficient performance, the FFF printed PVDF films have to be free of porosities or impurities, otherwise a premature breakage during the mechanical stretching process or a permanent electrical breakdown during the poling process could happen. In case of an electrical breakdown, the piezoelectric element could not be further polarized and the piezoelectricity will remain very low.

Undesired porosities or impurities can be created during the filament preparation and/or the FFF printing process. First, the as-received printing filament should be with the least content of bubbles and impurities. Second, the PVDF filaments were dried in the oven to minimize their moisture content and the pores in the printed parts. Meanwhile, we slightly decrease the extrusion width to make sure there is no gap between the printed lines (Figure 4.7, Supporting Information). A fabricated PVDF film with electrical connections is shown in Figure 4.1e. The optical image of the cross-section of the piezoelectric PVDF film with electrodes shown in Figure 4.1f illustrates that the average thickness of the piezoelectric PVDF film after being stretched at $R = 4$ is ~ 60 μm and the average thickness of the painted silver electrodes on each side is ~ 15 μm. The photo and the thickness of the PVDF films stretched at $R = 1$, 2 and 3 are shown in Figure 4.8 and listed in Table 4.2 in the Supporting Information.

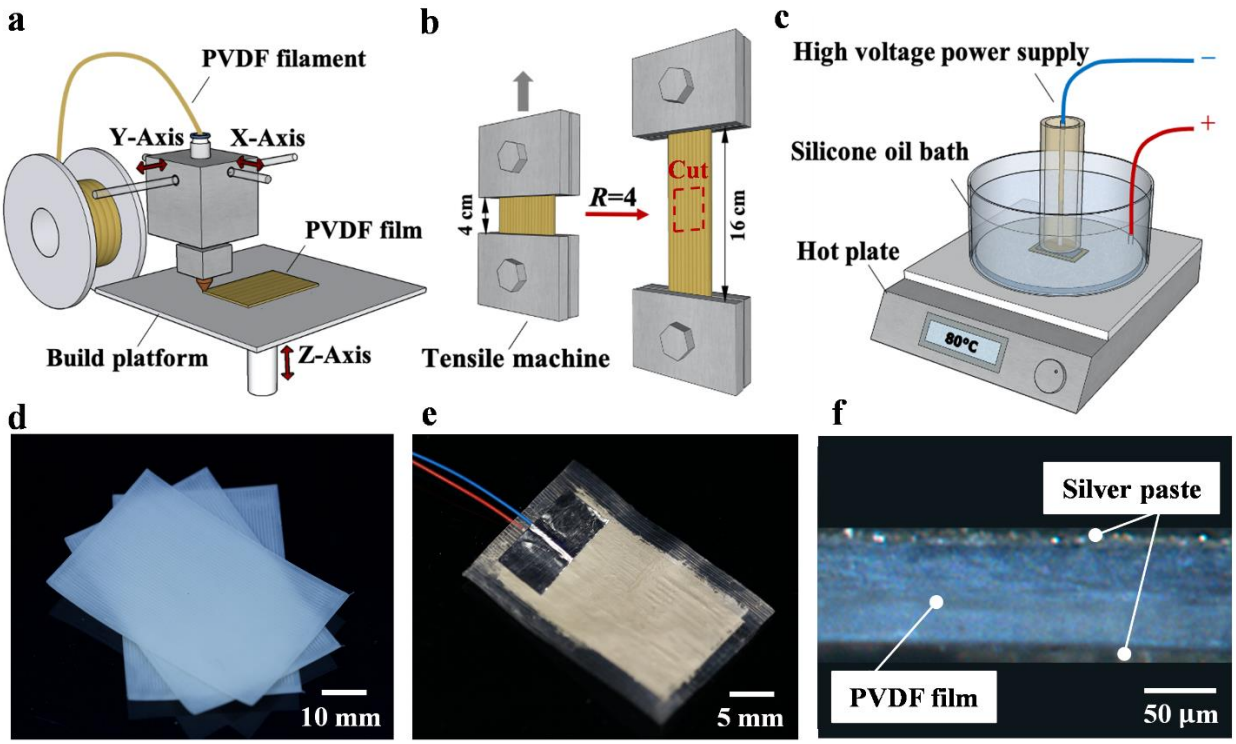

Figure 4.1 Fabrication of the piezoelectric PVDF films. Schematic of the (a) FFF printing process of the PVDF films (60 × 40 × 0.15 mm). (b) Stretching process of the printed PVDF films (R = 4). (c) Contact poling process of the stretched PVDF films (40 × 20 × 0.06 mm). Photos of (d) FFF printed PVDF films. (e) A piezoelectric PVDF film with electrical connections. (f) Optical image of the cross-section of the piezoelectric PVDF film.

Poling voltage, time and temperature are the three main poling parameters that influence the piezoelectric properties of polarized PVDF films. Poling voltage should be sufficiently high to align the dipole moments, while poling time should be optimized to ensure the complete polarization in the shortest time. An elevated poling temperature is used to increase the mobility of the PVDF molecules. Figure 4.2a-c show that the d_{33} of the printed PVDF films (R = 4) and the commercial unpolarized PVDF films with respect to poling voltage, time and temperature, respectively. In Figure 4.2a, d_{33} values of both printed (R = 4) and commercial PVDF films increase rapidly and then reach a plateau value with the enhancement of poling voltage (poling temperature = 80°C and poling time = 60 min). For the commercial stretched PVDF films, under the highest poling voltage value of 6 kV, which is approximately 50 V/μm electric field, the maximum d_{33} value of 32.41 pC/N is reached, consistent with the reported d_{33} value (32 pC/N) of the commercial polarized PVDF film measured by a d_{33} meter.[46] Electrical breakdown happens at ~ 7 kV as marked in blue. The printed PVDF films (R = 4) can hold the maximum poling voltage of 2 kV, which is approximately 30 V/μm electric field and leads to a maximum d_{33} value of 7.29 pC/N. Electrical breakdown of PVDF film happens at 3 kV as marked in red. The maximum poling electric field of the printed PVDF films (R = 4) is less than the commercial PVDF films due to the fact that the thinner section between the extruded lines in the printed PVDF films (Figure 4.7, Supporting Information). In Figure 4.2b, d_{33} of both printed (R = 4) and commercial PVDF films increase rapidly and then reach a plateau value with the poling time (poling temperature = 80°C, poling voltage = 50 V/μm (commercial PVDF) and 30 V/μm (printed PVDF)). For both commercial and printed PVDF films, the d_{33} value increases with poling time until 60 min. The d_{33} is almost constant for poling time beyond 60 min probably due to the completion of the alignment of the dipole moments in that period. In Figure 4.2c, d_{33} of both printed (R = 4) and commercial PVDF films increase until 80°C and then drop down with the increase of poling temperature (poling time = 60 min, poling voltage = 50 V/μm (commercial PVDF) and 30 V/μm (printed PVDF)). We observe that the highest d_{33} value is achieved at 80°C. Below 80°C, the PVDF molecules are inactive, so it could not be reoriented efficiently along with the electric field.[49] However, when the poling temperature is above 80°C, we observed that the PVDF films significantly warp and detach from the bottom poling plate, so the poling electric field cannot be uniformly applied on the PVDF films. The investigation on the poling parameters for the commercial PVDF films suggest that the

optimal poling settings are 80°C, 50 V/μm and 60 min. However, the printed PVDF films could not sustain more than 30 V/μm because of the thinner area between printed lines. Thus, the optimal poling settings for the printed PVDF films are 80°C, 30 V/μm and 60 min. In the d_{33} measurement, three specimens are tested and each specimen is measured at three different locations. We found that the error bar of the specimens polarized at the same conditions is too small to be detected, which indicates the PVDF films have been uniformly polarized.

We investigate the effect of R on the creation of piezoelectric β phases in the printed PVDF films. The photos and the dimensions of the printed PVDF films stretched at R=1, 2, 3 and 4 are shown in Figure 4.8, Supporting Information. The FTIR spectra of the polarized printed PVDF films stretched at R = 1 to 4 are shown in Figure 4.2d. Herein, 840 cm^{-1} is the characteristic peak of piezoelectric β phase, while 613, 713, 795 and 975 cm^{-1} are the representative peaks of piezoelectric α phase. With the increase of R, the peaks of α phase decreases, while the peak of β phase increases, meaning that the printed PVDF films transform from α phase to β phase. For a system containing α and β phases, the modified Beer-Lambert law is used to calculate F_β (%):

$$F_\beta\,(\%) = \frac{A_\beta}{1.26A_\alpha + A_\beta} \tag{4-1}$$

where A_α and A_β are the absorbance of α and β phases at 763 and 840 cm^{-1}, respectively, and 1.26 is the ratio of absorption coefficient at the corresponding wavenumber of 6.1×10^4 and 7.7×10^4 cm^2mol^{-1} for α and β phases, respectively.[19,50] Three specimens are prepared for each stretching condition and F_β (%) and d_{33} of each specimen is measured at three different locations. As shown in Figure 4.2e, F_β (%) and d_{33} increase with the value of R. The unprinted PVDF filament and the printed PVDF films stretched at R = 1 have a similar low F_β (%) and d_{33}, indicating that 3D printing process cannot efficiently convert α phase to β phase in PVDF. Both F_β (%) and d_{33} increase with R, which means that stretching process is necessary for achieving a higher piezoelectric performance. The polarized printed PVDF films possess a F_β (%) of 65% and a d_{33} of 7.29 pC/N, which is ~ 10 - 100 times higher compared to the previously reported FFF 3D printed PVDF films (Kim *et al.*[33]: d_{33} = 0.048 pC/N; Porter *et al.*[32]: d_{31} = 1.19 pC/N). However, the piezoelectric performance of the printed PVDF films is still lower than that of the commercial one for the following two reasons: in the stretching process, when R > 4, our printed PVDF films rupture, while the commercial films had already been stretched at R = 5. The utilization of a lower R value

is due to the relatively weak interface between the printed lines that makes the printed films fail prematurely. Thus, the fraction of the piezoelectric β phase of our stretched PVDF film is ~10% lower than the commercial one. Also, the interface between the printed lines, the surface roughness and the interfilament porosities have an adverse effect during the poling phase. In addition, we compare F_β (%) of the printed PVDF films and the commercial PVDF films before and after the poling process with their respective optimal poling parameters (Figure 4.2f). For both PVDF films, F_β (%) has not been much enhanced by the poling step. The commercial PVDF films have a slightly higher F_β (%) than the printed PVDF films owing to the hot-pressing process and the higher R (R = 5) during the stretching process. In conclusion, stretching process creates higher F_β (%) and poling process aligns β PVDF molecules to achieve a non-zero net polarization. In addition, we heat the polarized printed PVDF films at 30, 40, 50, 60, 70, 80, 90 until 100°C. Below 60°C, d_{33} is stable. Above 60°C, d_{33} decreases with increasing temperature due to the misalignment of the PVDF molecules, i.e., losing its net polarization. Thus, the maximum allowable operating temperature for the FFF printed piezoelectric PVDF films developed in this work is 60°C as shown in Figure 4.9,Supporting Information.

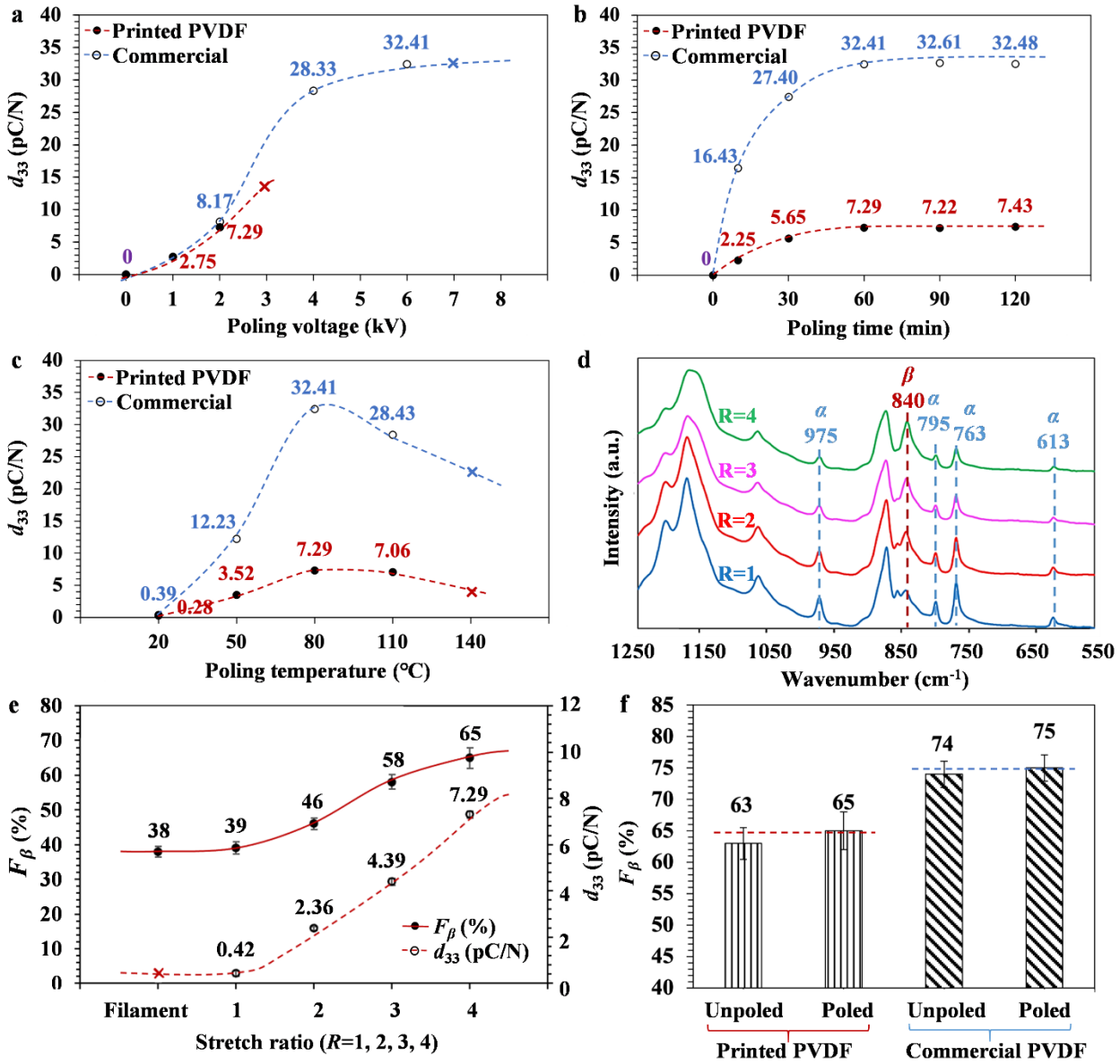

Figure 4.2 Investigation of the optimal poling and stretching parameters by characterizing and comparing the piezoelectric behaviors of printed PVDF films fabricated in this work and stretched commercial hot-pressed PVDF films. (a) d_{33} of commercial and printed (R = 4) PVDF films polarized under different poling voltages: 2, 4, 6 and 7 kV (for commercial PVDF); 1, 2 and 3 kV (for printed PVDF) (red and blue markers represent electrical breakdown). (b) d_{33} of commercial and printed (R = 4) PVDF films polarized for different poling time: 30, 60, 90 and 120 min. (c) d_{33} of commercial and printed (R = 4) PVDF films polarized at different poling temperature: room temperature, 50, 80, 110 and 140°C (red and blue markers represent electrical breakdown). (d)

FTIR spectrum, (e) F_β (%) and d_{33} of unprinted PVDF filament and polarized printed PVDF films stretched at R=1, 2, 3 and 4. (poling parameters: 80°C, 30 V/μm and 60 min) (f) Comparison of F_β (%) of printed PVDF films fabricated in this work (R=4) and commercial PVDF films before and after the poling process.

We chose 40 × 20 × 0.06 mm polarized printed piezoelectric PVDF films (R = 4; polarized at 80°C, 30 V/μm for 60 min) for the demonstration of two sensing (cantilever bending - d_{31} mode and compression tests - d_{33} mode) and one energy harvesting applications:

Application #1: Cantilever for bending frequency sensing application. A cantilever bending test setup (Figure 4.3a) is designed to evaluate the frequency detection behavior of the printed piezoelectric PVDF sensor. The shaker and the aluminum beam are fixed on a steel support and connected to a rod. The screwed rod moves back and forth in the x direction and bends the aluminum beam. The printed piezoelectric PVDF sensor is attached near the clamped end of the aluminum beam. The cantilever bending test was also recorded by the high-speed camera as shown in Supplementary information: Movie S1. The shaker is excited by a function generator (in sine wave format) at eight frequencies (i.e., 0.1, 0.5, 1, 5, 10, 20, 30 and 40 Hz) and the deflection of the free end of the aluminum beam is held constant at +5 / 0 mm. To validate the durability of the printed piezoelectric sensor, we performed the cyclic test at 5 Hz for around 8 h and captured the voltage at the beginning and at the end of the cyclic test for 1200 s, respectively. The printed piezoelectric PVDF sensor still shows good sensitivity and favorable stability for more than 140,000 cycles (Figure 4.3b). Figure 4.3c shows the voltage generated from the printed piezoelectric film sensor in a period of 1 s between 0.1 and 40 Hz. The measured peak-to-peak voltage is ~ 0, 9, 39, 35, 29, 6, 2 and 0 mV. The highest peak-to-peak voltage output of ~ 39 mV is observed at 1 Hz. The peak-to-peak voltage increases from 9 to 39 mV as the frequency increases from 0.5 to 10 Hz and then decreases to 2 mV as the frequency increases from 10 to 30 Hz. The detected frequency by the printed piezoelectric sensor is consistent with the related actuating frequency between 0.5 to 30 Hz. The output voltage signal is close to zero below 0.5 Hz and above 30 Hz. Below 0.5 Hz, the movement is too slow to be detected. The reason is that the piezoelectric sensors are good at dynamic force measurement instead of static force measurement due to the fact that the surface charges are easily neutralized under the static force.[51] Above 30 Hz (i.e., frequency = 40 Hz), the piezoelectric PVDF sensor do not have enough time to transmit the charges generated

from the bending movement in the positive *x* direction (forward); these charges are reversed by the recovering movement in the negative *x* direction (back).

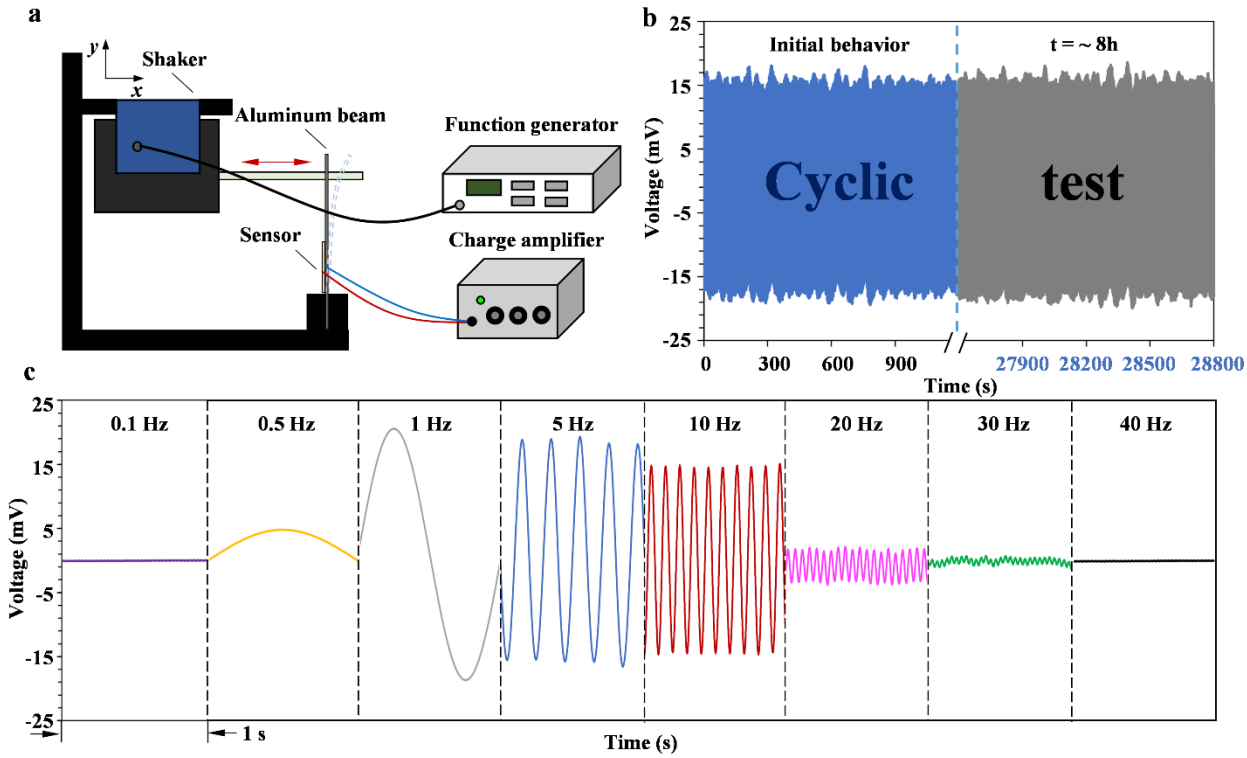

Figure 4.3 Cantilever bending test at different frequencies actuated by a shaker. (a) Schematic of the cantilever bending test setup. (b) Durability test for a polarized printed PVDF film sensor (R = 4) by continuously bending at 5 Hz for 144,000 cycles. The voltage generated in 1200 s intervals at the beginning and after 8 h. (c) Voltage generated by a polarized printed piezoelectric PVDF sensor (R = 4) at different actuating frequencies: 0.1, 0.5, 1, 5, 10, 20, 30 and 40 Hz.

Application #2: Compression sensing application. The schematic of the compression test setup is shown in Figure 4.4a. During the test, the compression head goes down by 0.033, 0.056, 0.079, 0.101, 0.129, 0.159, 0.206 and 0.234 mm to reach the maximum compressive force: 100, 200, 300, 400, 500, 600, 700 and 800 N, respectively. The voltage curves of the printed piezoelectric PVDF sensor under the compressive force between 0 to 700 N during a 1 s interval is shown in Figure 4.4b. The PVDF films rupture when the load is equal to or greater than 800 N. As the compressive force increases, it takes longer time for the voltage signal to go back to zero. Figure 4.4c depicts a linear response of the PVDF film sensor voltage output for the force range between 0 to ~ 700 N.

The sensitivity of the sensor is ~ 9.717 mV/N. Then, we reversed the direction of the connection by switching the positive and negative wires on the piezoelectric sensor, and compressed the piezoelectric sensor with a load of 500 N. We observe that the direction of the voltage peak has been reversed, but the amplitude of two peaks is very close with a 0.8% difference, which confirms that the voltage comes from the piezoelectric sensor and not from the movement of the wires due to the change of the capacitance (Figure 4.4d).

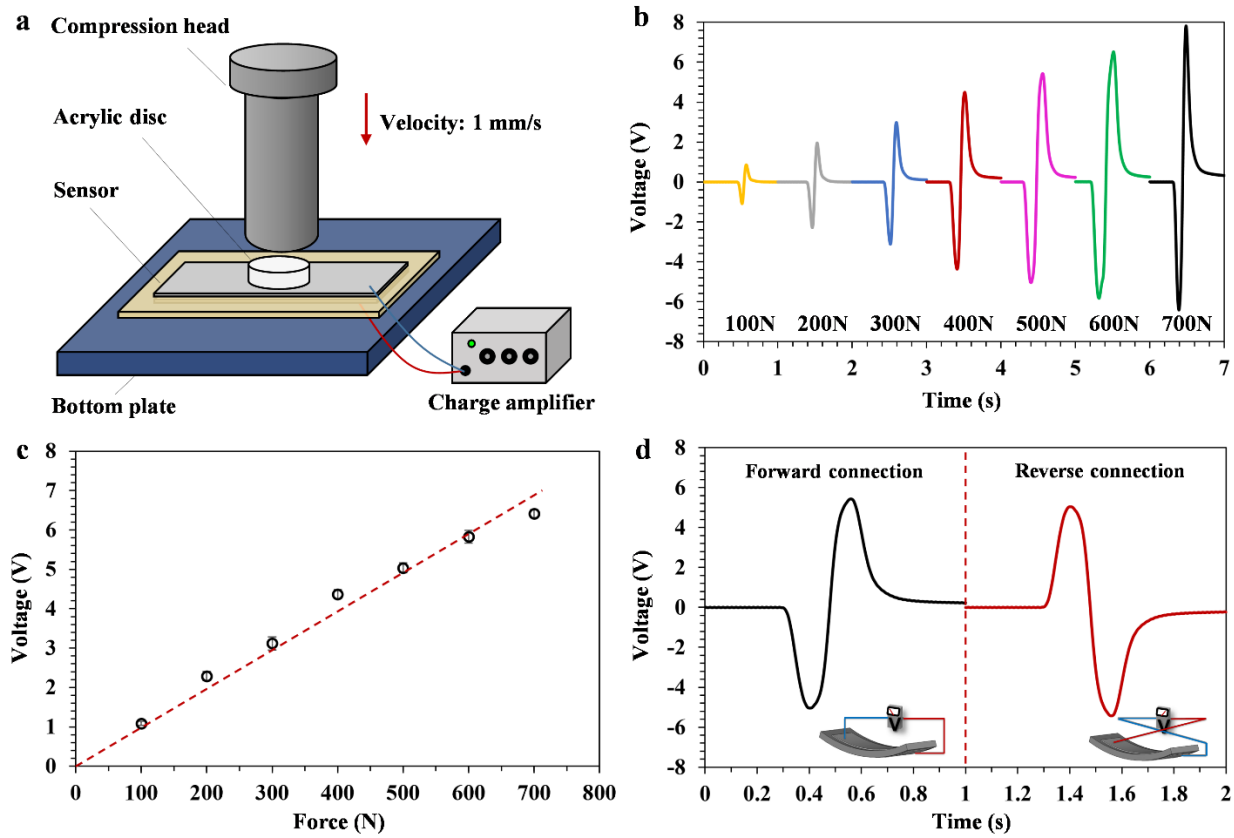

Figure 4.4 Compression test. (a) Schematic of the compression test setup. (b) Voltage curves during a 1 s period, (c) Maximum voltage generated by a 40 × 20 mm printed piezoelectric PVDF sensor (R = 4) under the maximum compressive force of 100, 200, 300, 400, 500, 600 and 700 N, respectively. Error bars indicate the standard deviations obtained from three measurements. (d) Switching-polarity test: voltage generated during a 1 s period under the compression of 500 N using forward and reverse connections.

Application #3: “Piezo leaves” for energy harvesting application. As shown in Figure 4.5a, four 40 × 20 × 0.06 mm printed polarized piezoelectric PVDF sensors (R = 4) are connected in parallel and glued on an FFF 3D printed PLA tree as energy harvesting “piezo leaves”. Figure 4.5b shows a bridge-rectifier circuit used to convert the AC to DC to charge a 2.2 μF capacitor.[52] In the energy harvesting test, we use a table fan to blow the “piezo leaves” (Figure 4.5c). The distance between the fan and the PLA tree is 10 cm. As we turn on the table fan to the highest speed (motor speed = 1500 rpm), the “piezo leaves” are bent, thus generating electric current. We record the voltage reading of the capacitor on the multimeter every 30 sec. During a 3-min period of fan blowing, the “piezo leaves” are able to charge the capacitor from 0 to ~ 2 V at a charging rate of ~ 667 mV/min. After we turn off the fan, the voltage drops gradually due to the intrinsic current leakage behavior of the capacitor (Figure 4.5d). A 2.2 μF capacitor is selected in order to balance the current leakage rate and the charging rate. Larger capacitors have a higher charging rate but larger current leakage. The charges stored in the capacitor is further used to make a red LED bulb blink (Supplementary information: Movie S2). The number of “piezo leaves” and the amplitude of wind power have a significant effect on the charging rate. By calculation, ~ 720 pieces of “piezo leaves” are required to light a LED continuously.

As shown in Figure 4.10 (Supporting Information), the calculated power density of the four “piezo leaves” is ~ 9.38 μWcm^{-3} at a resistance of 1 MΩ (although there is a small deformation under the wind), which is comparable to the power density of the PVDF related energy harvesters from other works.[53-55]

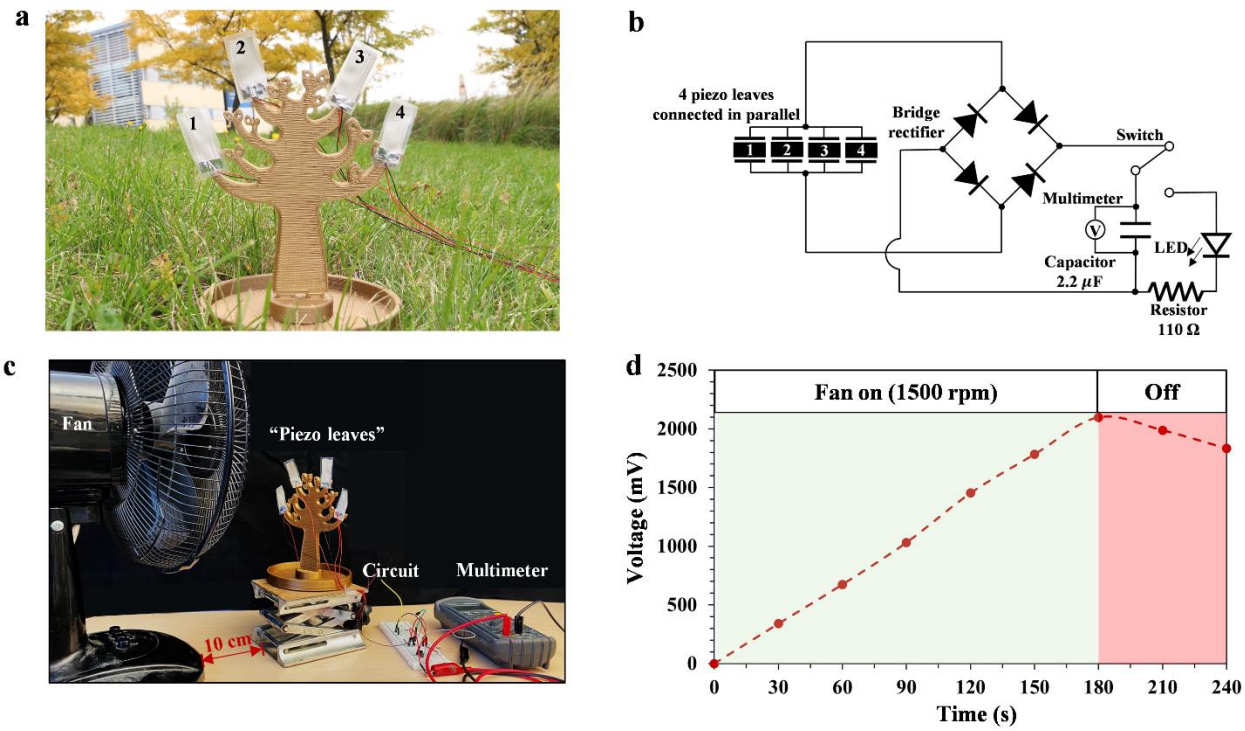

Figure 4.5 "Piezo leaves" energy harvester - Four PVDF films connected in parallel blown by a fan. (a) Photo of the four 40 × 20 mm printed piezoelectric PVDF sensors (R = 4) glued on an FFF 3D printed PLA tree. (b) Circuit diagram of the energy harvester: four "piezo leaves" connected in parallel generate AC, which is converted to DC by a bridge rectifier and stored in a capacitor to light a LED bulb. (c) Photo of the experimental setup: the wind energy from the fan is converted to electrical energy by four "piezo leaves" and the stored voltage in an energy harvesting circuit is read by a multimeter. (d) Voltage of a 2.2 μF capacitor charged by the "piezo leaves" after the fan is turned on (1500 rpm) for 3 min and off.

4.3 Conclusion

In summary, we have successfully optimized the stretching-poling post-treatment parameters to fabricate FFF printed piezoelectric PVDF films and tested them for frequency sensing, presure sensing and energy harvesting applications. By tailoring the stretching and poling parameters, a piezoelectric coefficient of 7.29 pC/N and a fraction of β phase of 65% were obtained. We find that the stretching step is necessary for the creation of piezoelectric β phase, while the poling step is required to align the randomly dispersed dipole moment. The d_{33} of the polarized printed PVDF

films (R = 4; polarized at 80°C, 30 V/μm for 60 min) fabricated in this work is ~ 10-100 times higher than the reported values.[32,33] We have successfully demonstrated that the fabricated PVDF films could be directly used in both d_{31} and d_{33} mode sensing applications, including frequency (0.5 to 30 Hz) and compression detection (0 to 700N). Moreover, 2 V voltage generated and stored in a 2.2 μF capacitor through a 3-min fan blowing of four printed PVDF films connected in parallel could make a LED bulb blink. In the future work, to further enhance the piezoelectric charge coefficient of the 3D printed piezoelectric films, high piezoelectric ceramic fillers can be incorporated into the pure PVDF filament as piezoelectric composite filament. The obtained piezoelectric coefficient will be the sum of the PVDF polymer matrix and the ceramic fillers. In addition, the stretching step is essential to enhance the β phase content in PVDF to achieve better piezoelectric performance, however it limits the complexity of the manufacturable structures. In our future work, we will show the use of FFF 3D printing technique to fabricate geometrically-optimized true 3D piezoelectric composite devices. The present work is the foundation of our future work with the goal of showing the upper limit of piezoelectric performance that we can achieve in the FFF 3D printed PVDF films. Also, we plan to utilize a multi-material FFF 3D printing technique for the fabrication of the piezoelectric sensors with electrodes in a single step. This multi-material 3D printing technique will offer a facile way to create piezoelectric devices without the need of post metallization. We believe that FFF 3D printed piezoelectric devices would find enormous applications in sensing and energy harvesting fields.

4.4 Experimental section

4.4.1 Materials

PVDF filaments (1.75 mm in diameter, Fluorinar-H™ Kynar®) were purchased from Nile Polymers, Inc (USA). Commercially available unpolarized (R=5) and polarized (R=5) hot-pressed PVDF films with a thickness of ~ 120 μm were purchased from PolyK Technologies, LLC (USA).

4.4.2 FFF printing of PVDF films

PVDF films were fabricated using the commercially available 1.75 mm diameter PVDF filament. An FFF 3D printer (Raised3D Pro 2) was used to print one-layer film with a dimension of 60 × 40 × 0.15 mm. Table 4.1 lists the main printing parameters.

Table 4.1 FFF 3D printing parameters for making the PVDF films.

Parameters	Values
Nozzle size	0.4 mm
Bed temperature	100 ℃
Extrusion temperature	250 ℃
Printing speed	30 mm/s
Infill percentage	100%
Layer height	0.15 mm

4.4.3 Stretching process

The stretching process was carried out on the printed PVDF films using the tensile test machine (eXpert 2600, ADMET). The dimension of the PVDF film between the upper and lower grips was 40 × 40 × 0.15 mm. The stretching condition were at 100℃ in an environmental chamber (F-280DT, ADMET) and at stretching rate of 0.2 mm/s. Using other temperature (80 to 120℃) and speed (0.1 to 1mm/s) settings, the PVDF films used to crack during the stretching process. The stretching ratio was varied from 1 to 4. The PVDF films have a great tendency to crack during the stretching process if we stretch them with $R > 4$.

4.4.4 Poling process

We built a contact poling setup to align the dipole moments of PVDF films, which consisted of three parts: an in-house-designed poling chamber, a high voltage power supply (ES60kV negative,

10 Watt, Gamma High Voltage Research, Inc.) and a hot plate (Thermo Scientific™ SuperNuova+™, Fisher Scientific). (Figure 4.6, Supporting Information) The commercially available hot-pressed PVDF films were polarized to confirm the functionality of the in-house built poling setup.

Before the poling process, both the 3D printed and commercial PVDF films were cut into the same size 40 × 20 mm and attached with conductive aluminum tape (3M, USA) to both surfaces as poling electrodes. During the poling process, the specimen was clamped between the copper rod and the bottom aluminum plate. Then, the specimen was cooled down to room temperature before removing the electric field to reduce the misalignment of dipole moments. After the poling process, the aluminum tapes were removed, the films were washed with soap to remove the residue of silicone oil and dried at room temperature before painting the electrodes on their top and bottom surfaces.

To evaluate the poling performance of the contact poling setup, the unpolarized commercial stretched hot-pressed PVDF films are polarized using four poling voltages (2, 4, 6 and 8 kV) at 80°C for 60 min, four poling time (30, 60, 90 and 120 min) at 80°C under 6 kV and five poling temperature (room temperature, 50, 80, 110 and 140°C) under 6 kV for 60 min, respectively. To investigate the optimal poling condition for the printed PVDF films stretched at $R = 4$ (highest F_β), we further polarized them using three poling voltages (1, 2 and 3 kV) at 80°C for 60 min, four poling times (30, 60, 90 and 120 min) at 80°C under 2 kV and five poling temperatures (room temperature, 50, 80, 110 and 140°C) under 2 kV for 60 min, respectively. In addition, the printed PVDF films stretched at $R = 1$, 2 and 3 are also polarized with an electric field of 30 V/μm at 80°C for 60 min.

4.4.5 Electrode fabrication and electrical connection process

A bristle paintbrush was used to paint a thin layer of silver conductive paste (MG Chemicals 842AR, ABRA Electronics Corp.) on the top and bottom surfaces of the printed piezoelectric PVDF films as electrodes for the electromechanical measurement. We left a gap (~ 2 mm) between the edge of the silver electrodes and the edge of the PVDF films in order to avoid contact between the two electrodes. Then, two pieces of aluminum tapes (5 × 10 mm) were used to electrically connect the silver electrodes and the wires.

4.4.6 Piezoelectric property characterization

A d_{33} meter (YE2730, Sinocera Piezotronics, Inc.) was used to characterize the piezoelectric coefficient d_{33}. The specimens were tested approximately one day after the poling process. Because the d_{33} value measured immediately after the poling process is higher than the real value. In the cantilever bending and compression tests, open-circuit voltages were collected using a charge amplifier (Piezo Lab Amplifier, MEAS Specialties) in the voltage mode. The data was acquired with an NI-9239 data acquisition system attached to a USB carrier NI-9162 (National Instruments) and recorded using a custom LabVIEW interface.

4.4.7 Piezoelectric β phase characterization

A Fourier-transform infrared (FTIR) spectrometer (Nicolet 6700, Thermoscientific) was used to obtain the absorption spectra of different types of PVDF films at 8 cm^{-1} resolution from 550 to 1250 cm^{-1}. 128 scans were conducted on each sample and the average values were used to assess the different phases content.

4.4.8 Optical characterization

A Canon EOS Rebel T4i camera was used for the photography of the samples in this paper. Optical images of the cross-section of the PVDF sensors were taken using an optical microscope (BX-61, Olympus). A high-speed camera (MotionBLITZ Cube4, Mikrotron) captured cantilever bending test at a frame rate of 200 Hz.

4.4.9 Cantilever bending test

An aluminum beam with a dimension of 120 × 40 × 0.5 mm was fixed on a steel support and actuated in flexion by a shaker (K2004E01, Mode Shop Inc.). The span length is ~ 8 cm. The printed piezoelectric PVDF film were attached near the clamped end of the aluminum beam in order to exhibit maximum strain and detect the vibrating frequency. During the cantilever bending test, the shaker was excited by a function generator (Model 19, Wavetek Corp.) in a sine wave format at eight different frequencies: 0.1, 0.5, 1, 5, 10, 20, 30 and 40 Hz.

4.4.10 Compression test

Compression test of the printed piezoelectric PVDF films were carried out in an MTS Insight machine with a 1000 N load cell in compression mode (MTS 569332-01). The crosshead speed was 1 mm/s. An acrylic disc with a diameter of 10 mm was glued on top of the PVDF film to obtain the same contact area under compression. The compression head moved down 0.033, 0.056, 0.079, 0.101, 0.129, 0.159, 0.206 and 0.234 mm until the maximum compressive force of 100, 200, 300, 400, 500, 600, 700 and 800 N was reached, respectively. The average voltage output is calculated from three measurements.

4.4.11 Energy harvester

Four FFF printed PVDF films were connected in parallel and glued on a 3D printed PLA tree as the energy harvesting "leaves" and blowed by a tabletop air circulation fan (PFT30T2ABB-V, PELONIS) at 1500 rpm. A circuit was built in order to light a red LED using the energy generated by the "piezo leaves". In this circuit, a bridge-rectifier consisting of four diodes converted the AC generated by these four "piezo leaves" to DC, while a 2.2 μF capacitor stored the converted energy. The stored voltage in the capacitor was displayed by a digital multimeter (HHM11, Omega Engineering, Inc.).

4.5 Supporting information

4.5.1 In-house-designed contact poling setup

Figure 4.6 shows the contact poling setup which consisted of three parts: an in-house-designed contact poling setup, a high voltage power supply (max voltage = 60 kV) and a hot plate. In the poling station, the positive high voltage cable from the high voltage power supply was connected to a copper rod with a diameter of 3 mm as the top electrode, and an aluminum plate was grounded as the bottom electrode. A ceramic-insulated resistance temperature detector (956-35110016, Mouser Electronics, Inc.) was mounted on the aluminum plate and connected to the hot plate to control the temperature of the silicone oil bath.

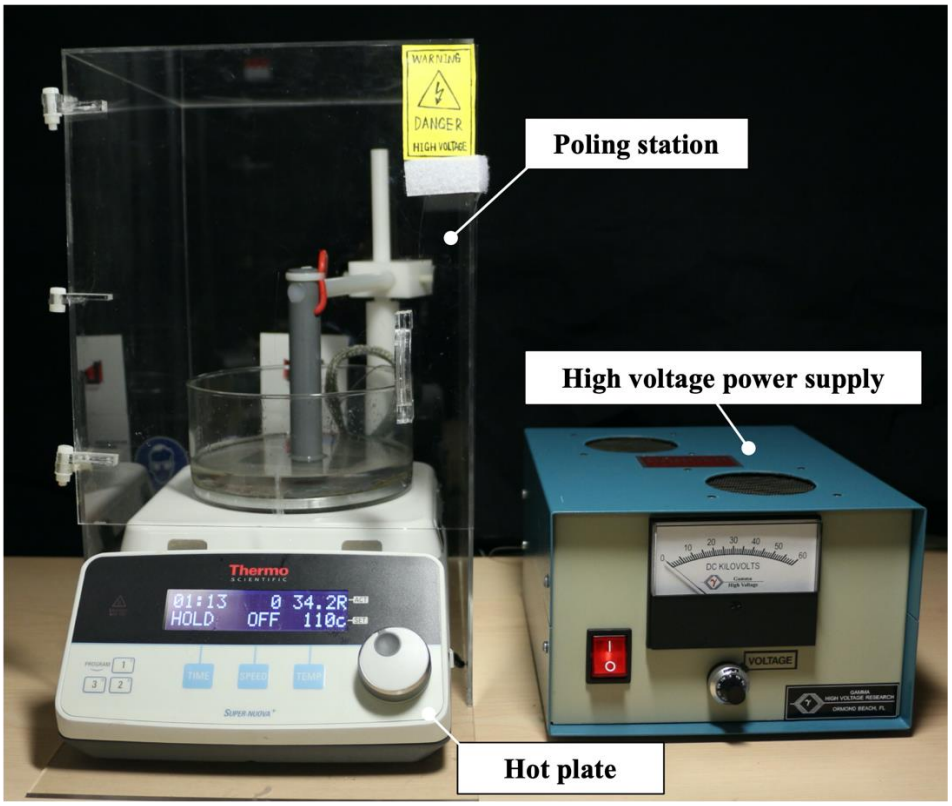

Figure 4.6 Photo of an in-house-designed contact poling station: a poling head (-), a silicone oil bath and an aluminum plate (+) (left) and a high voltage power supply (right).

4.5.2 Surface characterization of the fabricated PVDF films

Defect-free printed PVDF films are important for the post-processing, i.e. stretching and poling processes. Figure 4.7 shows the optical images of the well-printed (Figure 4.7a) and the printed PVDF films with defects (Figure 4.7b). As shown in Figure 4.7b, thinner section between the printed lines and the defects not only result in the failure during the stretching process but also limit the amplitude of the poling electric field during the poling process. In order to achieve a good printing without the thinner section between the printed lines, the printing bed should be well leveled and the extrusion width is decreased from 0.48 mm to 0.40 mm.

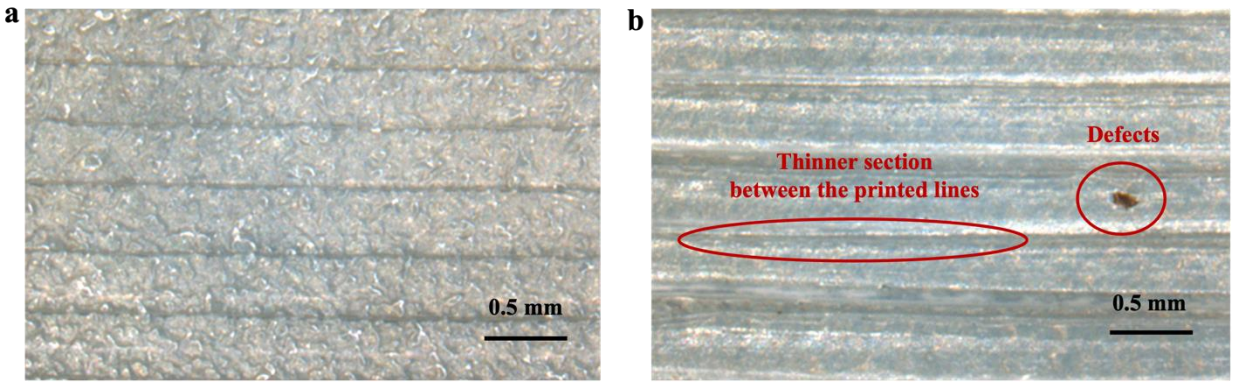

Figure 4.7 Optical images of the top surface of (a) the well-printed PVDF film, and (b) the printed PVDF film with defects.

4.5.3 Photo and thickness of the printed PVDF films with different *R*

Figure 4.8 shows the photo of the stretched PVDF films at R = 1, 2, 3 and 4. The thickness of the films were measured using a digital micrometer. The average thickness of the films and the poling voltage (i.e. electric field 30 V/μm) are listed in Table 4.2. Before the poling process, all types of PVDF films are cut into 40 × 20 mm from the center of the printed or stretched PVDF films.

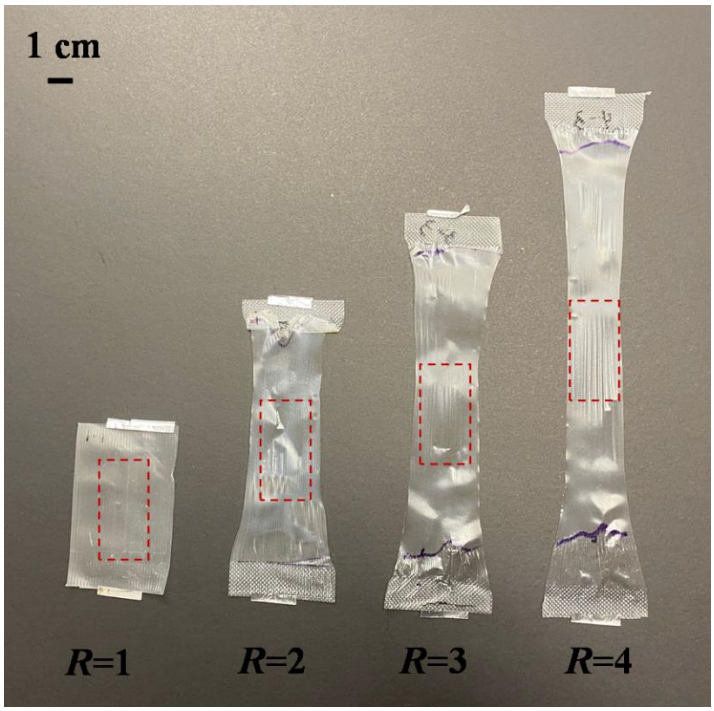

Figure 4.8 Photos of the stretched PVDF films at R=1, 2, 3 and 4.

Table 4.2 Thickness of the stretched PVDF films.

R	Average thickness (μm)	Poling voltage (kV)
1	150	4.5
2	120	3.6
3	90	2.7
4	60	1.8

4.5.4 Maximum operating temperature for the printed polarized PVDF films

To investigate the maximum working temperature of the piezoelectric PVDF films (R = 4; poling electric field = 30 V/μm) fabricated in this work, the polarized printed PVDF films were heated in the silicone oil bath at 30, 40, 50, 60, 70, 80, 90 and 100°C for 1 hr, respectively, and the piezoelectric coefficient (d_{33}) were measured by the d_{33} meter at three different locations before and after being heated (Figure 4.9). We find that the PVDF films start to lose its piezoelectric performance gradually when the temperature is above 60°C, which is consistent with the reported maximum operating temperature of commercial PVDF piezo sensors.[53] The reason is that the higher mobility of PVDF molecules at an elevated temperature results in the misalignment of the dipole moments. As a consequence, during the poling process, we need to cool down the piezo elements below 60°C before removing the poling electric field in order to avoid the misalignment of the dipole moments.

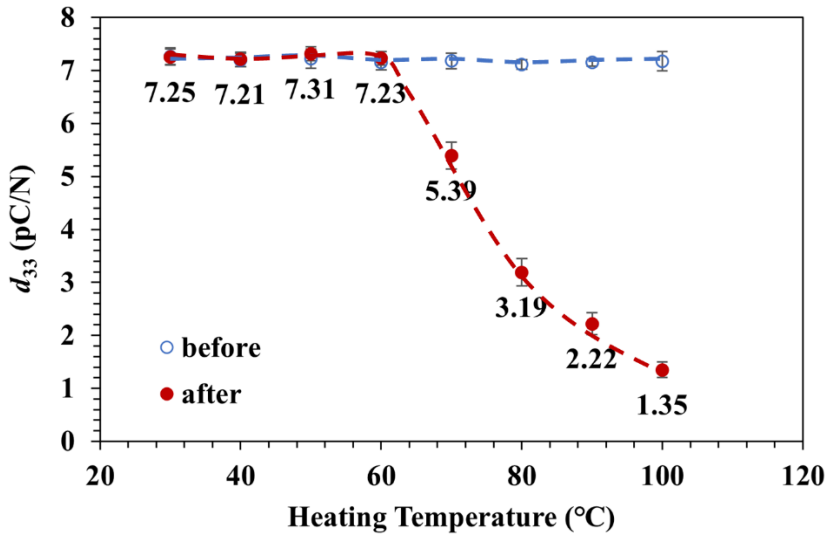

Figure 4.9 Piezoelectric coefficient d_{33} of printed polarized PVDF films before and after being heated at 30, 40, 50, 60, 70, 80, 90, and 100°C for 1 hr. Error bars indicate the standard deviations obtained from three location measurements on three different samples.

4.5.5 Optimal voltage output and power output of the "piezo leaves" energy harvesters with the external resistance

The effects of external resistance load on the voltage output of the "piezo leaves" are shown in Figure 4.10a. It can be observed that the voltage output increases with the external resistance. Figure 4.10b shows the instantaneous output power (P) at different external resistances (1 kΩ, 10 kΩ, 100 kΩ, 1 MΩ and 10 MΩ) calculated by:

$$P = \frac{U^2}{r} \tag{4-2}$$

where U is the output voltage and r is the external resistance as shown in Figure 4.10a. The maximum power output of the "piezo leaves" is ~ 0.45 μW when the optimum resistance is 1 MΩ. The instantaneous power density with the optimum resistance is calculated by:

$$S = \frac{P}{V} \tag{4-3}$$

where S is the power density and V is the volume of the four "piezo leaves". The calculated S of the four "piezo leaves" is ~ 9.38 μWcm^{-3} at a resistance of 1 MΩ.

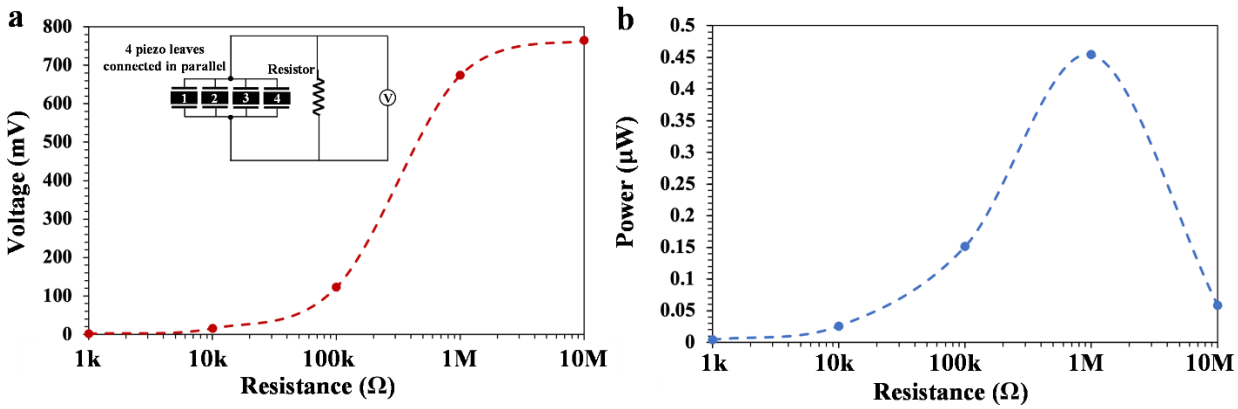

Figure 4.10 (a) Output voltage, (Inset: circuit diagram of the energy harvesting behavior test.) (b) Power of the "piezo leaves" with different resistances (1 kΩ, 10 kΩ, 100 kΩ, 1 MΩ and 10 MΩ) when the fan is turned on (1500 rpm).

Acknowledgement

We acknowledge support from National Science and Engineering Research Council (NSERC), Discovery program (#RGPIN-4566-2018) and the Department of National Defence (DND) (Grant#: DGDND-2018-00011). Ms. Rui Tao and Mr. Jiahao Shi acknowledge the financial support that they have received from the China Scholarship Council (CSC). We are thankful for the instrument and the lab access kindly provided by Prof. Frédérick Gosselin, Prof. Stéphane Étienne, Prof. Annie Ross, and Prof. Abdellah Ajji at Polytechnique Montreal. We would like to especially thank technicians Mr. Yanik Landry-Ducharme, Mr. Bénédict Besner, Mr. Nour Aimene, Mr. Robert Delisle, and research associates Mr. Matthieu Gauthier and Mr. Richard Silverwood for the technical support, as well as Dr. Rouhollah Farahani, Dr. Kambiz Chizari and Dr. Shibo Zou for their technical advice.

References

(1) Wang, Z.; Yuan, X.; Yang, J.; Huan, Y.; Gao, X.; Li, Z.; Wang, H.; Dong, S. 3D-Printed Flexible, Ag-Coated PNN-PZT Ceramic-Polymer Grid-Composite for Electromechanical Energy Conversion. *Nano Energy* **2020**, *73* (March), 104737.

(2) Bodkhe, S.; Turcot, G.; Gosselin, F. P.; Therriault, D. One-Step Solvent Evaporation-Assisted 3D Printing of Piezoelectric PVDF Nanocomposite Structures. *ACS Appl. Mater. Interfaces* **2017**, *9* (24), 20833–20842.

(3) Lu, X.; Qu, H.; Skorobogatiy, M. Piezoelectric Micro- and Nanostructured Fibers Fabricated from Thermoplastic Nanocomposites Using a Fiber Drawing Technique: Comparative Study and Potential Applications. *ACS Nano* **2017**, *11* (2), 2103–2114.

(4) Huo, Z.; Wang, X.; Zhang, Y.; Wan, B.; Wu, W.; Xi, J.; Yang, Z.; Hu, G.; Li, X.; Pan, C. High-Performance Sb-Doped p-ZnO NW Films for Self-Powered Piezoelectric Strain Sensors. *Nano Energy* **2020**, *73* (February), 104744.

(5) Wang, X.; He, X.; Zhu, H.; Sun, L.; Fu, W.; Wang, X.; Hoong, L. C.; Wang, H.; Zeng, Q.; Zhao, W.; Wei, J.; Jin, Z.; Shen, Z.; Liu, J.; Zhang, T.; Liu, Z. Subatomic Deformation Driven by Vertical Piezoelectricity from CdS Ultrathin Films. *Sci. Adv.* **2016**, *2* (7), 1–10.

(6) Wu, Y.; Yim, J. K.; Liang, J.; Shao, Z.; Qi, M.; Zhong, J.; Luo, Z.; Yan, X.; Zhang, M.; Wang, X.; Fearing, R. S.; Full, R. J.; Lin, L. Insect-Scale Fast Moving and Ultrarobust Soft Robot. *Sci. Robot.* **2019**, *4* (32).

(7) Li, N.; Yi, Z.; Ma, Y.; Xie, F.; Huang, Y.; Tian, Y.; Dong, X.; Liu, Y.; Shao, X.; Li, Y.; Jin, L.; Liu, J.; Xu, Z.; Yang, B.; Zhang, H. Direct Powering a Real Cardiac Pacemaker by Natural Energy of a Heartbeat. *ACS Nano* **2019**, *13* (3), 2822–2830.

(8) Zhang, Y.; Bowen, C. R.; Ghosh, S. K.; Mandal, D.; Khanbareh, H.; Arafa, M.; Wan, C. Ferroelectret Materials and Devices for Energy Harvesting Applications. *Nano Energy* **2019**, *57*, 118–140.

(9) Shi, J.; Akbarzadeh, A. H. Architected Cellular Piezoelectric Metamaterials: Thermo-Electro-Mechanical Properties. *Acta Mater.* **2019**, *163*, 91–121.

(10) Shi, J.; Akbarzadeh, A. H. 3D Hierarchical Lattice Ferroelectric Metamaterials. *Int. J. Eng. Sci.* **2020**, *149*, 103247.

(11) Kim, W.; Pyo, S.; Kim, M. O.; Oh, Y.; Kwon, D. S.; Kim, J. Humidity-Resistant Triboelectric Energy Harvester Using Electrospun PVDF/PU Nanofibers for Flexibility and Air Permeability. *Nanotechnology* **2019**, *30* (27).

(12) Fiorillo, A. S.; Pullano, S. A.; Bianco, M. G.; Critello, C. D. Bioinspired US Sensor for Broadband Applications. *Sensors Actuators, A Phys.* **2019**, *294*, 148–153.

(13) Ghafari, E.; Jiang, X.; Lu, N. Surface Morphology and Beta-Phase Formation of Single Polyvinylidene Fluoride (PVDF) Composite Nanofibers. *Adv. Compos. Hybrid Mater.* **2018**, *1* (2), 332–340.

(14) Sarkar, S.; Garain, S.; Mandal, D.; Chattopadhyay, K. K. Electro-Active Phase Formation in PVDF-BiVO4 Flexible Nanocomposite Films for High Energy Density Storage Application. *RSC Adv.* **2014**, *4* (89), 48220–48227.

(15) Kim, G. H.; Hong, S. M.; Seo, Y. Piezoelectric Properties of Poly(Vinylidene Fluoride) and Carbon Nanotube Blends: β-Phase Development. *Phys. Chem. Chem. Phys.* **2009**, *11* (44), 10506–10512.

(16) El Achaby, M.; Arrakhiz, F. Z.; Vaudreuil, S.; Essassi, E. M.; Qaiss, A. Piezoelectric β-Polymorph Formation and Properties Enhancement in Graphene Oxide - PVDF Nanocomposite Films. *Appl. Surf. Sci.* **2012**, *258* (19), 7668–7677.

(17) Soin, N.; Zhao, P.; Prashanthi, K.; Chen, J.; Ding, P.; Zhou, E.; Shah, T.; Ray, S. C.; Tsonos, C.; Thundat, T.; Siores, E.; Luo, J. High Performance Triboelectric Nanogenerators Based on Phase-Inversion Piezoelectric Membranes of Poly(Vinylidene Fluoride)-Zinc Stannate (PVDF-ZnSnO3) and Polyamide-6 (PA6). *Nano Energy* **2016**, *30* (August), 470–480.

(18) Arshad, A. N.; Wahid, M. H. M.; Rusop, M.; Majid, W. H. A.; Subban, R. H. Y.; Rozana, M. D. Dielectric and Structural Properties of Poly(Vinylidene Fluoride) (PVDF) and Poly(Vinylidene Fluoride-Trifluoroethylene) (PVDF-TrFE) Filled with Magnesium Oxide Nanofillers. *J. Nanomater.* **2019**, *2019*.

(19) Salimi, A.; Yousefi, A. A. FTIR Studies of β-Phase Crystal Formation in Stretched PVDF Films. *Polym. Test.* **2003**, *22* (6), 699–704.

(20) Luo, H.; Huang, Y.; Wang, D. The Crystallization and Crystal Transition of PVDF in PAN Nano-Tube. *Polymer (Guildf).* **2013**, *54* (17), 4710–4718.

(21) Gregorio, R.; Ueno, E. M. Effect of Crystalline Phase, Orientation and Temperature on the Dielectric Properties of Poly (Vinylidene Fluoride) (PVDF). *J. Mater. Sci.* **1999**, *34* (18), 4489–4500.

(22) Sencadas, V.; Moreira, V. M.; Lanceros-Mendéz, S.; Pouzada, A. S.; Gregório, R. α - To - β Transformation on PVDF Films Obtained by Uniaxial Stretch. *Mater. Sci. Forum* **2006**, *514–516* (PART 2), 872–876.

(23) Jahan, N.; Mighri, F.; Rodrigue, D.; Ajji, A. Effect of the Inflation Strategy on the Piezoelectric Response of Cellular Poly(Vinylidene Fluoride) Ferroelectret. *J. Appl. Polym. Sci.* **2019**, *136* (20), 47540.

(24) Ren, X.; Meng, N.; Zhang, H.; Wu, J.; Abrahams, I.; Yan, H.; Bilotti, E.; Reece, M. J. Giant Energy Storage Density in PVDF with Internal Stress Engineered Polar Nanostructures. *Nano Energy* **2020**, *72* (February), 104662.

(25) Huang, Z. X.; Wang, M. M.; Feng, Y. H.; Qu, J. P. β-Phase Formation of Polyvinylidene Fluoride via Hot Pressing under Cyclic Pulsating Pressure. *Macromolecules* **2020**, *53* (19), 8494–8501.

(26) Tao, H.; Wu, J. New Poling Method for Piezoelectric Ceramics. *J. Mater. Chem. C* **2017**, *5* (7), 1601–1606.

(27) Guo, H.; Ma, C.; Liu, X.; Tan, X. Electrical Poling below Coercive Field for Large Piezoelectricity. *Appl. Phys. Lett.* **2013**, *102* (9), 6–10.

(28) Granzow, T.; Kounga, A. B.; Aulbach, E.; Rödel, J. Electromechanical Poling of Piezoelectrics. *Appl. Phys. Lett.* **2006**, *88* (25).

(29) Ribeiro, C.; Correia, D. M.; Ribeiro, S.; Sencadas, V.; Botelho, G.; Lanceros-Méndez, S. Piezoelectric Poly(Vinylidene Fluoride) Microstructure and Poling State in Active Tissue Engineering. *Eng. Life Sci.* **2015**, *15* (4), 351–356.

(30) Kumar, A.; Bhanu Prasad, V. V.; James Raju, K. C.; James, A. R. Optimization of Poling Parameters of Mechanically Processed PLZT 8/60/40 Ceramics Based on Dielectric and Piezoelectric Studies. *Eur. Phys. J. B* **2015**, *88* (11).

(31) Nilsson, E.; Lund, A.; Jonasson, C.; Johansson, C.; Hagström, B. Poling and Characterization of Piezoelectric Polymer Fibers for Use in Textile Sensors. *Sensors Actuators, A Phys.* **2013**, *201*, 477–486.

(32) Porter, D. A.; Hoang, T. V. T.; Berfield, T. A. Effects of In-Situ Poling and Process Parameters on Fused Filament Fabrication Printed PVDF Sheet Mechanical and Electrical Properties. *Addit. Manuf.* **2017**, *13*, 81–92.

(33) Kim, H.; Torres, F.; Wu, Y.; Villagran, D.; Lin, Y.; Tseng, T.-L. Integrated 3D Printing and Corona Poling Process of PVDF Piezoelectric Films for Pressure Sensor Application. *Smart Mater. Struct.* **2017**, *26* (8), 085027.

(34) Cui, H.; Hensleigh, R.; Yao, D.; Maurya, D.; Kumar, P.; Kang, M. G.; Priya, S.; Zheng, X. Three-Dimensional Printing of Piezoelectric Materials with Designed Anisotropy and Directional Response. *Nat. Mater.* **2019**, *18* (3), 234–241.

(35) Kim, H.; Fernando, T.; Li, M.; Lin, Y.; Tseng, T. L. B. Fabrication and Characterization of 3D Printed BaTiO3/PVDF Nanocomposites. *J. Compos. Mater.* **2018**, *52* (2), 197–206.

(36) Lee, C.; Tarbutton, J. A. Electric Poling-Assisted Additive Manufacturing Process for Lead-Free Piezoelectric Device Fabrication. *Procedia Manuf.* **2015**, *1*, 320–326.

(37) Wei, H.; Cauchy, X.; Navas, I. O.; Abderrafai, Y.; Chizari, K.; Sundararaj, U.; Liu, Y.; Leng, J.; Therriault, D. Direct 3D Printing of Hybrid Nanofiber-Based Nanocomposites for Highly Conductive and Shape Memory Applications. *ACS Appl. Mater. Interfaces* **2019**, *11* (27), 24523–24532.

(38) Wu, Q.; Zou, S.; Gosselin, F. P.; Therriault, D.; Heuzey, M. C. 3D Printing of a Self-Healing Nanocomposite for Stretchable Sensors. *J. Mater. Chem. C* **2018**, *6* (45), 12180–12186.

(39) Zou, S.; Therriault, D.; Gosselin, F. P. Spiderweb-Inspired, Transparent, Impact-Absorbing Composite. *Cell Reports Phys. Sci.* **2020**, *1* (11), 100240.

(40) Ataur Rahman, M.; Lee, B. C.; Phan, D. T.; Chung, G. S. Fabrication and Characterization of Highly Efficient Flexible Energy Harvesters Using PVDF-Graphene Nanocomposites. *Smart Mater. Struct.* **2013**, *22* (8).

(41) Salimi, A.; Yousefi, A. A. Conformational Changes and Phase Transformation Mechanisms in PVDF Solution-Cast Films. *J. Polym. Sci. Part B Polym. Phys.* **2004**, *42* (18), 3487–3495.

(42) Brunengo, E.; Castellano, M.; Conzatti, L.; Canu, G.; Buscaglia, V.; Stagnaro, P. PVDF-Based Composites Containing PZT Particles: How Processing Affects the Final Properties. *J. Appl. Polym. Sci.* **2020**, *137* (20), 1–8.

(43) Lyu, J. Y.; Chen, S.; He, W.; Zhang, X. X.; Tang, D. yun; Liu, P. J.; Yan, Q. L. Fabrication of High-Performance Graphene Oxide Doped PVDF/CuO/Al Nanocomposites via Electrospinning. *Chem. Eng. J.* **2019**, *368* (November 2018), 129–137.

(44) Sorayani Bafqi, M. S.; Bagherzadeh, R.; Latifi, M. Fabrication of Composite PVDF-ZnO Nanofiber Mats by Electrospinning for Energy Scavenging Application with Enhanced Efficiency. *J. Polym. Res.* **2015**, *22* (7), 1–9.

(45) Lalia, B. S.; Guillen-Burrieza, E.; Arafat, H. A.; Hashaikeh, R. Fabrication and Characterization of Polyvinylidenefluoride-Co-Hexafluoropropylene (PVDF-HFP) Electrospun Membranes for Direct Contact Membrane Distillation. *J. Memb. Sci.* **2013**, *428*, 104–115.

(46) Commercial piezoelectric PVDF film. https://piezopvdf.com/piezoelectric-poled-pvdf-film-d31/.

(47) Pei, H.; Xie, Y.; Xiong, Y.; Lv, Q.; Chen, Y. A Novel Polarization-Free 3D Printing Strategy for Fabrication of Poly (Vinylidene Fluoride) Based Nanocomposite Piezoelectric Energy Harvester. *Compos. Part B Eng.* **2021**, *225* (July), 109312.

(48) Liu, X.; Shang, Y.; Zhang, J.; Zhang, C. Ionic Liquid-Assisted 3D Printing of Self-Polarized β-PVDF for Flexible Piezoelectric Energy Harvesting. *ACS Appl. Mater. Interfaces* **2021**, *13* (12), 14334–14341.

(49) Ducrot, P. H.; Dufour, I.; Ayela, C. Optimization of PVDF-TrFE Processing Conditions for the Fabrication of Organic MEMS Resonators. *Sci. Rep.* **2016**, *6* (January), 1–7.

(50) Jaleh, B.; Jabbari, A. Evaluation of Reduced Graphene Oxide/ZnO Effect on Properties of PVDF Nanocomposite Films. *Appl. Surf. Sci.* **2014**, *320*, 339–347.

(51) John X. J. Zhang and Kazunori Hosshino. *Molecular Sensors and Nanodevices*; 2014.

(52) Building a Piezoelectric Generator. Https://Www.Teachengineering.Org/Activities/View/Uoh_piezo_lesson01_activity1.

(53) Fu, J.; Hou, Y.; Gao, X.; Zheng, M.; Zhu, M. Highly Durable Piezoelectric Energy Harvester Based on a PVDF Flexible Nanocomposite Filled with Oriented BaTi2O5 Nanorods with High Power Density. *Nano Energy* **2018**, *52* (August), 391–401.

(54) Karan, S. K.; Bera, R.; Paria, S.; Das, A. K.; Maiti, S.; Maitra, A.; Khatua, B. B. An Approach to Design Highly Durable Piezoelectric Nanogenerator Based on Self-Poled PVDF/AlO-RGO Flexible Nanocomposite with High Power Density and Energy Conversion Efficiency. *Adv. Energy Mater.* **2016**, *6* (20), 1–12.

(55) Sun, B.; Li, X.; Zhao, R.; Ji, H.; Qiu, J.; Zhang, N.; He, D.; Wang, C. Electrospun Poly(Vinylidene Fluoride)-Zinc Oxide Hierarchical Composite Fiber Membrane as Piezoelectric Acoustoelectric Nanogenerator. *J. Mater. Sci.* **2019**, *54* (3), 2754–2762.

CHAPTER 5 ARTICLE 2: MULTI-MATERIAL FUSED FILAMENT FABRICATION OF FLEXIBLE 3D PIEZOELECTRIC NANOCOMPOSITE LATTICES FOR PRESSURE SENSING AND ENERGY HARVESTING APPLICATIONS

Rui Tao[1,2], Jiahao Shi[2,3], Floriane Granier[1,2], Mohammadreza Moeini[1], Abdolhamid Akbarzadeh[2,3,4] and Daniel Therriault[1,2*]

[1] Laboratory for Multiscale Mechanics (LM^2), Department of Mechanical Engineering, Polytechnique Montreal, Montreal, QC, H3T 1J4, Canada

[2] Research Center for High Performance Polymer and Composite Systems (CREPEC), Montreal, QC, H3T 1J4, Canada

[3] Advanced Multifunctional and Multiphysics Metamaterials Laboratory (AM^{3}L), Department of Bioresource Engineering, McGill University, Montreal, QC, H9X 3V9, Canada

[4] Department of Mechanical Engineering, McGill University, Montreal, QC, H3A 0C3, Canada

Submitted in Applied Materials Today on April 19th, 2022

Abstract

Flexible three-dimensional (3D) piezoelectric sensors and energy harvesters are in great demand for wireless and low power consumption human health monitors, artificial skins and soft robots. In this work, a multi-material fused filament fabrication (FFF) 3D printing technique is used to fabricate 3D piezoelectric and flexible composite structures with integrated electrodes by utilizing a developed piezoelectric composite filament and a commercially available conductive composite filament. The developed piezoelectric composite filament consists of flexible polyurethane (TPU) matrix and 30 vol% of piezoelectric ceramic lead zirconate titanate (PZT) nanoparticle fillers. The fabricated TPU/30vol%PZT piezoelectric composite has an elongation at break strain of ~56% and a d_{33} value of 6.8 pC/N after being polarized. Four types of 3D piezoelectric composite lattices including Simple cubic, Body-centered cubic, Cuboctahedron and Octet truss (and one fully dense solid for counterpart) are fabricated and tested. Under the same maximum applied compressive force, octet truss piezoelectric composite lattice generates two times higher voltage output than the fully dense solid counterpart, aligned with our finite element analysis (FEA) predictions. As a

demonstration for the potential applications, a multi-material 3D printed flexible piezoelectric composite shoe sole made of the octet truss infill pattern can generate a high peak-to-peak voltage (V_{pp}) of ~20 V through a typical human stomp. Our approach can open a new avenue for designing and manufacturing flexible piezoelectric devices for sensing and energy harvesting applications.

5.1 Introduction

Piezoelectric materials find widespread applications in sensing,[1–3] energy harvesting[4–6] and actuating[7,8] fields owing to their capability for converting mechanical energy into electrical energy and vice versa.[9–11] The piezoelectric charge coefficient d_{ij} has two subscripts: the first subscript i indicates the direction of the charge generation, and the second subscript j indicates the direction of the applied stress.[12] Compared to the piezoelectric polymer polyvinylidene fluoride (PVDF) and its copolymers, piezoelectric ceramics such as lead zirconate titanate (PZT) and barium titanate ($BaTiO_3$) typically have ~10 times higher piezoelectric coefficient (d_{ij}) and only require a low poling electric field.[13,14] The piezoelectricity of the piezoelectric ceramic originates from the dipole moments between the tetravalent metal ion, titanium Ti^{4+} or zirconium Zr^{4+} and the diatomic oxygen ions O^{2-} when temperature is below the Curie temperature (T_c).[15] Above T_c, crystalline structure of the ceramic changes from tetragonal system (polar) to cubic system (symmetric, non-polar), thus loses its piezoelectric behavior.[16,17] Traditionally, to fabricate a piezoelectric PZT product, PZT particles are mixed with a binder (Polyvinyl alcohol (PVA)) and the resulting mixture is formed into a desired shape. The PZT parts are heat treated at high temperatures in a furnace during which the binder is removed and the piezo particles are sintered. The dense crystalline structure is then polarized according to the desired poling time, temperature and voltage parameters.[18] Although the fabricated devices possess high piezoelectric properties, this manufacturing process is delicate and time-consuming. Another disadvantage is that the fabricated piezoelectric ceramic devices are brittle in nature and susceptible to cracking during service.[19]

In order to overcome the shortcomings of the piezoelectric ceramic devices, researchers incorporated piezoelectric ceramic particles into the polymer matrix to fabricate piezoelectric composite materials. However, most of the reported fabricated piezoelectric composites are in simple fiber (1D)[20,21] or film (2D)[22,23] shapes. Additive manufacturing (AM), also referred as three-dimensional (3D) printing, is a family of several processes that enables the fabrication of a 3D

shape in a layer-by-layer approach. Several 3D printing techniques such as direct ink writing (DIW),[24–27] digital light processing (DLP)[28,29] and fused filament fabrication (FFF) have been used to fabricate 3D smart composite structures.[28–37] On account of the ready-to-use thermoplastic filament, FFF 3D printing technique is widely used without the impact of the limited shelf-life for the raw material compared to other techniques (i.e., change of material properties by time in solvent-based inks, the thermoset-based inks (DIW) or photocurable resin (DLP)). Another issue related to the piezoelectric composite materials is that most polymer matrix (e.g., PVDF[38–40]) used for developing piezoelectric composites are not stretchable. Thus, the produced piezoelectric devices cannot be conformally applied to soft and irregularly shaped surfaces for use in wearable sensors.

On the manufacturing side, an extra step is usually required to add electrodes on the top and bottom surfaces of the piezoelectric element by painting,[41] screen printing,[42] sputtering[43] or attaching conductive tape or fabrics.[44,45] The electrode layers tend to wear or rupture after a period of usage. Multi-material 3D printing technology used for the fabrication of multi-color or multifunctional composites,[27,46,47] has a great potential to co-fabricate electrodes and the piezoelectric element in a single manufacturing process.

The goal of the present work is to develop a 3D-printable, flexible and high-performance piezoelectric composite filament by incorporating piezoelectric ceramic PZT particles into a flexible thermoplastic polyurethane (TPU) matrix. We designed and fabricated four types of 3D piezoelectric composite lattices (and one fully dense solid for counterpart) using a multi-material FFF 3D printing method. The voltage output of the piezoelectric lattices under the same maximum applied force and imposed displacement are investigated. The normalized voltage of the fully dense sample and the octet truss lattice under the same maximum applied force are simulated by a finite element analysis (FEA) to compare with the experimental results. Additionally, we evaluated the sensing and energy harvesting performance of a multi-material piezoelectric composite shoe sole consisting of periodic octet truss.

5.2 Results and discussion

The scanning electron microscopy (SEM) images of the transverse cross-section and the outer surface of the developed TPU/30vol% PZT filament are shown in Figure 5.1a. The absence of any significant polymer-rich regions and agglomerations in Figure 5.1a(I-II) confirm the homogeneous distribution of the PZT particles within the TPU matrix. The diameter of the filament is also relatively uniform ($1.74 \pm 0.7\%$) as shown in Figure 5.1a(III). Figure 5.1b shows the SEM image of the strong bonding between the electrode and the piezoelectric layers of the multi-material 3D printed piezoelectric devices after being bent a few times. Figure 5.1c shows 3D models of four types of 3D piezoelectric composite lattices designed for the current investigation: SC, BCC, CH and OT, respectively. Figure 5.1d shows the images and the close-up front and top views of the multi-material 3D printed piezoelectric composite lattices presented in Figure 5.1e. The manufacturing defects are mainly due to the imperfections of the extruded piezoelectric composite filaments from the twin-screw micro-compounder (e.g., surface roughness and diameter variation) and the difficulties in 3D printing stretchable filaments (e.g., filaments buckle between the feeding screws and the nozzle of the FFF 3D printer; the shear force between the two feeding screws are hard to control). In Figure 5.8 and Table 5.3 (Section S3, Supporting Information), we observed that the dimension of the 3D printed piezoelectric composite lattices well matches the as-designed samples with a maximum error of 7%, demonstrating the 3D printability of the developed piezoelectric composite filament and the feasibility of the multi-material 3D printing technique used for the fabrication of piezoelectric devices. The weight of the 3D printed lattices is also listed in Table 5.4 (Section S4, Supporting Information).

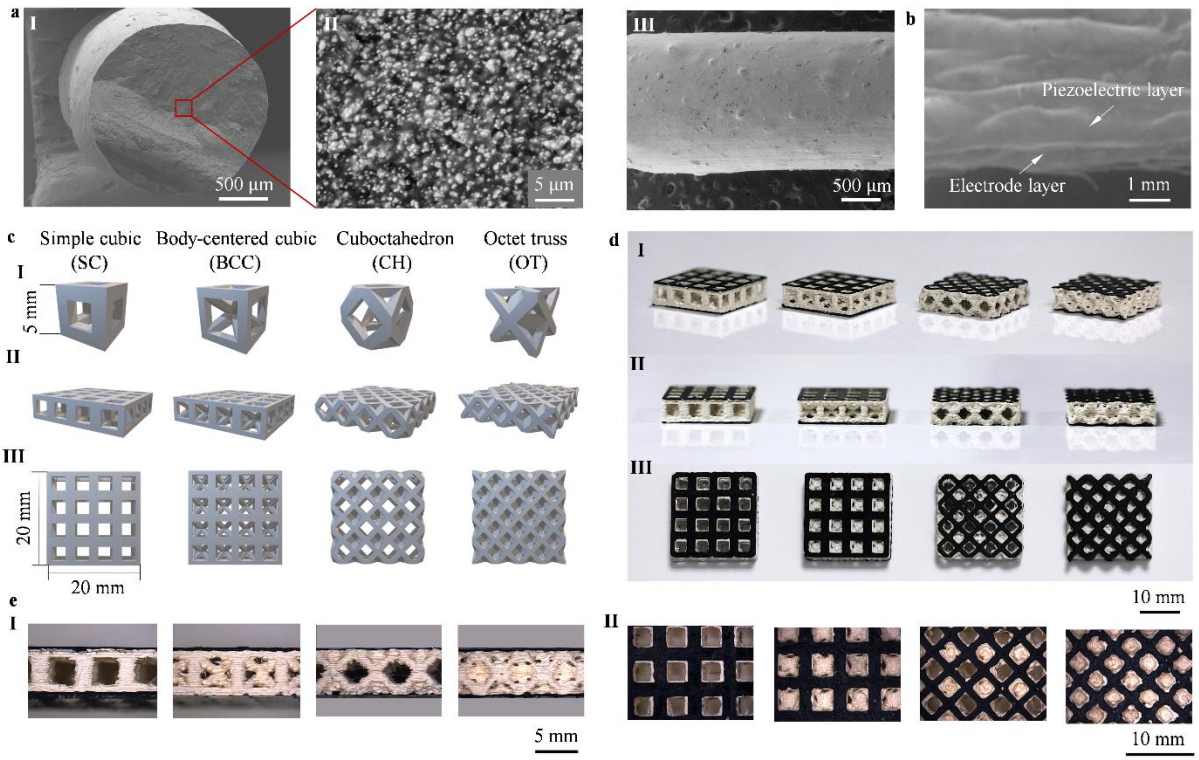

Figure 5.1 Characterization of the developed piezoelectric composite filament and the multi-material 3D printed flexible piezoelectric composite lattices with integrated electrodes: (a) SEM (I-II) cross-section and (III) surface images of piezoelectric composite filaments extruded by a twin-screw micro-compounder. (b) SEM images of bonding between the electrode and piezoelectric layers of the multi-material 3D printed sample. (c) 3D models of multi-material piezoelectric composite lattices investigated (I: one unit cell; II: isometric view; and III: top view) and (d) Images (I: isometric view; II: front view; and III: top view) of multi-material 3D printed piezoelectric composite lattices investigated. (e) Close-up views (I: front view and II: top view) of multi-material 3D printed piezoelectric composite lattices.

The main poling parameters were investigated to tailor the piezoelectric performance of the polarized 3D piezoelectric composite lattices. Figure 5.2a-c show the variation of d_{33} of the 3D printed TPU/30vol%PZT piezoelectric composite films (10 × 10 ×1 mm; 5 layers) with respect to poling electric field, time and temperature, respectively. In Figure 5.2a, the d_{33} values of the TPU/30vol%PZT piezoelectric composite films increase rapidly and then reach a plateau value with the increase of the poling electric field while the poling temperature and poling time are remained unchanged (poling temperature = 80°C and poling time = 60 min). Under the poling

electric field of 5 kV/mm, the d_{33} value of 5.52 pC/N is reached. Above 5 kV/mm, d_{33} does not significantly increase because of the complete alignment of the piezoelectric domains. In Figure 5.2b, the d_{33} values increase with poling temperature until ~80°C while the poling electric field and poling time are remained unchanged (poling electric field = 5 kV/mm and poling time = 60 min). Below 80°C, the PZT crystals could not be reoriented efficiently along with the electric field. However, when the poling temperature is above 140°C, the electrical breakdown happens (as marked in red "x"). In Figure 5.2c, the d_{33} values increase with poling time until 60 min while the poling temperature and poling electric field are remained unchanged (poling temperature = 80°C, poling electric field = 5 kV/mm). The d_{33} is almost constant for poling time beyond 60 min probably due to the complete polarization. Based on these results, the poling parameters selected in this work are 80°C, 5 kV/mm and 60 min. Figure 5.2d shows the piezoelectric performance of the TPU/PZT composites for different PZT contents (15 to 35 vol%). We observed that the d_{33} values increase from 1.45 to 6.10 pC/N with the augmentation of the PZT loading whereas the viscosity of the melted filament during the 3D printing process also increases significantly. The TPU/35vol%PZT piezoelectric composite has the highest d_{33}, but it frequently blocks the 3D printer nozzle (nozzle size = 0.6 mm). Hence, TPU/30vol% PZT composite is selected to fabricate the 3D piezoelectric composite structures in this work. As shown in Figure 5.9 (Section S5, Supporting Information), we also investigated the effect of the thickness of the piezoelectric films on the value of d_{33}. We 3D printed and polarized TPU/30vol%PZT piezoelectric composite films with different thicknesses (10 × 10 mm, thickness = 1, 2, 3, 4 and 5 mm, three replicates for each thickness type). We found that when the poling voltage is higher than 15 kV, there was a combination of contact and corona poling effect. In the contact poling process, a sufficiently high electric field is applied directly on the top and bottom electrodes of the piezoelectric materials, while corona poling is to create an electric field by depositing ionized charges on the top surface of the poled sample.[49] Therefore, the d_{33} value of the 3D printed piezoelectric composite lattices is 6.80 pC/N (thickness = 5 mm) instead of 5.52 pC/N (thickness = 1 mm). To observe the thermal stability of the polarized piezoelectric devices, we heated the polarized TPU/30vol%PZT piezoelectric composite films (10 × 10 × 1 mm, three replicates for each heating condition) at 30, 40, 50, 60, 70, 80, 90 and 100°C, respectively. As shown in Figure 5.10 (Section S6, Supporting Information), below 80°C, the d_{33} values are stable, but above 80°C, the d_{33} values decrease by increasing temperature due to the

misalignment of the piezoelectric domains. Thus, the maximum allowable operating temperature for the 3D printed piezoelectric composites developed in this work is 80°C.

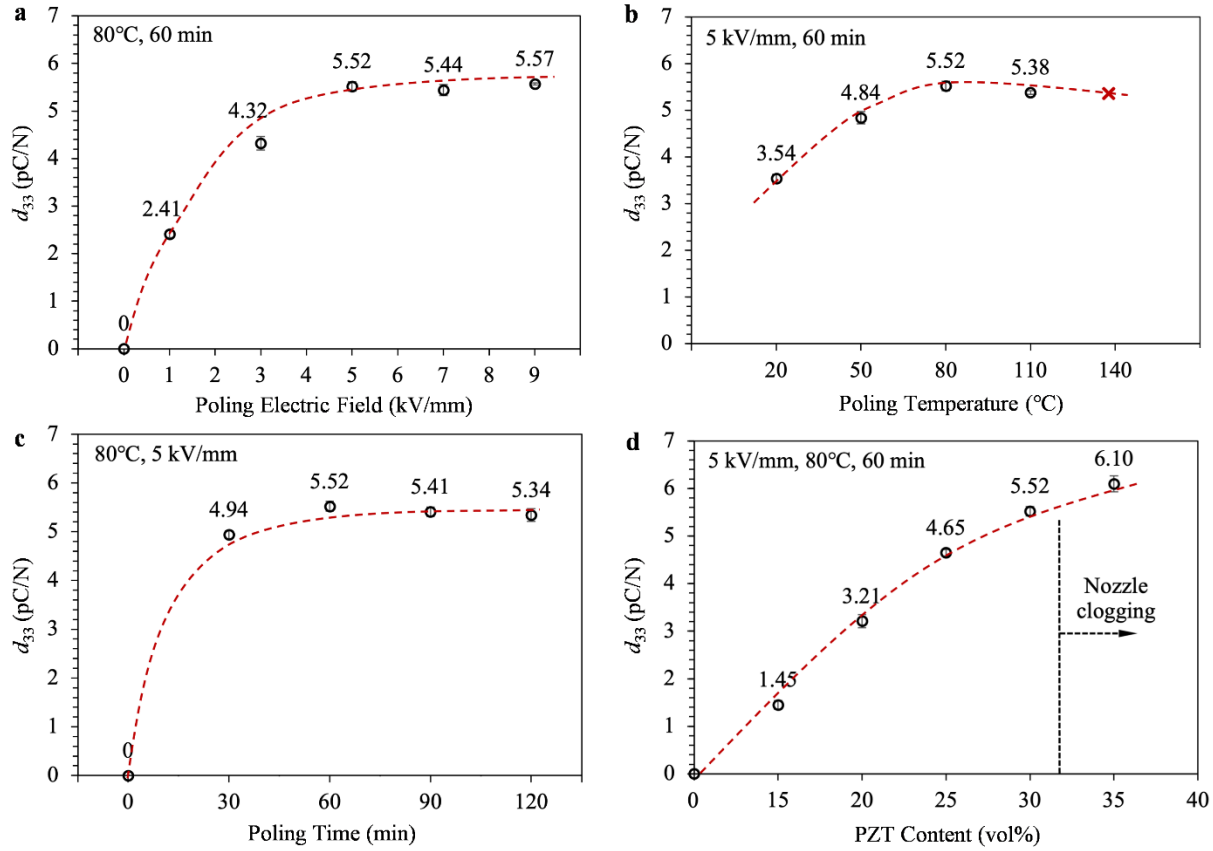

Figure 5.2 Tailoring of the poling parameters (poling electric field, temperature and time) and the PZT content in the TPU/PZT composite filament: d_{33} of TPU/30vol%PZT piezoelectric composite as a function of (a) Different poling electric fields at 80°C for 60 min, (b) Different poling temperature at 5 kV/mm for 60 min, (c) Different poling time at 80°C under an electric field of 5 kV/mm and (d) d_{33} of piezoelectric composite for different PZT volume fractions. Error bars indicate 95% confidence interval of the mean obtained from three location measurements on three different replicates.

Next step is to confirm that the TPU/30vol%PZT composite formulation shows the best compromise between being highly piezoelectric while remaining 3D printable and mechanically flexible. We investigated the mechanical behaviors of the 3D printed specimens of the pure TPU, the commercially available conductive composite and the developed piezoelectric

TPU/30vol%PZT composite. Figure 5.3a shows the optical images of the 3D printed tensile dogbone samples. The representative optical images of the side view and SEM transverse cross-section and surface images of the tensile dogbone samples are shown in Figure 5.3b(I-III). The layer height and extrusion width of these specimens are relatively uniform, and there is no delamination between the 3D printed layers. Figure 5.3c presents the average tensile stress−strain curves. The Young's modulus and the elongation at break (%) are shown in Figure 5.3d. The pure TPU used as the matrix of the conductive and piezoelectric composite exhibits the highest elongation at break (622.4% ± 27.29%) and the lowest Young's modulus (11.9 ± 0.6 MPa) compared to the conductive TPU/carbon black (128.2% ± 10.98%; 28.6 ± 0.46 MPa) and the piezoelectric TPU/30vol%PZT composites (56.3% ± 9.61%; 22.1 ± 1.27 MPa). The addition of the particles in the TPU matrix leads to the increase of the Young's modulus and the decrease of elongation at break (%) for both conductive and piezoelectric composites. The elongation at beak strain of the TPU/30vol%PZT composite is ~56%, showing its great potential to be fabricated into flexible or stretchable piezoelectric composite devices.

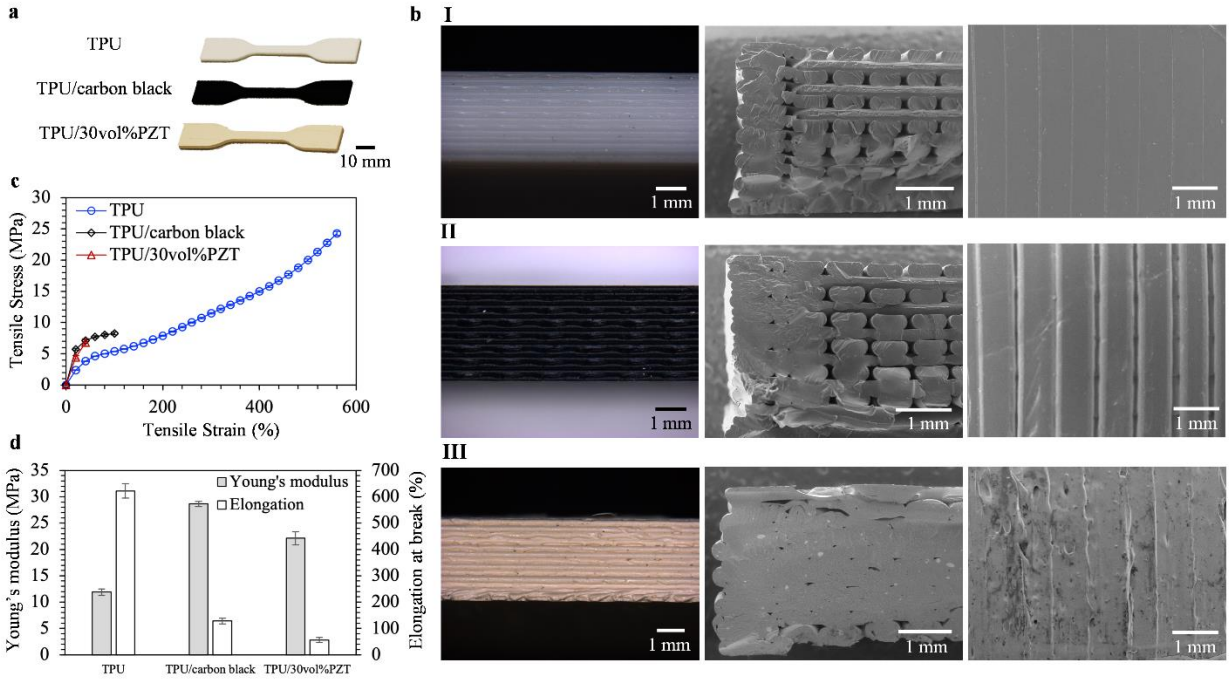

Figure 5.3 Mechanical characterization of the pure TPU, commercial TPU/carbon black conductive composite and the developed TPU/30vol%PZT piezoelectric composite: (a) A representative optical image of the printed tensile dogbone samples (printing orientation: 0°/90°). (b) Optical

images, SEM transverse cross-section and surface images of the tensile dogbone samples 3D printed out of (I) pure TPU, (II) commercial TPU/carbon black conductive composite and (III) TPU/30vol%PZT piezoelectric composite, respectively. (c) Average tensile stress-strain curves from five tested replicates. (d) Young's modulus and elongation at break (%) of the 3D printed tensile dogbone samples.

To compare the piezoelectric performance of the FD sample and four other types of lattices designed in this work, we conducted compression tests under two conditions: (1) under the same maximum applied force of 300 N and (2) under the same maximum imposed displacement of 2 mm. Figure 5.4a shows representative output voltage curves as a function of time under the same maximum force cycle, and Movie S1 (Supporting Information) shows the corresponding curves under the same imposed displacement testing conditions. The peak-to-peak voltage (V_{pp}) generated from the lattices along with the maximum displacement of the compressive head under the same peak compression force of 300 N are compared in Figure 5.4b. The four types of multi-material 3D printed piezoelectric composite lattices investigated generate higher voltage output compared to the FD sample. The OT piezoelectric composite lattice shows the highest V_{pp} of 0.273 V, almost twice the value of the FD sample (0.140 V). Figure 5.4c presents V_{pp} and peak compression force under the same imposed displacement of 2 mm. The OT lattice has also the highest voltage output among the four types of piezoelectric composite lattices under the same maximum imposed displacement of 2 mm. When we divide V_{pp} by weight for FD sample and OT lattice, the FD sample is 376 mV/g, and the OT lattice is 306 mV/g, demonstrating that OT is still showing much better results under the displacement control condition. The FD sample (5.94g) is not efficient due to the heavier weight compared to OT lattice (4.3g).

The normalized voltage distribution in the FD sample and OT piezoelectric composite lattice are simulated in ANSYS APDL. Figure 5.4d shows the normalized voltage distribution in the FD sample and the OT lattice. As presented in Figure 5.4e, the normalized peak voltage of the FD sample is 0.32 and the OT is 1. By comparing the experimental and simulation results, we observed that the ratio of the V_{pp} between the OT lattice and the FD sample is ~ 2 for the experimental results and ~ 3 for the simulation. The difference of the V_{pp} between the prediction from the model and the measured performance of the OT lattice and the FD sample probably stems from the following three reasons: (1) 3D printing defects; (2) measurement errors for the material properties used in

the simulation; (3) the electrodes are not simulated in the FEA, while in the experiment, the electrodes are stiffer than the piezoelectric composite material, and the thickness of the electrodes are not negligible compared to the thickness of the whole piezoelectric composite lattices.

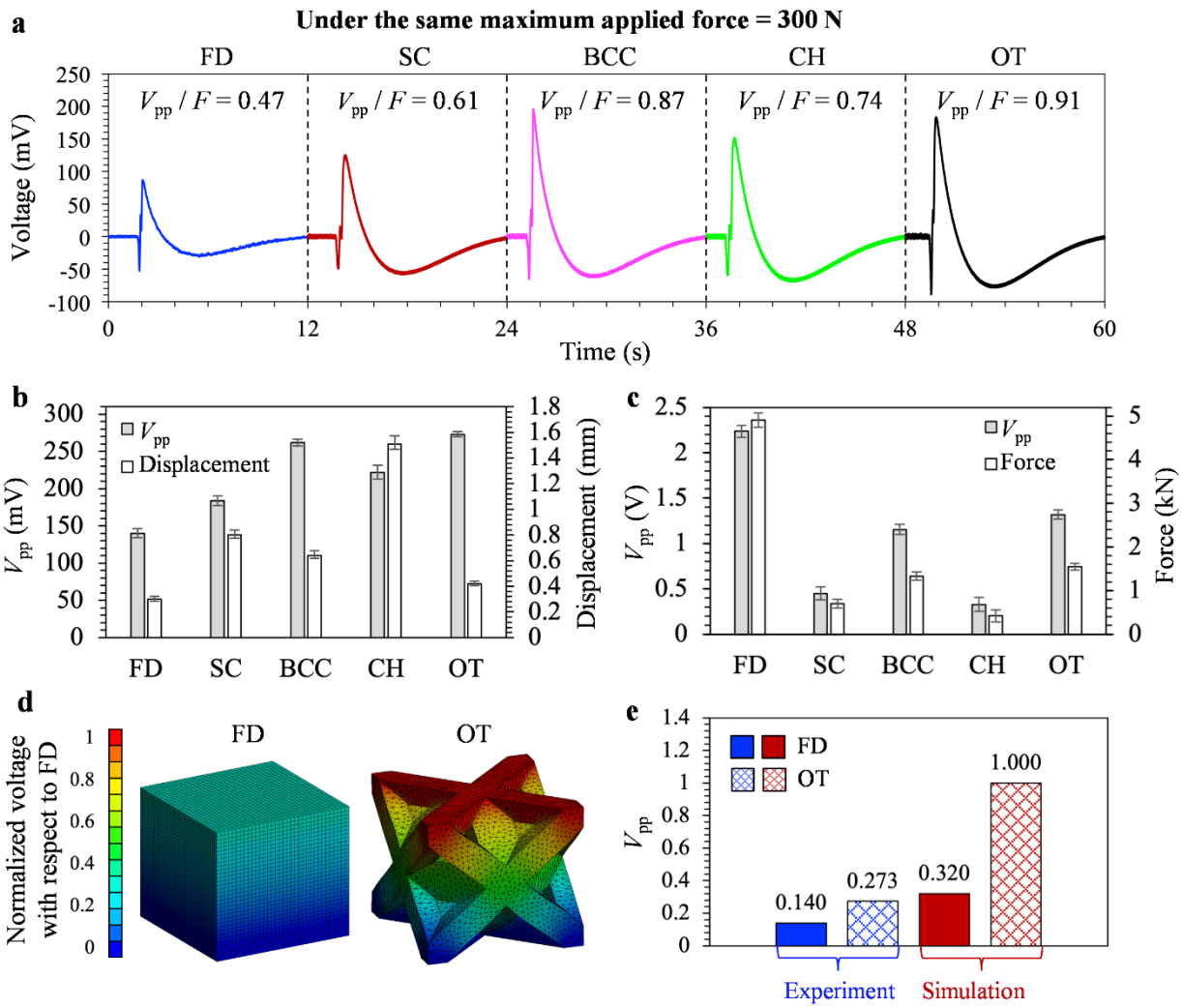

Figure 5.4 Piezoelectric characterization of the multi-material 3D printed piezoelectric composite lattices: (a) Voltage curves of the FD sample and four other types of 3D piezoelectric composite lattices under the same maximum applied force of 300 N. (b) V_{pp} of the lattices and displacement of the compressive head under the same maximum applied force of 300 N. (c) V_{pp} of the lattices and peak compressive force under the same maximum imposed displacement of 2 mm. (d) Simulation results show the normalized voltage distribution in the FD sample and OT lattice (one unit cell). (e) Comparison of the experimental and simulation results for V_{pp} found in FD sample

and OT lattice. Error bars indicate 95% confidence interval of the mean obtained from three tested replicates.

To demonstrate the piezoelectric performance of the OT lattice, a multi-material OT piezoelectric composite shoe sole was designed and fabricated. The shoe sole size is Woman US 7. Figure 5.5a shows the front view (I) and side view (II) images of the fabricated multi-material OT piezoelectric composite shoe sole. To validate the durability of the shoe sole, we conducted the cyclic compression test on the shoe sole at the human walking frequency of 2 Hz. The test setup is shown in Figure 5.5b, in which a 3D printed PLA foot replica clamped on the upper compressive head compressed the shoe sole with a displacement of 2 mm (F ~ 600 N, to simulate a 60 kg human walking condition); the pressure distribution on the piezoelectric shoe sole was recorded simultaneously by a commercial pressure map placed on the top of the multi-material OT piezoelectric composite shoe sole. The measured V_{pp} is 313 $\pm$ 0.37 mV, which indicates that the piezoelectric composite shoe sole demonstrates a favorable stability for more than 200 cycles (Figure 5.5c and 5.5d). In addition, we investigated the energy harvesting behavior by conducting a human stomp test. By one stomp, ~20 V voltage was generated from the multi-material OT piezoelectric composite shoe sole. As shown in Figure 5.5e inset, a white LED blinks by stomping on the piezoelectric composite shoe sole. The effects of external resistance load on the voltage output and generated power of the multi-material OT piezoelectric composite shoe sole are shown in Figure 5.5f. The measured voltage output increases with the resistance of the external resistors (1, 10, 20, 30, 40 and 50 MΩ). The instantaneous output power (P) at different external resistances is calculated by:

$$P = \frac{V^2}{r} \tag{5-1}$$

where V is the output voltage and r is the external resistance. The maximum power output of the multi-material OT piezoelectric composite shoe sole is ~ 28.8 μW when using an external resistance of 20 MΩ by one stomp. The energy harvesting behavior test results demonstrate the high piezoelectric performance of our multi-material 3D printed piezoelectric composite lattices and their great potential to be used in the energy harvesting field. In Movie S2 (Supporting Information), the human stomp test and cyclic compression test on the multi-material OT piezoelectric composite shoe sole are shown.

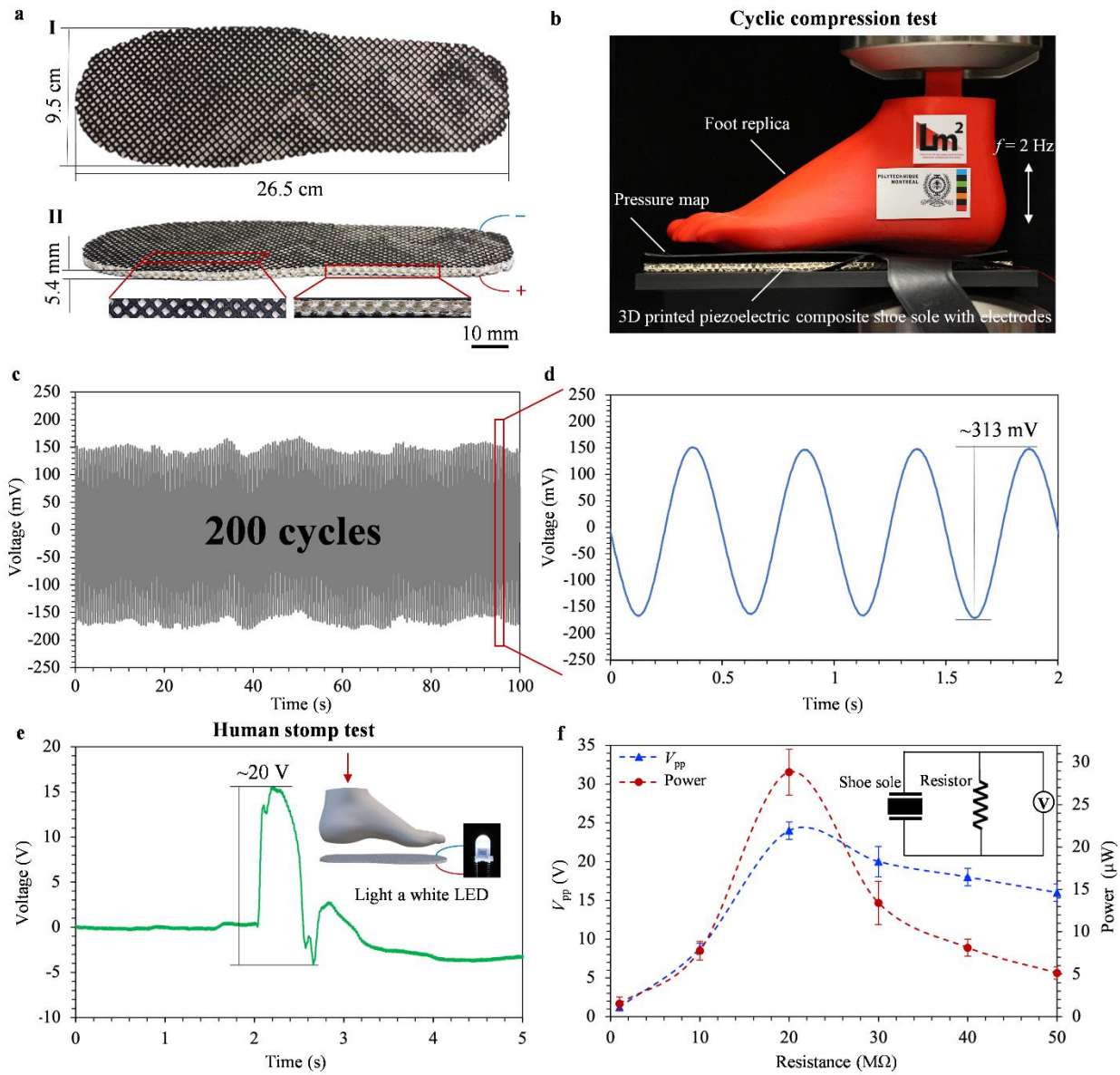

Figure 5.5 Piezoelectric characterization of the multi-material octet tress (OT) piezoelectric composite shoe sole: (a) I: top view and II: front view and enlarged views of the multi-material OT piezoelectric composite shoe sole. (b) Image of the cyclic compression test setup: a 3D printed foot replica is clamped on the upper compressive head, the multi-material OT piezoelectric composite shoe sole is placed on the bottom plate and a pressure map is placed between the foot replica and the multi-material OT piezoelectric composite shoe sole to capture the pressure distribution during the cyclic compression test. (c) Piezoelectric voltage output of the multi-material OT piezoelectric composite shoe sole at a frequency of 2 Hz for 200 cycles and (d) for 4 cycles. (e) Human stomp

test (Inset: a white LED blinks at every stomp of foot). (f) V_{pp} and power of the multi-material OT piezoelectric composite shoe sole by one stomp for different resistances (Inset: circuit diagram of the energy harvesting behavior test).

5.3 Conclusion

The multi-material 3D printed flexible piezoelectric composite lattices with integrated electrodes developed in this work show higher piezoelectric performance compared to the fully dense counterpart under the same maximum applied force, broadening the possibilities of manufacturing lightweight, high voltage output and flexible 3D piezoelectric devices. Among the investigated configurations, the multi-material octet truss piezoelectric composite lattice generates twice as much voltage as the fully dense counterpart under the same maximum compressive force cycle. The prediction from the model is a little off most probably due to the manufacturing defects. The printing quality can be further improved by both precisely controlling the diameter uniformity of the extruded filament during the filament manufacturing process and enhancing the capability of the commercial FFF 3D printers to print flexible materials (e.g., adding force sensor on the feeding screws to control the clamping force; adding proper heat-resistant guide tubes from the feeding screws to the nozzle to avoid the buckling of the flexible filament). A 3D printed flexible multi-material OT piezoelectric composite shoe sole demonstrator could generate ~ 20 V by one human stomp, showing a stable performance during a 200 cycles compression test. The topology lattice architecture can also be optimized to find lightweight designs with a potentially higher piezoelectric performance. Finally, the developed piezoelectric composite filament in this work shows a great potential to replace the commonly-used brittle and much harder to print piezoelectric ceramic materials. The multi-material 3D printing technique will be employed to fabricate wearable and flexible piezoelectric sensors or energy harvesters such as smart artificial skins and battery-free wireless energy harvesters.

5.4 Experimental section

5.4.1 Materials

PZT powder (~500 nm, sphere, APC 850) was purchased from APC International, Ltd (USA). The flexible TPU filament (1.75 mm in diameter, NinjaFlex™) was purchased from NinjaTek (USA)

as the matrix of the piezoelectric composite filament. The conductive TPU/carbon black composite filament (1.75 mm in diameter, 1,500 ohms-cm, Eel™) was also purchased from NinjaTek (USA).

5.4.2 Manufacturing process

Piezoelectric composite filament fabrication process

The commercially available TPU filament was cut into small pellets with a length of ~5 mm using a filament pelletizer machine (BT 25, Scheer Bay Co.). Both the TPU pellets and PZT powder were dried at least one day at 60°C in a vacuum oven before the composite filament extrusion process. As shown in Figure 5.6a, 30 vol% PZT powder (as fillers) and TPU pellets (as matrix) are melt-extruded in the form of a piezoelectric composite filament (~1.75 mm in diameter) using a 5 cc twin-screw micro-compounder (DSM Xplore) at 220°C with a mixing speed of 50 rpm for 10 min. Figure 5.7 (Section S1, Supporting Information) describes the recyclability of the developed piezoelectric composite material. The scrap materials or the printed parts can be re-extruded to form filaments.

FFF 3D printing of piezoelectric multi-material composite structures

A fully dense sample (FD), four types of 3D piezoelectric composite lattices[9] i.e. Simple cubic (SC), Body-centered cubic (BCC), Cuboctahedron (CH) and Octet truss (OT), and a piezoelectric shoe sole (infill pattern: OT) were fabricated using the developed piezoelectric composite filament and the commercially available conductive composite filament (as electrodes). The lattices are made of 4 × 4 × 1 unit cells; lattice dimension is 20 × 20 × 5.4 mm (length × width × thickness). Both the piezoelectric and the conductive composite filaments were dried at 60°C in a vacuum oven for at least one day before the printing process. The piezoelectric and conductive composite filaments were printed in the form of SC lattice using a commercial FFF 3D printer (Makerbot replicator 2, MakerBot Industries, LLC) as shown in Figure 5.6b. FFF 3D printing parameters for making the multi-material piezoelectric composite structures (for both filaments) are: nozzle size = 0.6 mm, extrusion temperature = 230°C, printing speed = 20 mm/s, layer height = 0.2 mm and the printing bed is not heated.

Poling process

To align the dipole moments in the PZT nanoparticles, we built a contact poling setup (Figure 5.6c), which consists of four parts: a poling bath filled with silicone oil (Thermo Scientific), a poling copper rod (~3 mm in diameter), a high voltage power supply (ES60kV negative, 10 Watt, Gamma High Voltage Research, Inc.) and a hot plate (Thermo Scientific™ SuperNuova+™, Fisher Scientific). During the poling process, we put an aluminum plate (20 × 20 × 2 mm) between the copper rod of the poling head and the top surface of the element to ensure a more uniform distribution of the electric field throughout the piezoelectric composite lattices. After the poling process, the silicone oil bath was cooled down to room temperature before removing the electric field to reduce the misalignment of dipole moments. The polarized structures were then washed with soap to remove the residue of silicone oil and dried at room temperature.

Herein, three poling parameters have significant effects on the piezoelectric performance: poling voltage, time and temperature. A sufficiently high poling voltage is crucial to align the randomly oriented dipole moments. Poling time could be tailored to ensure the complete polarization. An elevated poling temperature ($<T_c$) is used to increase the mobility of the crystals. To tailor the poling parameters, we fabricated TPU/30vol%PZT piezoelectric composite films (10 × 10 × 1 mm, 5 layers, 3 replicates for each test condition) and polarized them using five poling voltages (1, 3, 5, 7 and 9 kV) at 80°C for 60 min, five poling temperatures (room temperature ~23, 50, 80, 110 and 140°C) under 5 kV/mm for 60 min and four poling time (30, 60, 90 and 120 min) under 5 kV/mm at 80°C, respectively. After the poling process, the silicone oil bath was cooled down to room temperature before removing the electric field to reduce the misalignment of dipole moments. To investigate the composition of the piezoelectric composite (i.e., PZT volume fraction), we fabricated and polarized piezoelectric composite films with five PZT volume fractions: 15%, 20%, 25%, 30% and 35% (i.e., 53%, 61%, 68%, 73% and 77 % in weight fraction) using the poling parameters 5 kV/mm, 80°C and 60 min. Then we used the poling parameters to polarize the multi-material 3D printed piezoelectric lattices and the multi-material OT piezoelectric composite shoe sole. We built a larger silicone oil poling bath with a dimension of 39.6 × 24.6 × 7.6 cm for the poling process of the multi-material OT piezoelectric composite shoe sole.

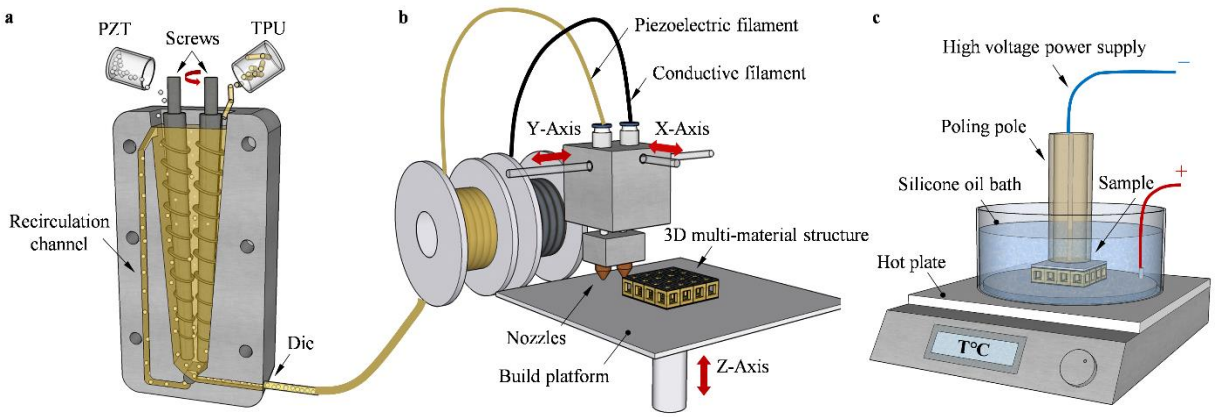

Figure 5.6 Schematic of the fabrication process of a multi-material 3D printed flexible piezoelectric composite lattice (SC lattice is shown): (a) Piezoelectric composite filament fabrication process (matrix: TPU and filler: PZT nanoparticles). (b) Multi-material 3D printing process (yellow filament: the developed TPU/PZT piezoelectric composite filament; black filament: the commercially available TPU/carbon black conductive composite filament). (c) Poling process using a custom-made poling station.

5.4.3 Scanning electron microscopy (SEM) and optical characterization

The microstructure of the TPU/30vol%PZT piezoelectric composite filament extruded from the twin-screw micro-compounder and the bonding between the electrode and the piezoelectric layers of the multi-material 3D printed devices were investigated using SEM observations (TM3030, Hitachi, USA). Samples were coated with a 10 nm layer of chrome before the imaging analysis. The imaging analyses were performed at a 5 kV voltage supply. Filler dispersion was analysed based on the cross-sectional view of extruded filament fractured manually in the liquid nitrogen.

Optical images of the close-up front view and top views of the multi-material 3D printed piezoelectric composite lattices and shoe sole were taken by an optical BX-61, Olympus microscope.

5.4.4 Piezoelectric property characterization

A d_{33} meter (YE2730, Sinocera Piezotronics, Inc.) was used to characterize three piezoelectric coefficients: d_{33}, d_{31} and d_{15}. The open-circuit piezoelectric voltages were collected using a charge amplifier (Piezo Lab Amplifier, MEAS Specialties) in a voltage mode. The data was acquired with

an NI-9239 data acquisition system attached to a USB carrier NI-9162 (National Instruments) and recorded using a custom LabVIEW interface. The average values were calculated from three measurements conducted on three replicates.

5.4.5 Capacitance measurement

The capacitance (*C*) of the TPU/30vol%PZT composite films was measured using an LCR (inductance, capacitance and resistance) meter (3522-50 LCR Hitester, Hioki). The TPU/30vol%PZT composite films with a dimension of 10 × 10 × 1 mm were tested. The average value was calculated from three replicates.

5.4.6 Mechanical characterization

Tensile stiffness and elongation at breakage (%) characterization of the tensile dogbones 3D printed out of pure TPU, piezoelectric TPU/PZT composite (~1.75 mm in diameter) and conductive TPU/carbon black composite filaments were carried out using an MTS Insight™ machine with a 1000 N load cell at a crosshead speed of 50 mm/min and using digital image correlation (DIC) technique. The tensile tests were performed according to ASTM D638 - 14.[48] The tensile dogbones were made into type IV (thickness = 3 mm). To prepare the samples for DIC measurement, a thin layer of white acrylic spray paint (Ultra 2X spray paint, Painter's Touch®) was applied on the surface of each specimen. The speckle pattern with a diameter of ~0.4 mm was then painted with a roller brush to track the speckle pattern displacement during the tensile test. Two long-range focus stereo microscopes were used for the image acquisition at a frequency of 5 Hz. The strain was computed from the displacement of the speckle pattern using the VIC3D micro software (Correlated solutions, version 7.2.4). Five replicates were tested for repetition.

5.4.7 Compression test on the multi-material 3D printed flexible piezoelectric composite lattices with integrated electrodes

The compression tests were carried out on the FD sample and four other types of 3D piezoelectric composite lattices using an MTS Insight™ machine with a 1000 N load cell at a crosshead speed of 500 mm/min. We conducted the compression tests for two conditions: under the same maximum

applied force of 300 N and under the same maximum imposed displacement of 2 mm, respectively. The average of piezoelectric voltage output was calculated from three replicates.

5.4.8 Cyclic compression test and human stomp test on the multi-material OT piezoelectric composite shoe sole

The cyclic compression test was carried out using an MTS Bionix^{TM} test system with a 25 kN load cell with an amplitude of 3 mm at 2 Hz; the 2 Hz frequency was selected to mimic the frequency of human walking. The plantar pressure distribution of the foot on the multi-material OT piezoelectric composite shoe sole was measured using a Medilogic Flex-Sole plantar pressure system (T&T Medilogic Medizintechnik GmbH, Germany) at 400 Hz. The plantar pressure map was placed between the 3D printed PLA foot replica and the multi-material OT piezoelectric composite shoe sole. The human stomp test was simply performed by stomping on the multi-material OT piezoelectric composite shoe sole. The pressure map was placed in the shoe of the tester. The voltage output was recorded and a white LED (3 V, 20 mA) blinked at every stomp of foot.

5.4.9 Finite element analysis

ANSYS APDL was used to conduct the finite element analysis (FEA). One unit cell of the FD sample and the OT lattice were investigated. The boundary condition was that the bottom surfaces of the structures were fixed, and a uniform stress was applied on the top surfaces to obtain the normalized voltage. Table 5.1 lists the input parameters taken from experimentally obtained properties of the bulk TPU/30vol%PZT piezoelectric composite. The element type is Solid 227, which is a 3D quadratic tetrahedral element and has 10 nodes. Table 5.2 (Section S2, Supporting Information) shows the convergence analysis. The number of elements is 39304 for FD and 49801 for OT.

Table 5.1 The input parameters of the bulk TPU/30vol%PZT piezoelectric composite.

Density (kg/m^3)	Elastic property (Modulus and Poisson's ratio)	Dielectric permittivity (F/m)	Piezoelectric coefficient (pC/N)

$\rho = 2.97 \times 10^3$	$Y = 22$ MPa $\nu = 0.43$	$\epsilon_{11} = \epsilon_{22} = 2.0 \times 10^{-10}$ $\epsilon_{33} = 1.59 \times 10^{-10}$	$d_{15} = d_{24} = 4.5$ $d_{31} = d_{32} = -2.1$ $d_{33} = 6.8$

5.5 Supporting information

5.5.1 Eco-friendly recyclable reusable piezoelectric composite material

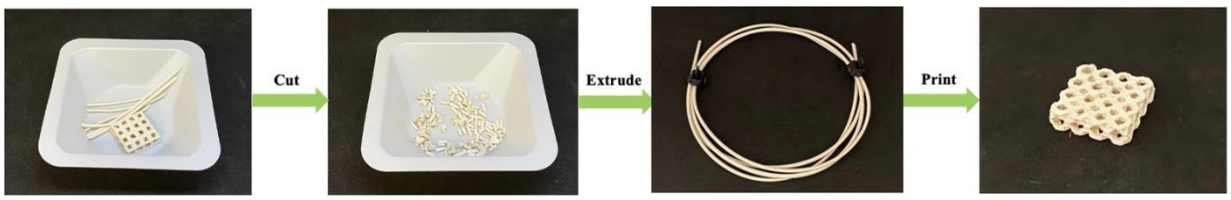

Figure 5.7 FFF 3D printed TPU/PZT composite structures and scrap materials can be recycled to generate new FFF 3D-printable piezoelectric composite filament. They are cut into small pellets and then re-extruded into filaments using the twin-screw micro-compounder. New structures can be FFF 3D printed out of the recycled piezoelectric composite filament. To recycle the piezoelectric composite structures printed with integrated electrodes, we should first peel off the electrode layers on the top and bottom surfaces of the 3D printed piezoelectric structures.

5.5.2 Convergence analysis

Table 5.2 Convergence analysis.

FD		OT	
Element number	Voltage result	Element number	Voltage result
1000	0.32	3805	0.97
2197	0.32	4024	0.97
4913	0.32	8271	0.99

15625	0.32	14653	1.00
39304	0.32	49801	1.00

5.5.3 Dimension of the four types of multi-material 3D printed piezoelectric composite lattices

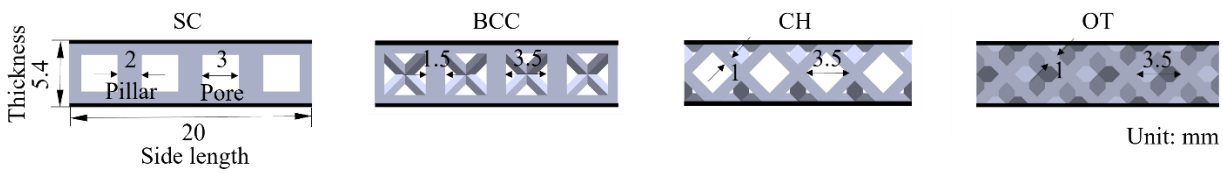

Figure 5.8 Dimension of the as-designed lattices.

Table 5.3 Dimension of the fabricated lattices (Unit: mm). Error bars indicate 95% confidence interval of the mean obtained from three location measurements on three different specimens.

	Type	SC	BCC	CH	OT
Thickness	Measurement	5.43 ± 0.021	5.42 ± 0.012	5.43 ± 0.011	5.41 ± 0.048
	Model	5.4	5.4	5.4	5.4
	Relative error (%)	0.6	0.4	0.6	0.2
Side length	Measurement	20.22 ± 0.080	20.19 ± 0.093	20.28 ± 0.060	20.26 ± 0.074
	Model	20	20	20	20
	Relative error (%)	1.1	1.0	1.4	1.3
Pillar width	Measurement	2.01 ± 0.014	1.54 ± 0.011	1.07 ± 0.024	0.93 ± 0.031
	Model	2	1.5	1	1

	Relative error (%)	0.5	2.7	7	7
	Measurement	2.96 ± 0.013	3.53 ± 0.022	3.48 ± 0.019	3.41 ± 0.026
Pore size	Model	3	3.5	3.5	3.5
	Relative error (%)	1.3	0.9	0.6	2.6

5.5.4 Weight of the FD sample and four types of 3D piezoelectric composite lattices with integrated electrodes

Table 5.4 Weight of the FD and four types of 3D piezoelectric composite lattices with electrodes.

Type	FD	SC	BCC	CH	OT
Weight (g)	5.94	2.97	3.59	2.87	4.3

5.5.5 Effect of high poling voltage ($E \geq 15$ kV) on the d_{33} value of FFF 3D printed piezoelectric TPU/30vol%PZT composites

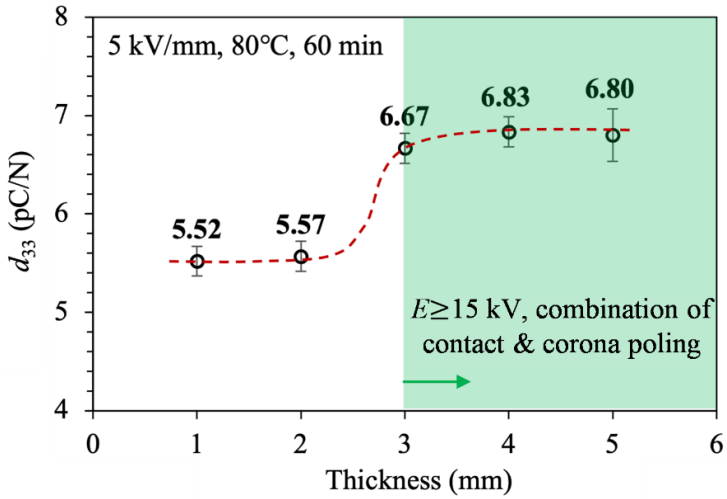

Figure 5.9 The d_{33} values of FFF 3D printed piezoelectric composite films with different thickness (length × width = 10 × 10 mm, thickness = 1, 2, 3, 4, 5 mm) polarized under the electric field of 5

kV/mm. When $E \geq 15$ kV, there is an increase ~ 1.3 pC/N of d_{33} observed due to the combination effect of contact poling and corona poling on the piezoelectric performance. Corona discharge happens due to the strength of the poling electric field exceeds the dielectric strength of the air.[50]

5.5.6 Maximum allowable operating temperature for the FFF 3D printed piezoelectric TPU/30vol%PZT composite

The piezoelectric composite filament developed in this work consists of TPU and 30 vol% PZT. The pure PZT powder has a Curie temperature 360℃. It is suggested that the maximum operating temperature to be half of the Curie temperature, i.e., 180℃. TPU matrix has a melting temperature of 216℃. To investigate the maximum working temperature of the piezoelectric composites, the polarized 3D printed TPU/30vol%PZT composite films (10 × 10 × 5 mm, three tested replicates) were heated in the silicone oil bath at 30, 40, 50, 60, 70, 80, 90 and 100°C for one hour, respectively, and the piezoelectric coefficient (d_{33}) were measured using a d_{33} meter at three different locations before and after being heated (Figure 5.10). We found that the piezoelectric composite films start to lose its piezoelectric performance gradually when the temperature is above 80°C, probably due to the misalignment of the domains. As a consequence, during the poling process, we need to cool down the piezo elements below 80°C before removing the poling electric field in order to avoid the misalignment of the domains.

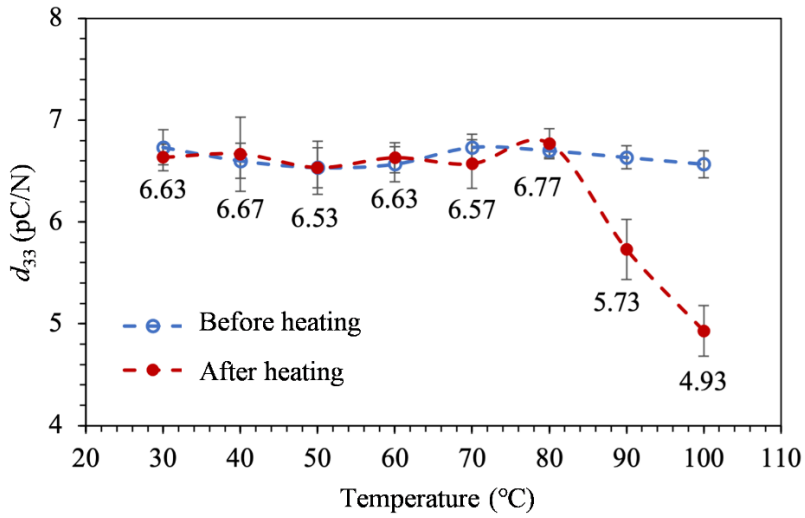

Figure 5.10 Piezoelectric coefficient d_{33} of printed polarized composite films before and after being heated at 30, 40, 50, 60, 70, 80, 90, and 100°C for one hour.

Acknowledgement

We acknowledge the financial support from National Science and Engineering Research Council (NSERC), Discovery program (#RGPIN-4566-2018 and RGPIN-2016-0471) and the Department of National Defence (DND) (Grant#: DGDND-2018-00011). A.H. Akbarzadeh acknowledges the financial support from the Canada Research Chairs program. Mrs. Rui Tao and Mr. Jiahao Shi acknowledge the financial support that they received through a scholarship from the China Scholarship Council (CSC). We are thankful for the instrument access and the suggestions kindly provided by Prof. Mickael Begon, Prof. Frédéric Sirois and Prof. Sharmistha Bhadra; and the scientific and technical advice from our colleagues Dr. Rouhollah Farahani, Dr. Kambiz Chizari, Mr. Lingyu Yue, Mr. Dogan Arslan, Ms. Jennifer Dowling-Medley, Mr. Gauthier Desmyttere and Mr. Kiran Kumar Sappati; and the technical support from the technicians Mr. Yanik Landry-Ducharme, Mr. Laurent Mouden and Mr. Christian-Charles Martel.

References

(1) Liu, Q.; Wang, X. X.; Song, W. Z.; Qiu, H. J.; Zhang, J.; Fan, Z.; Yu, M.; Long, Y. Z. Wireless Single-Electrode Self-Powered Piezoelectric Sensor for Monitoring. ACS Appl. Mater. Interfaces 2020, 12 (7), 8288–8295.

(2) Tian, G.; Deng, W.; Gao, Y.; Xiong, D.; Yan, C.; He, X.; Yang, T.; Jin, L.; Chu, X.; Zhang, H.; Yan, W.; Yang, W. Rich Lamellar Crystal Baklava-Structured PZT/PVDF Piezoelectric Sensor toward Individual Table Tennis Training. Nano Energy 2019, 59 (February), 574–581.

(3) Ding, R.; Liu, H.; Zhang, X.; Xiao, J.; Kishor, R.; Sun, H.; Zhu, B.; Chen, G.; Gao, F.; Feng, X.; Chen, J.; Chen, X.; Sun, X.; Zheng, Y. Flexible Piezoelectric Nanocomposite Generators Based on Formamidinium Lead Halide Perovskite Nanoparticles. Adv. Funct. Mater. 2016, 26 (42), 7708–7716.

(4) Mariello, M.; Fachechi, L.; Guido, F.; De Vittorio, M. Multifunctional Sub-100 μm Thickness Flexible Piezo/Triboelectric Hybrid Water Energy Harvester Based on Biocompatible AlN and Soft Parylene C-PDMS-EcoflexTM. Nano Energy 2021, 83 (December 2020), 105811.

(5) Ji, S. H.; Lee, W.; Yun, J. S. All-in-One Piezo-Triboelectric Energy Harvester Module Based on Piezoceramic Nanofibers for Wearable Devices. ACS Appl. Mater. Interfaces 2020, 12 (16), 18609–18616.

(6) Wu, J.; Shi, H.; Zhao, T.; Yu, Y.; Dong, S. High-Temperature BiScO3-PbTiO3 Piezoelectric Vibration Energy Harvester. Adv. Funct. Mater. 2016, 26 (39), 7186–7194.

(7) Liu, X.; Shi, Q.; Lin, Y.; Kojima, M.; Mae, Y.; Fukuda, T.; Huang, Q.; Arai, T. Multifunctional Noncontact Micromanipulation Using Whirling Flow Generated by Vibrating a Single Piezo Actuator. Small 2019, 15 (5), 1–9.

(8) S, M.; Karanth P, N.; Kulkarni, S. M. Performance Analysis of Valveless Micropump with Disposable Chamber Actuated through Amplified Piezo Actuator (APA) for Biomedical Application. Mechatronics 2020, 67 (March), 102347.

(9) Shi, J.; Akbarzadeh, A. H. 3D Hierarchical Lattice Ferroelectric Metamaterials. Int. J. Eng. Sci. 2020, 149, 103247.

(10) Shi, J.; Akbarzadeh, A. H. Architected Cellular Piezoelectric Metamaterials: Thermo-Electro-Mechanical Properties. Acta Mater. 2019, 163, 91–121.

(11) Shi, J.; Akbarzadeh, A. H. Hierarchical Cellular Ferroelectric Metamaterials: A Design Motif to Enhance Multifunctional Figures of Merit. Compos. Struct. 2020, 250 (November 2019), 112395.

(12) Prume, K.; Muralt, P.; Calame, F.; Schmitz-Kempen, T.; Tiedke, S. Piezoelectric Thin Films: Evaluation of Electrical and Electromechanical Characteristics for MEMS Devices. IEEE Trans. Ultrason. Ferroelectr. Freq. Control 2007, 54 (1), 8–14.

(13) Covaci, C.; Gontean, A. Piezoelectric Energy Harvesting Solutions: A Review. Sensors (Switzerland) 2020, 20 (12), 1–37.

(14) Hajati, A. Ultra Wide-Bandwidth Micro Energy Harvester. 2010, 197.

(15) Newnham, R. E. Properties of Materials; 2005.

(16) Zhang, S.; Yu, F. Piezoelectric Materials for High Temperature Sensors. J. Am. Ceram. Soc. 2011, 94 (10), 3153–3170.

(17) Safari, Ahmad, E. K. A. Piezoelectric and Acoustic Materials for Transducer Application; 2008.

(18) Piezoelectricity, APC International, Ltd. https://www.americanpiezo.com/knowledge-center/piezo-theory/piezoelectricity.html.

(19) Stuber, V. L.; Deutz, D. B.; Bennett, J.; Cannel, D.; de Leeuw, D. M.; van der Zwaag, S.; Groen, P. Flexible Lead-Free Piezoelectric Composite Materials for Energy Harvesting Applications. Energy Technol. 2019, 7 (1), 177–185.

(20) Lu, X.; Qu, H.; Skorobogatiy, M. Piezoelectric Micro- and Nanostructured Fibers Fabricated from Thermoplastic Nanocomposites Using a Fiber Drawing Technique: Comparative Study and Potential Applications. ACS Nano 2017, 11 (2), 2103–2114.

(21) Sim, H. J.; Choi, C.; Lee, C. J.; Kim, Y. T.; Spinks, G. M.; Lima, M. D.; Baughman, R. H.; Kim, S. J. Flexible, Stretchable and Weavable Piezoelectric Fiber. Adv. Eng. Mater. 2015, 17 (9), 1270–1275.

(22) Su, H.; Wang, X.; Li, C.; Wang, Z.; Wu, Y.; Zhang, J.; Zhang, Y.; Zhao, C.; Wu, J.; Zheng, H. Enhanced Energy Harvesting Ability of Polydimethylsiloxane-BaTiO3-Based Flexible Piezoelectric Nanogenerator for Tactile Imitation Application. Nano Energy 2021, 83 (December 2020), 105809.

(23) Hanani, Z.; Izanzar, I.; Amjoud, M.; Mezzane, D.; Lahcini, M.; Uršič, H.; Prah, U.; Saadoune, I.; Marssi, M. El; Luk'yanchuk, I. A.; Kutnjak, Z.; Gouné, M. Lead-Free Nanocomposite Piezoelectric Nanogenerator Film for Biomechanical Energy Harvesting. Nano Energy 2021, 81 (November 2020).

(24) Bodkhe, S.; Noonan, C.; Gosselin, F. P.; Therriault, D. Coextrusion of Multifunctional Smart Sensors. Adv. Eng. Mater. 2018, 20 (10), 1800206.

(25) Bodkhe, S.; Turcot, G.; Gosselin, F. P.; Therriault, D. One-Step Solvent Evaporation-Assisted 3D Printing of Piezoelectric PVDF Nanocomposite Structures. ACS Appl. Mater. Interfaces 2017, 9 (24), 20833–20842.

(26) Bodkhe, S.; Rajesh, P. S. M.; Gosselin, F. P.; Therriault, D. Simultaneous 3D Printing and Poling of PVDF and Its Nanocomposites. ACS Appl. Energy Mater. 2018, 1 (6), 2474–2482.

(27) Xu, C.; Quinn, B.; Lebel, L. L.; Therriault, D.; L'espérance, G. Multi-Material Direct Ink Writing (DIW) for Complex 3D Metallic Structures with Removable Supports. ACS Appl. Mater. Interfaces 2019, 11 (8), 8499–8506.

(28) Yao, D.; Cui, H.; Hensleigh, R.; Smith, P.; Alford, S.; Bernero, D.; Bush, S.; Mann, K.; Wu, H. F.; Chin-Nieh, M.; Youmans, G.; Zheng, X. Achieving the Upper Bound of Piezoelectric Response in Tunable, Wearable 3D Printed Nanocomposites. Adv. Funct. Mater. 2019, 29 (42).

(29) Cui, H.; Hensleigh, R.; Yao, D.; Maurya, D.; Kumar, P.; Kang, M. G.; Priya, S.; Zheng, X. Three-Dimensional Printing of Piezoelectric Materials with Designed Anisotropy and Directional Response. Nat. Mater. 2019, 18 (3), 234–241.

(30) Wu, Q.; Zou, S.; Gosselin, F. P.; Therriault, D.; Heuzey, M. C. 3D Printing of a Self-Healing Nanocomposite for Stretchable Sensors. J. Mater. Chem. C 2018, 6 (45), 12180–12186.

(31) Wei, H.; Cauchy, X.; Navas, I. O.; Abderrafai, Y.; Chizari, K.; Sundararaj, U.; Liu, Y.; Leng, J.; Therriault, D. Direct 3D Printing of Hybrid Nanofiber-Based Nanocomposites for Highly Conductive and Shape Memory Applications. ACS Appl. Mater. Interfaces 2019, 11 (27), 24523–24532.

(32) Sydney Gladman, A.; Matsumoto, E. A.; Nuzzo, R. G.; Mahadevan, L.; Lewis, J. A. Biomimetic 4D Printing. Nat. Mater. 2016, 15 (4), 413–418.

(33) Ge, Q.; Sakhaei, A. H.; Lee, H.; Dunn, C. K.; Fang, N. X.; Dunn, M. L. Multimaterial 4D Printing with Tailorable Shape Memory Polymers. Sci. Rep. 2016, 6 (July), 1–11.

(34) Kim, K.; Zhu, W.; Qu, X.; Aaronson, C.; McCall, W. R.; Chen, S.; Sirbuly, D. J. 3D Optical Printing of Piezoelectric Nanoparticle-Polymer Composite Materials. ACS Nano 2014, 8 (10), 9799–9806.

(35) Yuan, C.; Wang, F.; Qi, B.; Ding, Z.; Rosen, D. W.; Ge, Q. 3D Printing of Multi-Material Composites with Tunable Shape Memory Behavior. Mater. Des. 2020, 193, 1–10.

(36) Wu, J.; Yuan, C.; Ding, Z.; Isakov, M.; Mao, Y.; Wang, T.; Dunn, M. L.; Qi, H. J. Multi-Shape Active Composites by 3D Printing of Digital Shape Memory Polymers. Sci. Rep. 2016, 6 (November 2015), 1–11.

(37) Wang, Z.; Yuan, X.; Yang, J.; Huan, Y.; Gao, X.; Li, Z.; Wang, H.; Dong, S. 3D-Printed Flexible, Ag-Coated PNN-PZT Ceramic-Polymer Grid-Composite for Electromechanical Energy Conversion. Nano Energy 2020, 73 (April), 104737.

(38) Kim, H.; Fernando, T.; Li, M.; Lin, Y.; Tseng, T.-L. B. Fabrication and Characterization of 3D Printed BaTiO 3 /PVDF Nanocomposites. 2018.

(39) Kim, H.; Johnson, J.; Chavez, L. A.; Garcia Rosales, C. A.; Tseng, T.-L. B.; Lin, Y. Enhanced Dielectric Properties of Three Phase Dielectric MWCNTs/BaTiO3/PVDF Nanocomposites for Energy Storage Using Fused Deposition Modeling 3D Printing. Ceram. Int. 2018, 44 (8), 9037–9044.

(40) Kim, H.; Wilburn, B. R.; Castro, E.; Garcia Rosales, C. A.; Chavez, L. A.; Tseng, T. L. B.; Lin, Y. Multifunctional SENSING Using 3D Printed CNTs/BaTiO 3 /PVDF Nanocomposites. J. Compos. Mater. 2019, 53 (10), 1319–1328.

(41) Tang, E. L.; Wang, L.; Han, Y. F. Space Debris Positioning Based on Two-Dimensional PVDF Piezoelectric Film Sensor. Adv. Sp. Res. 2019, 63 (8), 2410–2421.

(42) Zhu, P.; Wang, Y.; Wang, Y.; Mao, H.; Zhang, Q.; Deng, Y. Flexible 3D Architectured Piezo/Thermoelectric Bimodal Tactile Sensor Array for E-Skin Application. Adv. Energy Mater. 2020, 10 (39), 1–8.

(43) Cho, G.; Jeong, K.; Paik, M. J.; Kwun, Y.; Sung, M. Performance Evaluation of Textile-Based Electrodes and Motion Sensors for Smart Clothing. IEEE Sens. J. 2011, 11 (12), 3183–3193.

(44) Mokhtari, F.; Shamshirsaz, M.; Latifi, M.; Foroughi, J. Nanofibers-Based Piezoelectric Energy Harvester for Self-Powered Wearable Technologies. Polymers (Basel). 2020, 12 (11), 1–15.

(45) Haghiashtiani, G.; Greminger, M. A. Fabrication, Polarization, and Characterization of PVDF Matrix Composites for Integrated Structural Load Sensing. 2015.

(46) Kokkinis, D.; Schaffner, M.; Studart, A. R. Multimaterial Magnetically Assisted 3D Printing of Composite Materials. Nat. Commun. 2015, 6.

(47) Skylar-Scott, M. A.; Mueller, J.; Visser, C. W.; Lewis, J. A. Voxelated Soft Matter via Multimaterial Multinozzle 3D Printing. Nature 2019, 575 (7782), 330–335.

(48) ASTM International. ASTM D638 - 14. Standard Test Method for Tensile Properties of Plastics. Https://Www.Astm.Org/Standards/D638.Htm.

(49) Mahapatra, S. Das; Mohapatra, P. C.; Aria, A. I.; Christie, G.; Mishra, Y. K.; Hofmann, S.; Thakur, V. K. Piezoelectric Materials for Energy Harvesting and Sensing Applications: Roadmap for Future Smart Materials. Adv. Sci. 2021, 8 (17).

(50) Troughton, M. J. Handbook of Plastics Joining; 2009.

CHAPTER 6 ARTICLE 3: MULTI-MATERIAL FREEFORM 3D PRINTING OF FLEXIBLE PIEZOELECTRIC COMPOSITE SENSORS USING A SUPPORTING FLUID

Rui Tao, Floriane Granier, and Daniel Therriault*

Laboratory for Multiscale Mechanics (LM^2), Department of Mechanical Engineering, Research Center for High Performance Polymer and Composite Systems (CREPEC), Polytechnique Montreal, Montreal, QC, H3T 1J4, Canada

Submitted in Additive Manufacturing on March 25th, 2022

Abstract

Three-dimensional (3D) printed flexible piezoelectric devices featuring conformal or freeform geometries show great potential for being fabricated into wireless sensors and energy harvesters with tailorable mechanical stiffness and piezoelectric response. In our work, supporting fluid-assisted multi-material direct-ink writing (DIW) 3D printing technology has been successfully utilized to fabricate flexible conformal or freeform piezoelectric composite sensors with integrated electrodes. The printing technique relies on the DIW of two paste-like materials: piezoelectric and conductive composite inks. A comprehensive characterization of the inks (i.e., piezoelectric or conductive behaviors, rheological and mechanical properties) and the rheological behavior of the supporting fluid are performed. Polydimethylsiloxane (PDMS)/30vol% lead zirconate titanate (PZT), PDMS/25vol% silver (Ag) and mineral oil/6% (w/v) fumed silica are the formulations for piezoelectric ink, conductive ink and supporting fluid, respectively. Three types of piezoelectric composite demonstrators which are a multi-layer planar film, a conformal non-planar hemisphere and a 3D structure composed of six spirals printed vertically between two hexagon layers (freeform spiral-hexagon), are fabricated and tested under tension or compression tests. The piezoelectric performance is consistent with the applied stress in all the tests. For example, the freeform spiral-hexagon piezoelectric sensor has a peak-to-peak voltage output of 86.39 ± 1.145 mV when it is subjected to a cyclic compression force at 8 Hz for more than 800 cycles. The dimensional accuracy measurements using an optical microscope and the microstructure images taken using a scanning electron microscope (SEM) show that the fabricated 3D structures have good shape

fidelity (with a maximum relative error of ~3.5%) when compared to the designed models. Our fabrication approach opens a new way to fabricate conformal and freeform piezoelectric structures with integrated electrodes from flexible composites for sensing and energy harvesting applications.

6.1 Introduction

Recent interests in wireless wearable piezoelectric sensors, flexible energy harvesters, and smart artificial skins have led to scores of investigations on stretchable piezoelectric materials.[1–7] These devices seek for new fabrication schemes that enable the fabrication of conformal and freeform complex geometries.[8–11] Conformal geometries feature uneven or curved surfaces.[12] Freeform geometries are more complex than conformal 3D geometries, which represent freedom design structures.[13] The freeform geometries have the advantages of being more compact (i.e., lightweight) and having greater design feasibility.

Additive manufacturing, also referred as three-dimensional (3D) printing, is a family of several processes that enables the fabrication of a 3D shape usually in a layer-by-layer approach. Traditionally, extrusion-based 3D printing methods such as direct-ink writing (DIW) technique are used to print freeform structures. As first, the inks should possess a shear-thinning behavior, which can benefit the flowability through the dispensing needle.[14,15] After the ink was extruded out of the needle, the shear stress is relieved and the ink viscosity increases again, which helps to retain its shape. Also, the functional ink materials must exhibit rapid solidification properties to retain the shape as extruded. There are usually two ways to enable rapid solidification: one way is to use fast-evaporation solvents[16] that are usually toxic; another way is to use ultraviolet (UV)-assisted DIW 3D printing technique, but this significantly limits the choice of printable materials.[17,18] To address these challenges, embedded 3D printing (e-3DP)[19–23] or DIW 3D printing in the supporting fluid[24] techniques have been developed to fabricate soft tissues or strain sensors for biomedical applications. The supporting fluid behaves as a Herschel-Bulkley fluid. The deposited filament is physically entrapped in the space between the crosslinked microgels, which temporarily flow under the stress generated by a moving dispensing needle and then rapidly recover to a jammed solid state to support the deposited filaments.[25,26] In addition, optically transparent, non-toxic and easy to clean properties are also the requirements for the supporting fluids. A variety of supporting fluid materials such as mineral oil/fumed silica,[27] deionized water

(DW)/dry Laponite,[28,29] DW/Carbopol,[30–33] DW/pluronic F-127,[34,35] DW/low acyl Gellan Gum,[36,37] DW/alginate,[38,39] Ultrez 30/Carbopol,[40] PF-$CaCl_2$/Laponite,[13,41] and DW/poloxamer/poly(ethylene glycol)[42] have been investigated.

An issue related to the manufacturing of piezoelectric devices is that an extra step is usually required to add electrodes on the piezoelectric elements for collecting the generated charges. The commonly used techniques to create the electrodes are painting,[43] screen printing,[44] sputtering[45] or attaching conductive tape or fabrics.[46,47] Several researchers have fabricated piezoelectric elements and electrodes in a single manufacturing process. Lu *et al.* developed thermal-mechanically drawn piezoelectric fibers consisting of alternating layers of piezoelectric electrospun nanocomposites (polyvinylidene fluoride enhanced with barium titanate, PZT or carbon nanotubes) and commercially available conductive composites (i.e., carbon black filled polyethylene).[48,49] Bodkhe *et al.* co-extruded piezoelectric filament with integrated electrodes using DIW technique.[50] Also, several researchers used a multi-material 3D printing technology[51–53] to co-fabricate electrodes with 3D piezoelectric structure in a single manufacturing process.[54] However, the fabricated structures are limited to one-dimensional fiber, two dimensional film or simple 3D scaffold shapes.

This work presents a fabrication approach based on multi-material DIW 3D printing in a supporting fluid bath to fabricate multi-layer, conformal and freeform flexible piezoelectric sensors with integrated electrodes in a single manufacturing process. Various concentrations of fumed silica nanoparticles were added into the mineral oil to find the best supporting behavior of the mineral oil/fumed silica supporting fluid with the proper yield stress. We also developed flexible piezoelectric polydimethylsiloxane (PDMS)/PZT and conductive PDMS/Ag composite materials as printing inks. The piezoelectric and conductive, rheological, and mechanical properties of the inks were investigated. The dimensional accuracy and piezoelectric performance of the three types of multi-material piezoelectric composite demonstrators prove that the developed composite materials and manufacturing technique could be further employed for the production of various freeform and conformal piezoelectric sensing and energy harvesting applications.

6.2 Results and discussion

Figure 6.1 presents the supporting performance of the supporting fluid with different compositions, the mechanism and the required rheological behavior. Figure 6.1a schematically illustrates a single

filament deposited in the supporting fluid with different fumed silica concentrations, the images are shown in Figure 6.7 (Section S1, Supporting Information). The deposited filament is discontinuous and dragged by the dispensing needle in the 5% (w/v) supporting fluid (Figure 6.1aI). When the concentration of fumed silica is too high, i.e., above 7% (w/v), the crevasse can be seen along the movement of the dispensing needle (Figure 6.1aIII). The crevasse adversely affects the following support performance of the supporting fluid. In the 6% (w/v) supporting fluid, the deposited filament is well supported without the introduction of any crevasse (Figure 6.1aII).[25]

The mechanism of the supporting performance of mineral oil/fumed silica is illustrated in Figure 6.1b.[27] When the dispensing needle moves in the mineral oil/6%(w/v) fumed silica supporting fluid, the shear stress induced by the dispensing needle is higher than the yield stress of the supporting fluid. Thus, the fumed silica aggregates are disrupted and flow like fluid to fill out the crevasse induced by the needle movement. Conversely, the scattered fumed silica aggregates recover to the stable 3D network when the dispensing needle leaves. Therefore, the fumed silica aggregates are stable like solid to support the deposited filaments.

The yield stress is the transition threshold between solid and fluid states of the mineral oil/fumed silica supporting fluid. The supporting fluid having a yield stress behaves like solid when the applied stress is lower than the yield stress, while it flows like fluid when the applied stress is higher than the yield stress.[27,29] To obtain the yield stress, the mineral oil/fumed silica nanoparticle suspensions with different compositions were tested in a rheometer in a steady sweep mode at different shear rates and the corresponding shear stresses were recorded. As illustrated in Figure 6.1c, we observed that for suspensions with different nanoparticle concentrations, shear stress increases with the increase of shear rate. The yield stress also increases with the addition of the fumed silica concentration. The yield stresses of the fumed silica nanoparticle suspensions are calculated by fitting the shear stress τ and shear rate $\dot{\gamma}$ data in the Herschel-Bulkley model[58]:

$$\tau = \tau_0 + K\dot{\gamma}^n \tag{6-1}$$

where τ_0 is the yield stress (Pa), n is the flow index, and K is the consistency index (Pa·s^n). The respective fitted Herschel-Bulkley parameters τ_0, n and K are listed in Table 6.1. The model shows good agreement with the rheometry data in both low and high $\dot{\gamma}$ regions, confirming the choice of the Herschel-Bulkley model to calculate the yield stress of the developed supporting fluids. The

calculated yield stresses of the fumed silica nanoparticle suspensions at the concentrations of 5, 6, and 7% (w/v) are 34.41, 86.73 and 105.72 Pa, respectively. The mineral oil/6%(w/v) fumed silica supporting fluid with a yield stress of 86.73 Pa shows a good supporting behavior.

Table 6.1 Parameters of the Herschel-Bulkley fits for the mineral oil/fumed silica supporting fluids with different fumed silica concentrations (data from Figure 6.1c).

Fluid type	Yield stress, τ_0 (Pa)	Flow index, n	Consistency index, K (Pa·s^n)
5% (w/v)	34.41 $\pm$ 1.420	0.48 $\pm$ 0.016	7.67 $\pm$ 0.243
6% (w/v)	86.73 $\pm$ 2.410	0.39 $\pm$ 0.006	26.06 $\pm$ 1.041
7% (w/v)	105.72 $\pm$ 1.626	0.37 $\pm$ 0.002	36.56 $\pm$ 1.546

Results are mean $\pm$ 95% confidence interval obtained from three replicates.

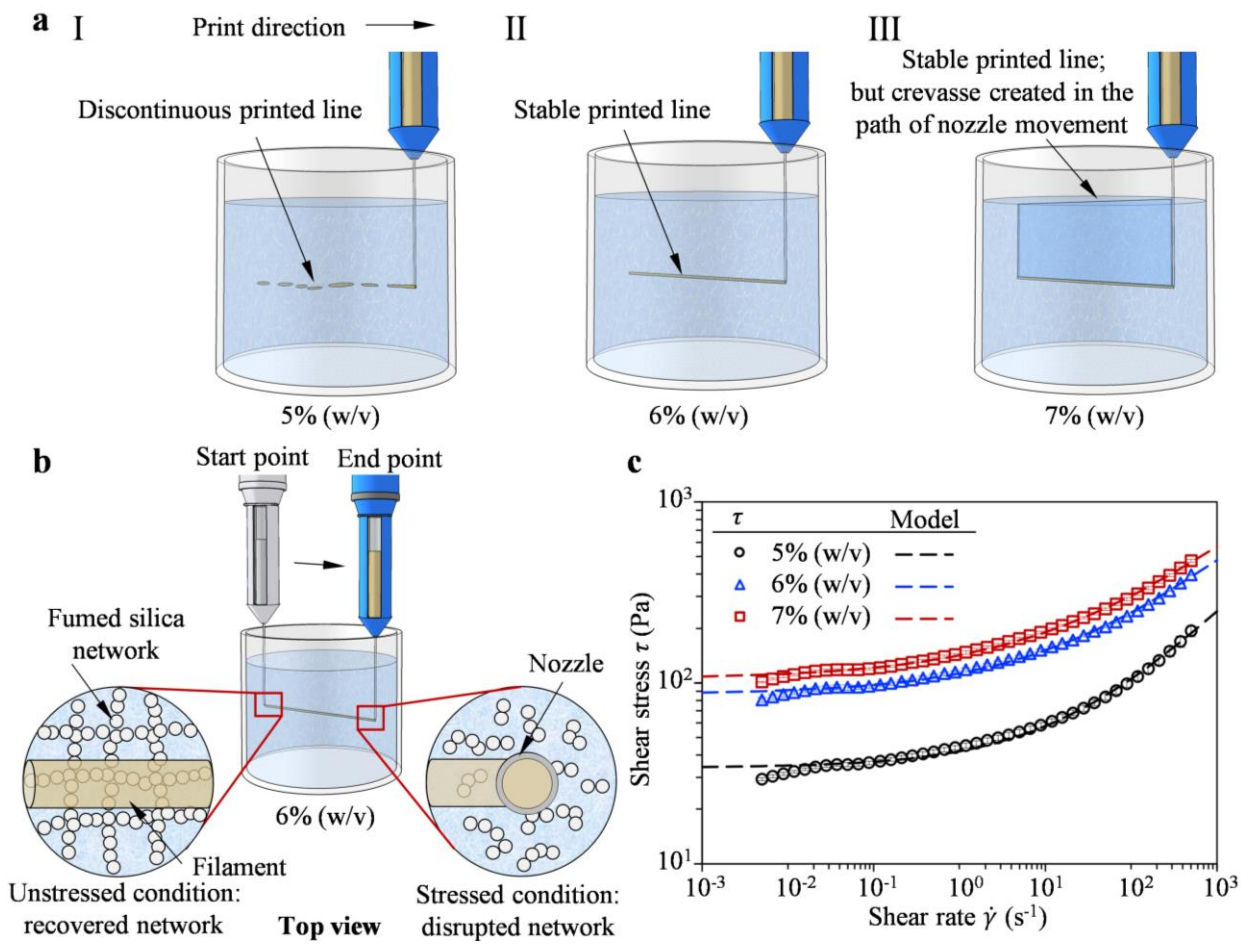

Figure 6.1 Characterization of the supporting fluid with different fumed silica concentrations: (a) Schematic of the supporting behavior of the supporting fluids with different fumed silica concentrations (5%, 6% and 7% (w/v)). (b) The mechanism of the fumed silica supporting network in unstressed and stressed conditions during the printing process. (c) Shear stress with respect to shear rate of the supporting fluids with different fumed silica concentrations (dashed lines are fitted Herschel-Bulkley models).

Upon the supporting behavior test and the yield stress characterization of the supporting fluid with different fumed silica concentrations, we chose to use mineral oil/6%(w/v) fumed silica supporting fluid in this work. The next step is to find out the piezoelectric and conductive ink compositions. Figure 6.2a shows the piezoelectric behavior of the PDMS/PZT composites with different PZT volume fractions: 10, 20, 30 and 40 vol%. Although the PDMS/40vol%PZT composite exhibits the highest d_{33} value of 6.30 pC/N, it usually blocks the nozzle (diameter = 0.6 mm). Thus, we

decided to use the PDMS/30vol%PZT composite having a d_{33} value of 4.43 pC/N and exhibiting stable flow through the nozzle as the piezoelectric ink formulation. Figure 6.2b depicts the conductive behavior of the PDMS/Ag composites with different Ag volume fractions: 20, 25 and 30 vol%. The PDMS/20vol%Ag composite is not conductive as marked in red. The PDMS/30vol%Ag composite shows the highest conductivity of 17.6 S/m. However, we chose to use the PDMS/25vol%Ag composite because of the high price of Ag nanoflakes.

Figure 6.2c and 6.2d report the effect of shear rates on the viscoelastic properties of the PDMS/PZT and PDMS/Ag with different compositions using data from rotational rheometer (at low shear rates) and capillary flow test (at high shear rates). The open symbols in Figure 6.2c and 6.2d present the viscosity of the composites with different filler concentrations obtained through rotational rheometry with respect to the shear rate. The process-related apparent viscosities of the composites with different filler concentrations are presented by solid symbols in Figure 6.2c and 6.2d. All inks exhibit a pronounced shear-thinning response as evidenced by an important decrease in viscosity as the share rate increases. For example, the apparent viscosity of the PDMS/30vol%PZT piezoelectric composite ink at a shear rate of around 28 s^{-1} is ~204 Pa·s and nearly 4 orders of magnitude smaller than the viscosity of ~1.8×10^6 Pa·s measured by rotational rheometer at low shear rates. The viscosity of the inks increases with filler content at all shear rates, which will affect 3D printability. The data points gap observed in the shear rate range of $10^0 \leq \dot{\gamma} \leq 10^1$ s^{-1} is due to measurement instabilities in the rotational rheometer caused by material yielding and separating from the parallel plates. Neither was it possible with the capillary flow method, because higher extrusion pressure for the material to flow through the nozzle is required. A power-law (Ostwald de Waele) model is commonly used to assume the shear-thinning behaviour of composite materials.[59–61] The power-law model relates shear viscosity η to shear rate $\dot{\gamma}$ as:

$$\eta = K\dot{\gamma}^{n-1} \tag{2}$$

where n is the flow index ($0 < n < 1$), and K is the consistency index (Pa·s^n). The respective fitted power-law parameters n and K for each ink formulation are listed in Table 6.2. Flow index values $n < 1$ depict the shear-thinning nature of the inks. The model shows good agreement with the rheometry and capillary data in both low and high $\dot{\gamma}$ regions, confirming the choice of the power-law viscosity model to describe the shear-thinning behavior of the developed inks.

Table 6.2 Parameters of the power-law fits for the piezoelectric and conductive composite inks with different filler contents (data from Figure 6.2c and 6.2d).

Ink type	Flow index, n	Consistency index, k (Pa·s^n)
PDMS/10vol%PZT	0.274 ± 0.0082	128 ± 0.9
PDMS/20vol%PZT	0.201 ± 0.0091	530 ± 0.8
PDMS/30vol%PZT	0.159 ± 0.0103	3,692 ± 1.6
PDMS/25vol%Ag	0.268 ± 0.0176	3,986 ± 1.2
PDMS/30vol%Ag	0.248 ± 0.0102	10,206 ± 6.8

Results are mean ± 95% confidence interval obtained from three replicates.

Mechanical tensile tests were carried out to investigate the mechanical behavior (i.e., mechanical stretchability) of the selected formulations i.e., the PDMS/30vol%PZT piezoelectric composite and PDMS/25vol%Ag conductive composite compositions as they show the highest piezoelectric or conductive properties while being printable (shear-thinning behavior, $n < 1$). Figures 6.2e and 6.2f show the average stress-strain curves of the three tested replicates. All types of piezoelectric and conductive composite films show a relatively long linear regime. The ultimate stress at failure and stiffness are improving with filler concentration. We found that both the PDMS/30vol%PZT piezoelectric composite (ultimate stress at failure = 2.86 ± 0.067 MPa; Young's modulus = 9.7 ± 0.020 MPa) and PDMS/25vol%Ag conductive composite (ultimate stress at failure = 1.59 ± 0.076 MPa; Young's modulus = 8.2 ± 0.046 MPa) exhibit an elongation at break of up to 30%, making them well suited for flexible or soft piezoelectric sensing devices.

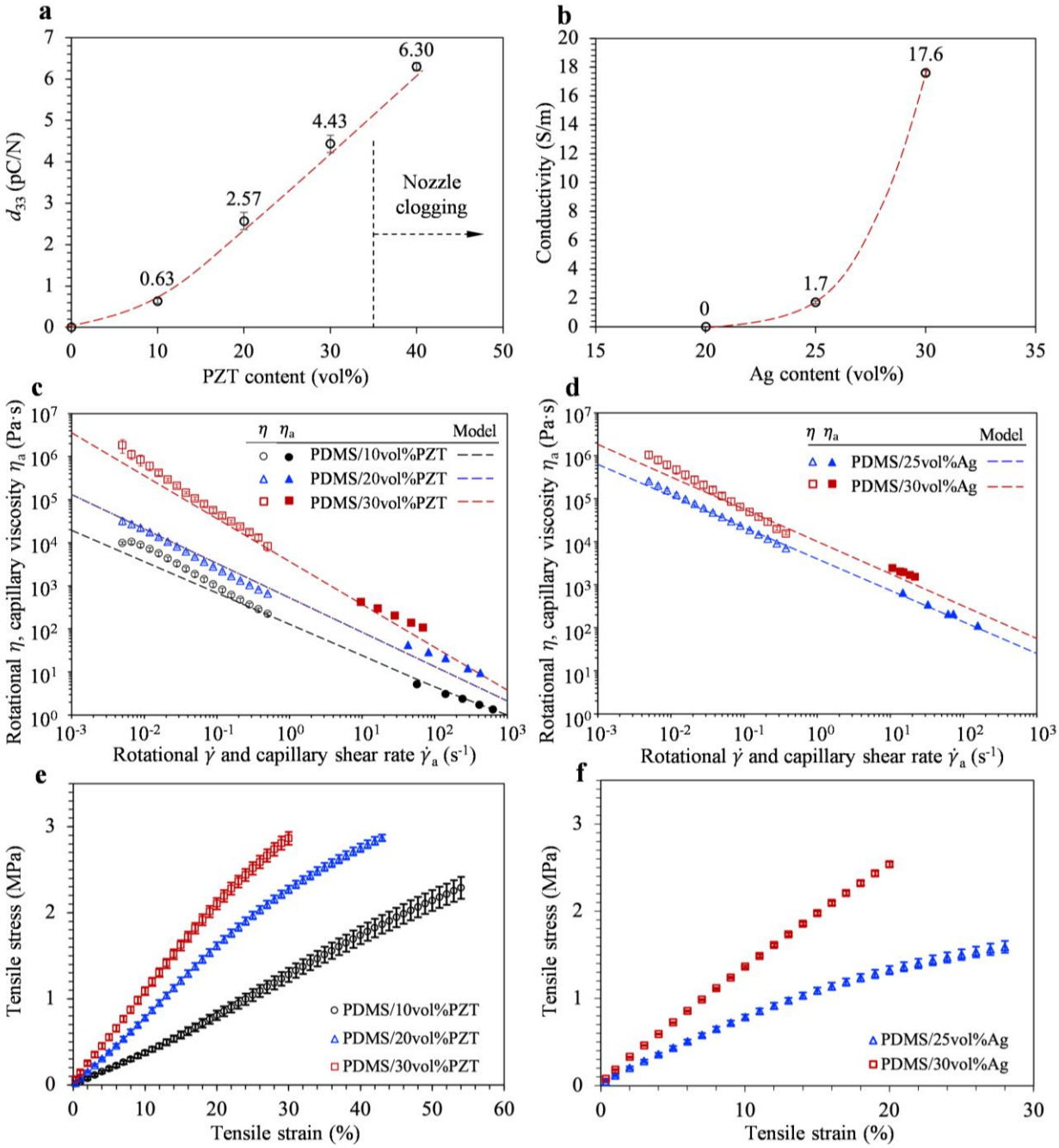

Figure 6.2 Characterization of the developed flexible piezoelectric PDMS/PZT and conductive PDMS/Ag composite materials: (a) d_{33} of piezoelectric composites with different PZT volume fractions. (b) Conductivity of conductive composites with different Ag volume fractions (dashed lines are trend lines). (c-d) Viscoelastic (dashed lines are fitted shear-thinning power-law models), and (e-f) mechanical properties of the piezoelectric and conductive composites with different filler

concentrations. Error bars indicate 95% confidence interval of the mean obtained from three replicates.

Three types of piezoelectric composite structures as demonstrators were designed and fabricated: a multi-layer planar film, a conformal non-planar hemisphere and a freeform spiral-hexagon (Figure 6.3a). The dimensions of the fabricated structures are listed in Table 6.4 (Section S2, Supporting Information). The maximum geometrical error compared to the designed model is ~3.5%, which indicates that the dimensional accuracy of this printing technique is acceptable. The images of the printed structures within or out of the supporting bath indicate that the patterned features do retain their shape after the printing and curing processes (Figure 6.3b).

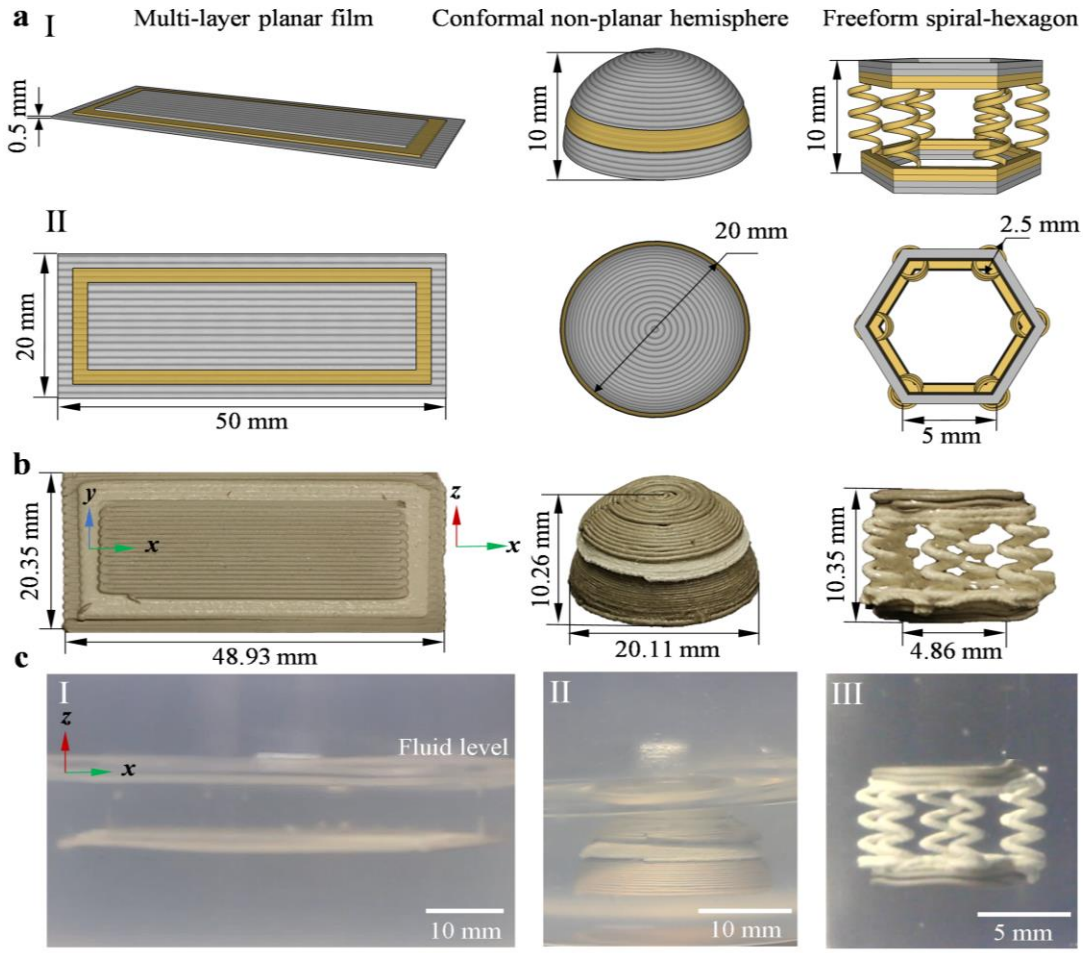

Figure 6.3 Design of the multi-material 3D printed flexible piezoelectric composite sensors with integrated electrodes: (a) 3D models (I: front view; II: top view), (b) Images of the cured structures

taken out of the supporting fluid, and (c) Images of the uncured structures in the supporting fluid after the printing process of the three types of multi-material 3D printed flexible piezoelectric composite structures with integrated electrodes: a multi-layer planar film, a conformal non-planar hemisphere and a freeform spiral-hexagon.

Figure 6.4a shows the locations of the samples cut from the three types of multi-material 3D printed piezoelectric composite sensors with integrated electrodes for SEM observations. We observed that the SEM images in Figure 6.4b show no significant oil trapped between the electrode and piezoelectric layers, demonstrating the good bonding between the layers of the multi-material 3D printed piezoelectric sensors. Figure 6.4cI and 6.4dI show the SEM images taken from the piezoelectric and conductive layers of the conformal non-planar hemisphere. The printed filaments are uniform (width = ~0.495 mm) and no significant porosities between filaments is observed. Figure 6.4cII and 6.4dII show the transverse cross-section view and Figure 6.4cIII and 6.4dIII show the enlarged view of the deposited filaments. For both composites, the PZT or Ag fillers are well-dispersed in the PDMS matrix without any significant agglomerations. Figure 6.4e shows the piezoelectric composite spiral cut from the freeform spiral-hexagon. We observed that the diameter of the spiral is uniform (~2.58 mm) and the pitches (~1.91 mm) between the turns are identical.

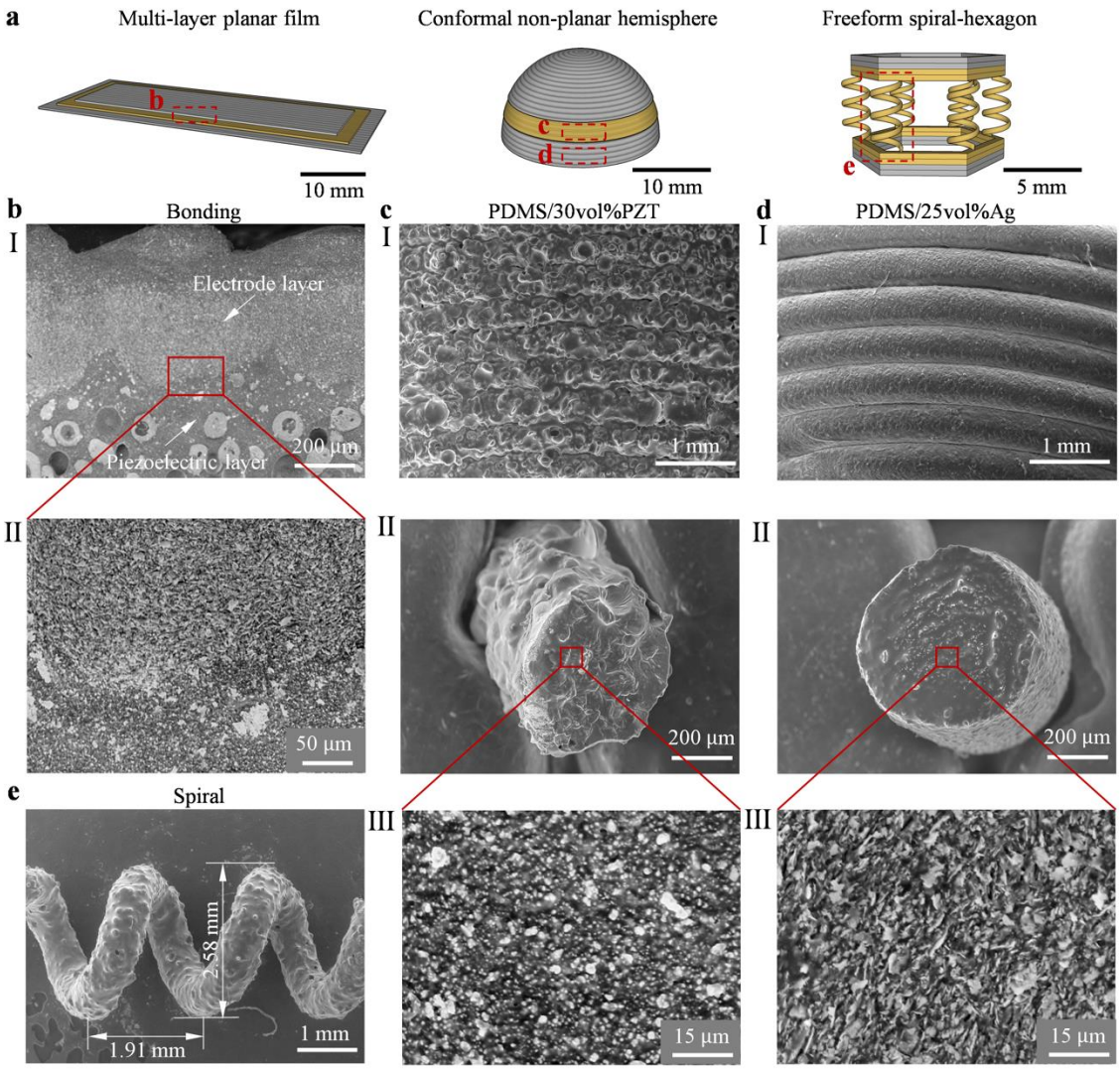

Figure 6.4 SEM images of the multi-material 3D printed flexible piezoelectric composite sensors with integrated electrodes: (a) The locations of the samples cut from the three types of piezoelectric sensors. (b) SEM images of the bonding between the conductive and piezoelectric layers of the multi-layer planar film (II: enlarged view). (c) PDMS/30vol%PZT piezoelectric composite: (I) surface view of the sample cut from the piezoelectric layer of the conformal non-planar hemisphere, (II) transverse cross-section view of the deposited filaments (III: enlarged view). (d) PDMS/25vol%Ag conductive composite: (I) surface view of the sample cut from the conductive layer of the conformal non-planar hemisphere, (II) transverse cross-section view of the deposited filaments (III: enlarged view). (e) A PDMS/30vol%PZT composite spiral cut from the freeform spiral-hexagon.

As listed in Table 6.3, we conducted the stretching or compression tests to evaluate the piezoelectric performance of the three demonstrators. The piezoelectric performance as a function of cyclic axial elongation was investigated by extending the multi-layer planar film to 10% strain at a crosshead speed of 1 mm/s and relaxing it back to a zero-strain condition at the same rate. This stretching-relaxation cycle was repeated three times. The obtained peak-to-peak voltage (V_{pp}) is 41.14 $\pm$ 0.316 mV (Figure 6.5a). The piezoelectric signal is consistent with the applied strain with negligible variation. For the conformal non-planar hemisphere (Figure 6.5b), we pressed it with a finger three times. The V_{pp} is 152.43 $\pm$ 4.624 mV. We observed that during the press-release cycle, the upper part of the hemisphere is dented inside but it will bounce out automatically, which shows its great potential to be used as a battery-free flexible button. To validate the durability of the freeform spiral-hexagon, we compressed it with a displacement of 2 mm at 8 Hz for 800 cycles using a shaker (Figure 6.5c). The V_{pp} of the early cycles is 88.53 $\pm$ 1.224 mV and the V_{pp} of the late cycles is 86.39 $\pm$ 1.145 mV, which indicates that the freeform spiral-hexagon still shows favorable stability for more than 800 cycles without much degradation.

Table 6.3 Comparison of the developed three demonstrators.

Type	Multi-layer planar film	Conformal non-planar hemisphere	Freeform spiral-hexagon
Mode	Tension	Bending	Compression and shearing
V_{pp} (mV)	41.14 $\pm$ 0.316 Strain = 10%	152.43 $\pm$ 4.624 Under three finger taps	86.39 $\pm$ 1.145 Displacement = 2 mm 8 Hz for 800 cycles
Weight (g)	3.52 $\pm$ 0.079	3.69 $\pm$ 0.069	0.45 $\pm$ 0.060
Advantages	Extensible	More flexible Spring back behavior More compact than planar design	More complex shape Spring back behavior Freedom in design Easily tailor the stiffness

Results are mean $\pm$ 95% confidence interval obtained from three replicates.

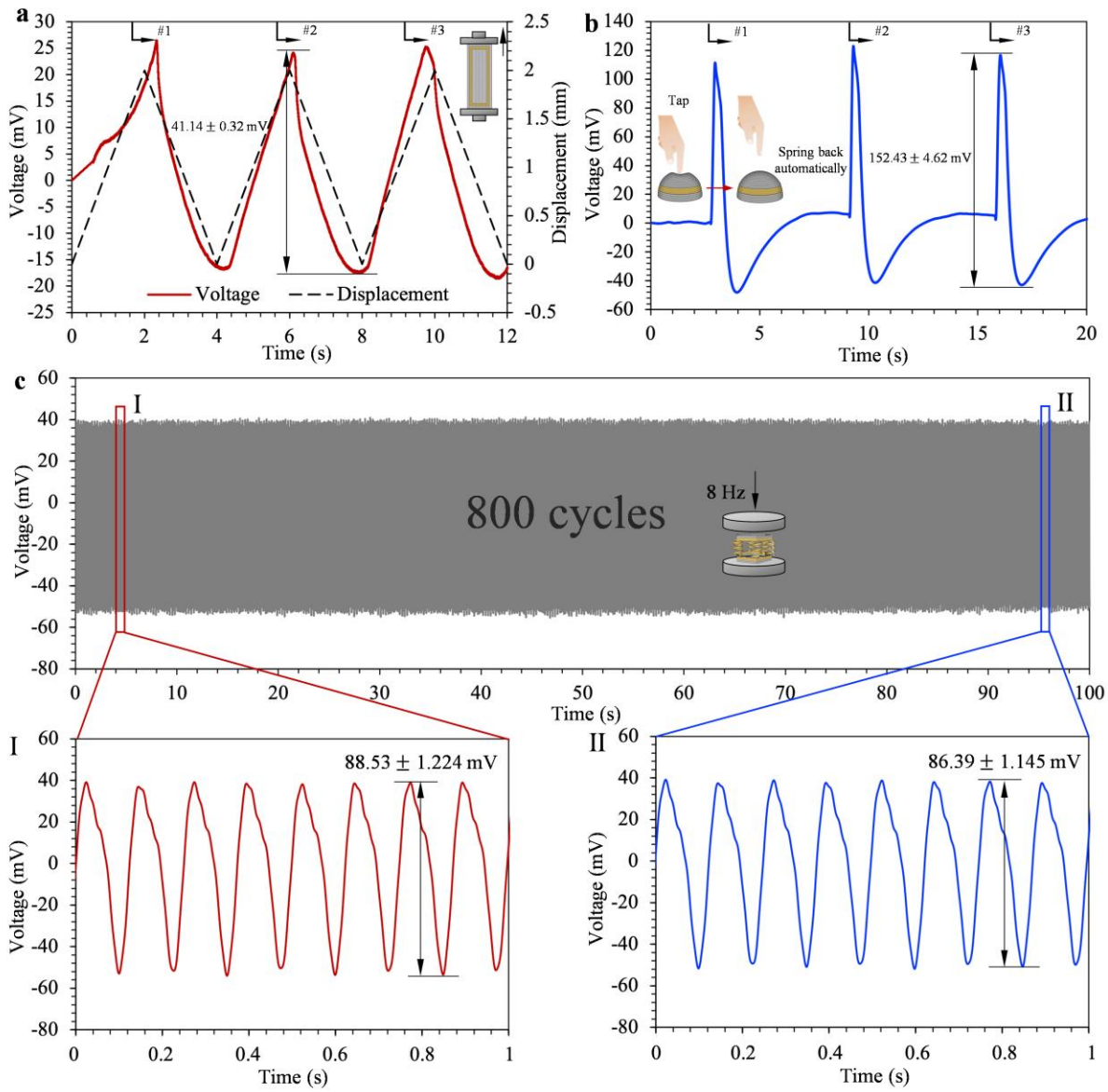

Figure 6.5 Piezoelectric characterizations of the multi-material 3D printed flexible piezoelectric composite sensors with integrated electrodes: (a) Stretching-relaxation test on the multi-layer planar film ($50 \times 20 \times 1.5$ mm^3) with a strain up to 10% for 3 cycles. (b) Finger tapping test on the conformal non-planar hemisphere for 3 cycles. (c) Cyclic compression test on the freeform spiral-hexagon with a displacement of 2 mm at 8 Hz for 800 cycles (Inset figures I: for the early 8 cycles; II: for the late 8 cycles.).

6.3 Conclusion

We have successfully implemented a multi-material DIW layer-by-layer, conformal (non-planar) and freeform 3D printing technique to fabricate flexible piezoelectric composite sensors with integrated electrodes inside a supporting fluid. The characterization on the tailored piezoelectric PDMS/30vol%PZT and conductive PDMS/25vol%Ag composite inks show that the inks meet the functional requirements to be used as the piezoelectric sensing element and the electrodes while being 3D printable (e.g., shear-thinning behavior) and mechanically flexible (up to 30% elongation at break for both composites). The mineral oil/6%(w/v) fumed silica nanoparticle suspension with the proper yield stress is found to successfully facilitate freeform 3D printing of the developed piezoelectric and conductive inks. For demonstration, three types of multi-material 3D printed piezoelectric composite structures are fabricated and tested to assess their piezoelectric performance. For example, under cyclic compression test at 8 Hz, the V_{pp} of a freeform spiral-hexagon is 86.39 ± 1.145 mV for more than 800 cycles. The novel approach presented here provides new opportunities to fabricate flexible piezoelectric devices with integrated electrodes in other complex freeform geometries, using a clean (i.e., without the need of toxic solvents) and eco-friendly (i.e., the supporting fluid is reusable) fabrication process, with high shape fidelity, easy operational mode (i.e., multi-material DIW 3D printing in a single manufacturing process).

6.4 Experimental section

6.4.1 Materials

Inks: A mixture of two different types of PDMS was used as the matrix for both piezoelectric and conductive composite inks. The low viscosity PDMS (SYLGARD™ 184) and high viscosity PDMS (DOWSIL™ SE 1700) were purchased from DOW Chemical (USA). The weight ratio of the high to low viscosity PDMS is 7:3, as recommended by the relevant works[55,56] and the base to curing agent is 10:1, as recommended by the supplier. The addition of low viscosity PDMS acted on the dilution of high viscosity PDMS for desired rheological properties. The PZT powder (APC 850: ~500 nm, spherical particles) was purchased from APC International, Ltd (USA) as the filler for piezoelectric composite ink. The silver flake powder (47MR-10F: purity = 99.95%, 2–5 µm)

was purchased from Inframat Advanced Materials (USA) as the filler for the conductive composite ink.

Supporting fluid: The fumed silica powder (AEROSIL® R805: 200 m^2/g) was purchased from Evonik Industries (USA) and the mineral oil (CAS: 8042-47-5) from VWR (Canada).

6.4.2 Manufacturing process

Inks and supporting fluid preparation process

Piezoelectric ink: 30 vol% PZT powder was added into the PDMS system and blended in a mixer (DAC 515-200 SE, FlackTeck SpeedMixer®) at 2750 rpm for 1 min.

Conductive ink: 25 vol% Ag flakes was added into the mixture of PDMS and blended in the mixer at 2750 rpm for 1 min. Then the two types of inks were loaded into two syringe barrels (3 mL, Nordson EFD), respectively.

Supporting fluid: 6% (w/v) fumed silica was blended with mineral oil in a 60 ml mixer container at 2750 rpm for 1 min. Then, the supporting fluid rested for 10 min and was remixed for 1 min to remove the bubbles (Figure 6.6a).

Multi-material DIW 3D printing of piezoelectric composite structures with integrated electrodes

Multi-material 3D printing process was carried out using a three-axis motion-controlled gantry system (Aerotech, USA) equipped with two independent DIW printing heads: one DIW head was assigned for the piezoelectric ink and the other DIW head was assigned for the conductive ink (Figure 6.6b). A custom-made pneumatic-driven controller (Mëkanic, Canada) was used to apply the pressure on the piston of dispensing apparatus (EFD 7×, Nordson) to push the ink inside the syringe out of the nozzle along the print paths. In the case of multi-layer planar films and conformal non-planar hemispheres, print paths were initially generated with Simplify3D slicing software and then translated to the Aerobasic language (i.e., the language of Aerotech) using a robotic simulation software, RoboDK 4.2.4 (RoboDK Inc.). In the case of the freeform spiral-hexagon structure, the print paths were generated using a custom-made MATLAB program and then translated to Aerobasic language using RoboDK. The printing speed was 5 mm/s. The applied pressure was 210 kPa for the conductive ink and 280 kPa for the piezoelectric ink, respectively. The dispensing needle of the nozzle had a 38 mm-long stainless steel tip (Nordson EFD) and an

inner diameter of 0.6 mm. The fairly long nozzle was selected to ensure that the nozzle can reach the bottom section of the supporting fluid. The layer height was 0.5 mm.

Post-curing process

The fabricated piezoelectric structures were cured in an oven at 80°C for 24 h (Figure 6.6c). We selected 80°C because the boiling point of the mineral oil is 100°C. Then the cured structures were taken out of the supporting fluid and washed with soap and water to remove the residue of mineral oil and fumed silica and dried at ambient temperature. The supporting fluid can be reused multiple times.

Poling process

To orient the dipole moments of the fabricated piezoelectric composite structures in the desired direction, a contact poling setup was built (Figure 6.6d). The setup consists of three parts: a custom-made poling station, a high voltage power supply (ES60kV negative, 10 Watt, Gamma High Voltage Research, Inc.) and a hot plate (Thermo Scientific™ SuperNuova+™, Fisher Scientific). In the poling station, an aluminum plate was grounded, and a negative high voltage cable from the high voltage power supply was connected to a copper rod (~3 mm in diameter) as the poling head. An aluminum plate ($20 \times 20 \times 2$ mm^3) was inserted between the copper rod of the poling head and top surface of the element to achieve a good distribution of electric field. During the poling process, we put the piezoelectric structure between the poling head and bottom aluminum plate, and polarized it under an electric field of 5 kV/mm at 80°C for 60 min. After the poling process, the piezoelectric structure was cooled down to room temperature before removing the electric field to reduce the misalignment of dipole moments. The piezoelectric structure was finally washed with soap and water to remove the residue of silicone oil and dried at ambient temperature.

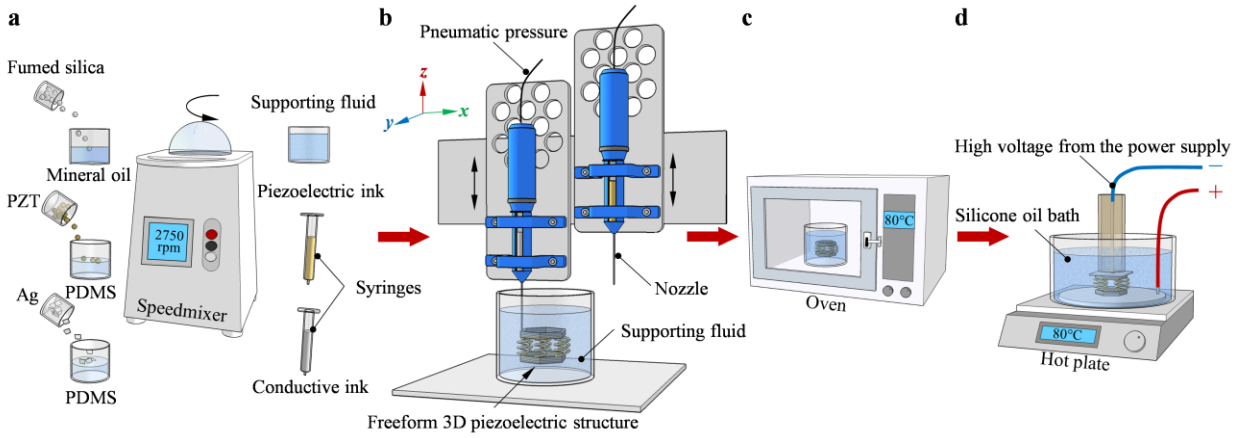

Figure 6.6 Fabrication of multi-material freeform 3D printed flexible piezoelectric composite sensors with integrated electrodes in the mineral oil/fumed silica supporting fluid: (a) Inks and supporting fluid preparation process using a mixer (piezoelectric composite ink: PDMS/30vol%PZT; conductive composite ink: PDMS/25vol%Ag; supporting fluid: mineral oil/6%(w/v) fumed silica). (b) Multi-material freeform 3D printing process in the supporting fluid (freeform spiral-hexagon is shown). (c) Curing process in an oven. (d) Poling process using a custom-made poling station.

6.4.3 Scanning electron microscopy (SEM) and optical characterization

The SEM observations (TM3030, Hitachi, USA) were used to investigate the microstructures of the following samples: (1) the bonding section of the printed piezoelectric and electrode layers cut from the multi-layer planar film; (2) printed layers, and (3) printed filaments cut from the conformal non-planar hemisphere structure (PDMS/30vol%PZT and PDMS/25vol%Ag composites); (4) a PDMS/30vol%PZT composite spiral cut from the freeform spiral-hexagon. A razor blade was used to cut all these samples. Samples were then sputtered with a 10 nm layer of chrome before the imaging analysis. The imaging analyses were performed at a 5 kV voltage supply. Filler dispersion was analysed based on the cross-sectional view of the sample (3) which were fractured manually in the liquid nitrogen. The dimensions of the three types of piezoelectric composite structures were measured using an optical microscope (BX-61, Olympus) and software ImageJ (version 1.8.0_172).

6.4.4 Piezoelectric coefficient characterization

A d_{33} meter (YE2730, Sinocera Piezotronics, Inc.) was used to characterize the piezoelectric coefficient - d_{33} of the PDMS/PZT composite films (50 × 10 × 0.5 mm^3) made of different PZT volume fractions (10, 20, 30 and 40 vol%). Five specimens of each type were tested approximately one day after the poling process to measure a stabilized value.

6.4.5 Piezoelectric test on the multi-material 3D printed structures

The piezoelectric performances of the three types of piezoelectric composite structures with integrated electrodes were evaluated through the following three tests: (1) stretching-relaxation test (axial strain = 10%, 3 cycles) of the multi-layer planar film (50 × 20 × 1.5 mm^3) was carried out using an MTS Insight machine at a crosshead speed of 1 mm/s. The gage length is 20 mm; (2) finger tapping test was conducted on the conformal non-planar hemisphere by three gentle finger taps; (3) cyclic compression tests (displacement = 2 mm, f = 8 Hz, 800 cycles) of the freeform spiral-hexagon using a shaker (2060E, Mode Shop Inc.).

The open-circuit piezoelectric voltages were collected using a charge amplifier (Piezo Lab Amplifier, MEAS Specialties) in a voltage mode. The voltage data was acquired with an NI-9239 data acquisition system attached to a USB carrier NI-9162 (National Instruments) and recorded using a custom LabVIEW interface.

6.4.6 Conductivity measurement on the conductive composite films

The electrical resistance (R) was measured using a four-point resistance measuring card (PCI-4070 card, National 312 Instruments). The R of the printed PDMS/Ag composite films (50 × 10 × 0.5 mm^3) with different Ag volume fractions (20, 25 and 30 vol%) were measured. Five specimens of each volume fraction were tested.

6.4.7 Rheological characterization

Shear viscosities of PDMS/PZT, PDMS/Ag composite inks and mineral oil/fumed silica supporting fluid with different filler concentrations were measured using a controlled stress rheometer (MCR 502, Anton Paar) equipped with parallel plates at shear rates between 0.001 to

100 s^{-1} at ambient temperature. Also, the process-related viscosity measurements on the PDMS/PZT and PDMS/Ag inks were conducted by capillary flow analysis following the procedure described in [57]. Different concentrations of PDMS/PZT (10, 20 and 30 vol%) and PDMS/Ag inks (25 and 30 vol%) were extruded on glass substrates under five different applied pressures at a print head motion velocity of 0.5 mm/s. The extruded filaments (~60 mm long) were weighed using a high-precision balance (GH-202, A&D Engineering Inc.). Their weight was used to obtain the volumetric flow rates for calculating the process-related apparent viscosity of the various inks. Three specimens of each type were tested.

6.4.8 Mechanical characterization

The tensile stiffness and elongation at break (%) characterization of the one-layer piezoelectric PDMS/PZT composite rectangular films ($50 \times 10 \times 0.5$ mm^3) with three PZT volume fractions (10, 20 and 30 vol%), and the one-layer conductive PDMS/Ag composite rectangular films ($50 \times 10 \times 0.5$ mm^3) with two Ag volume fractions (25 and 30 vol%) were carried out using an MTS Insight electromechanical testing system (820-050-EL) with a 100 N load cell at a crosshead speed of 50 mm/min. The gauge length was 25 mm. The test was carried out based on ASTM Standard D882 - 12. Five specimens of each type were tested.

6.5 Supporting information

6.5.1 Images of the supporting behavior of the supporting fluid with different fumed silica concentrations

Figure 6.7 shows the images of a single filament printed in the supporting fluid with three different fumed silica concentrations: 5%, 6% and 7% (w/v). The printed filament in the 5% (w/v) supporting fluid were dragged along the movement of the dispensing needle. The printed filament was well-supported in the 6% (w/v) supporting fluid. There was crevasse in the 7% (w/v) supporting fluid caused by the movement of the needle.

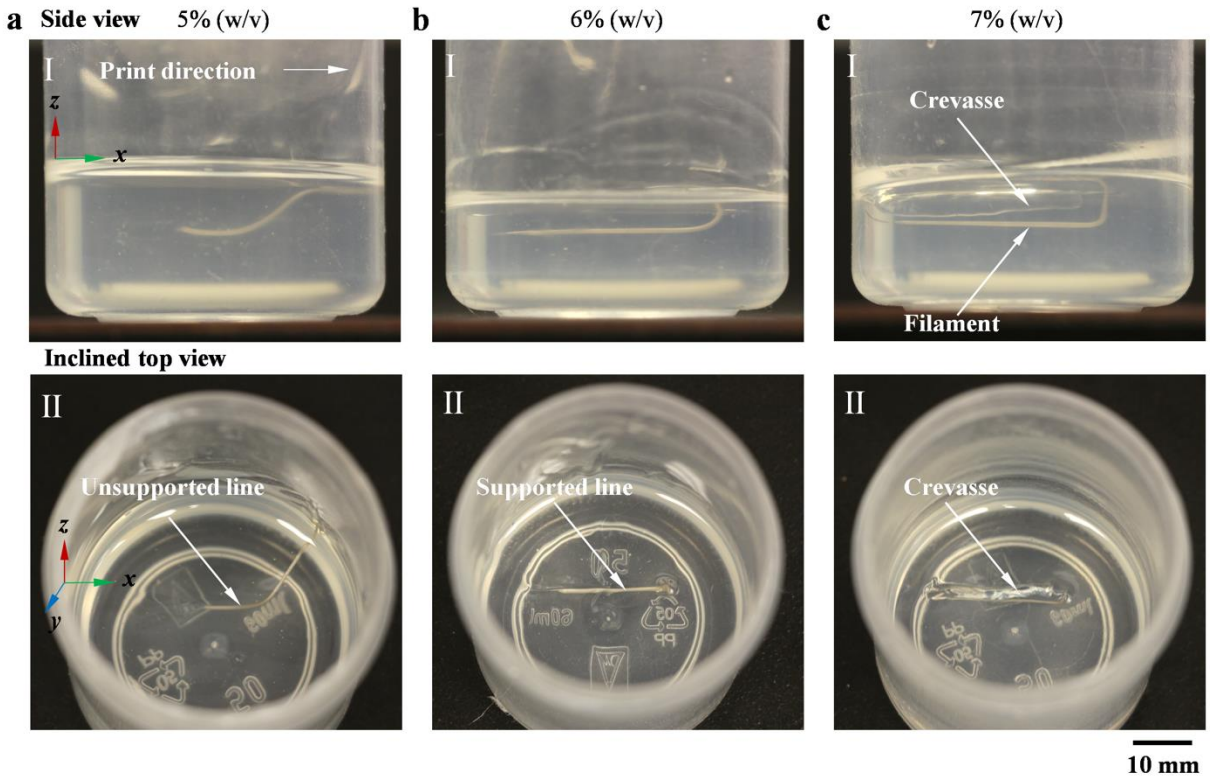

Figure 6.7 Images (I: side view and II: inclined top view) of a single PDMS/25vol%Ag conductive composite filament printed in the supporting fluid with different fumed silica concentrations: (a) 5, (b) 6 and (c) 7% (w/v), respectively.

6.5.2 Dimension measurement of the three piezoelectric composite structures

Table 6.4 Dimension measurement of the printed structures (Unit: mm). Error bars indicate 95% confidence interval of the mean obtained from three replicates.

Type		Multi-layer film	Hemisphere	Spiral-hexagon
Length (or diameter or side length)	Measurement	48.93 ± 0.086	20.26 ± 0.094	4.86 ± 0.089
	Model	50	20	5
	Relative error (%)	2.1	1.3	2.8

	Measurement	20.35 ± 0.062	_	_
Width	Model	20	_	_
	Relative error (%)	1.8	_	_
	Measurement	1.55 ± 0.023	10.11 ± 0.034	10.35 ± 0.043
Height	Model	1.5	10	10
	Relative error (%)	3.3	1.1	3.5

Acknowledgement

We acknowledge support from National Science and Engineering Research Council (NSERC), Discovery program (#RGPIN-4566-2018) and the Department of National Defence (DND) (Grant#: DGDND-2018-00011). Mrs. Rui Tao also acknowledges the financial support that she received through a scholarship from the China Scholarship Council (CSC). We are thankful for the help from our colleague Dr. Rouhollah Farahani for helping with the manuscript, Dr. Iee Lee Hia for the assistance in SEM characterization, Mr. Jean-François Chauvette and Mrs. Chi Zhang for the advice on the analysis of rheological properties, Dr. Mohammad Rafiee and Mr. Abraham Bhérer-Constant for the training on Aerotech gantry system.

References

(1) Wang, Z.; Yuan, X.; Yang, J.; Huan, Y.; Gao, X.; Li, Z.; Wang, H.; Dong, S. 3D-Printed Flexible, Ag-Coated PNN-PZT Ceramic-Polymer Grid-Composite for Electromechanical Energy Conversion. Nano Energy 2020, 73 (January), 104737.

(2) Rovisco, A.; Dos Santos, A.; Cramer, T.; Martins, J.; Branquinho, R.; Águas, H.; Fraboni, B.; Fortunato, E.; Martins, R.; Igreja, R.; Barquinha, P. Piezoelectricity Enhancement of Nanogenerators Based on PDMS and ZnSnO3Nanowires through Microstructuration. ACS Appl. Mater. Interfaces 2020, 12 (16), 18421–18430.

(3) Zheng, Q.; Zhang, H.; Mi, H.; Cai, Z.; Ma, Z.; Gong, S. High-Performance Flexible Piezoelectric Nanogenerators Consisting of Porous Cellulose Nanofibril (CNF)/Poly(Dimethylsiloxane) (PDMS) Aerogel Films. Nano Energy 2016, 26, 504–512.

(4) Shi, K.; Huang, X.; Sun, B.; Wu, Z.; He, J.; Jiang, P. Cellulose/BaTiO 3 Aerogel Paper Based Flexible Piezoelectric Nanogenerators and the Electric Coupling with Triboelectricity. Nano Energy 2019, 57 (November 2018), 450–458.

(5) Ren, X.; Fan, H.; Zhao, Y.; Liu, Z. Flexible Lead-Free BiFeO3/PDMS-Based Nanogenerator as Piezoelectric Energy Harvester. ACS Appl. Mater. Interfaces 2016, 8 (39), 26190–26197.

(6) Quinsaat, J. E. Q.; de Wild, T.; Nüesch, F. A.; Damjanovic, D.; Krämer, R.; Schürch, G.; Häfliger, D.; Clemens, F.; Sebastian, T.; Dascalu, M.; Opris, D. M. Stretchable Piezoelectric Elastic Composites for Sensors and Energy Generators. Compos. Part B Eng. 2020, 198 (April).

(7) Luo, C.; Hu, S.; Xia, M.; Li, P.; Hu, J.; Li, G.; Jiang, H.; Zhang, W. A Flexible Lead-Free BaTiO3/PDMS/C Composite Nanogenerator as a Piezoelectric Energy Harvester. Energy Technol. 2018, 6 (5), 922–927.

(8) Cui, H.; Hensleigh, R.; Yao, D.; Maurya, D.; Kumar, P.; Kang, M. G.; Priya, S.; Zheng, X. Three-Dimensional Printing of Piezoelectric Materials with Designed Anisotropy and Directional Response. Nat. Mater. 2019, 18 (3), 234–241.

(9) Yao, D.; Cui, H.; Hensleigh, R.; Smith, P.; Alford, S.; Bernero, D.; Bush, S.; Mann, K.; Wu, H. F.; Chin-Nieh, M.; Youmans, G.; Zheng, X. Achieving the Upper Bound of Piezoelectric Response in Tunable, Wearable 3D Printed Nanocomposites. Adv. Funct. Mater. 2019, 29 (42).

(10) Chen, S.; Tan, W. S.; Bin Juhari, M. A.; Shi, Q.; Cheng, X. S.; Chan, W. L.; Song, J. Freeform 3D Printing of Soft Matters: Recent Advances in Technology for Biomedical Engineering. Biomed. Eng. Lett. 2020, 10 (4), 453–479.

(11) Farahani, R. D.; Chizari, K.; Therriault, D. Three-Dimensional Printing of Freeform Helical Microstructures: A Review. Nanoscale 2014, 6 (18), 10470–10485.

(12) Bausch, N.; Dawkins, D. P.; Frei, R. Inspired - Advances in Conformal Printing: 3D Printing onto Unknown Uneven Surfaces. IEEE/ASME Int. Conf. Adv. Intell. Mechatronics, AIM 2017, 430–435.

(13) Patrício, S. G.; Sousa, L. R.; Correia, T. R.; Gaspar, V. M.; Pires, L. S.; Luís, J. L.; Oliveira, J. M.; Mano, J. F. Freeform 3D Printing Using a Continuous Viscoelastic Supporting Matrix. Biofabrication 2020, 12 (3).

(14) Barry, R. A.; Shepherd, R. F.; Hanson, J. N.; Nuzzo, R. G.; Wiltzius, P.; Lewis, J. A. Direct-Write Assembly of 3D Hydrogel Scaffolds for Guided Cell Growth. Adv. Mater. 2009, 21 (23), 2407–2410.

(15) Wu, Q.; Therriault, D.; Heuzey, M. C. Processing and Properties of Chitosan Inks for 3D Printing of Hydrogel Microstructures. ACS Biomater. Sci. Eng. 2018, 4 (7), 2643–2652.

(16) Wei, H.; Cauchy, X.; Navas, I. O.; Abderrafai, Y.; Chizari, K.; Sundararaj, U.; Liu, Y.; Leng, J.; Therriault, D. Direct 3D Printing of Hybrid Nanofiber-Based Nanocomposites for Highly Conductive and Shape Memory Applications. ACS Appl. Mater. Interfaces 2019, 11 (27), 24523–24532.

(17) Farahani, R. D.; Dalir, H.; Le Borgne, V.; Gautier, L. A.; El Khakani, M. A.; Lévesque, M.; Therriault, D. Direct-Write Fabrication of Freestanding Nanocomposite Strain Sensors. Nanotechnology 2012, 23 (8).

(18) Lebel, L. L.; Aissa, B.; El Khakani, M. A.; Therriault, D. Ultraviolet-Assisted Direct-Write Fabrication of Carbon Nanotube/Polymer Nanocomposite Microcoils. Adv. Mater. 2010, 22 (5), 592–596.

(19) Herren, B.; Saha, M. C.; Altan, M. C.; Liu, Y. Development of Ultrastretchable and Skin Attachable Nanocomposites for Human Motion Monitoring via Embedded 3D Printing. Compos. Part B Eng. 2020, 200 (June), 108224.

(20) Li, F.; Smejkal, P.; Macdonald, N. P.; Guijt, R. M.; Breadmore, M. C. One-Step Fabrication of a Microfluidic Device with an Integrated Membrane and Embedded Reagents by Multimaterial 3D Printing. Anal. Chem. 2017, 89 (8), 4701–4707.

(21) Grosskopf, A. K.; Truby, R. L.; Kim, H.; Perazzo, A.; Lewis, J. A.; Stone, H. A. Viscoplastic Matrix Materials for Embedded 3D Printing. ACS Appl. Mater. Interfaces 2018, 10 (27), 23353–23361.

(22) Truby, R. L.; Wehner, M.; Grosskopf, A. K.; Vogt, D. M.; Uzel, S. G. M.; Wood, R. J.; Lewis, J. A. Soft Somatosensitive Actuators via Embedded 3D Printing. Adv. Mater. 2018, 30 (15), 1–8.

(23) Zhao, J.; Hussain, M.; Wang, M.; Li, Z.; He, N. Embedded 3D Printing of Multi-Internal Surfaces of Hydrogels. Addit. Manuf. 2020, 32 (January), 101097.

(24) Hua, W.; Mitchell, K.; Raymond, L.; Godina, B.; Zhao, D.; Zhou, W.; Jin, Y. Fluid Bath-Assisted 3D Printing for Biomedical Applications: From Pre: From Postprinting Stages. ACS Biomater. Sci. Eng. 2021, 7 (10), 4736–4756.

(25) O'Bryan, C. S.; Bhattacharjee, T.; Hart, S.; Kabb, C. P.; Schulze, K. D.; Chilakala, I.; Sumerlin, B. S.; Sawyer, W. G.; Angelini, T. E. Self-Assembled Micro-Organogels for 3D Printing Silicone Structures. Sci. Adv. 2017, 3 (5).

(26) Pellet, C.; Cloitre, M. The Glass and Jamming Transitions of Soft Polyelectrolyte Microgel Suspensions. Soft Matter 2016, 12 (16), 3710–3720.

(27) Jin, Y.; Song, K.; Gellermann, N.; Huang, Y. Printing of Hydrophobic Materials in Fumed Silica Nanoparticle Suspension. ACS Appl. Mater. Interfaces 2019.

(28) Jin, Y.; Compaan, A.; Chai, W.; Huang, Y. Functional Nanoclay Suspension for Printing-Then-Solidification of Liquid Materials. ACS Appl. Mater. Interfaces 2017, 9 (23), 20057–20066.

(29) Jin, Y.; Xiong, R.; Antonelli, P. J.; Long, C. J.; McAleer, C. W.; Hickman, J. J.; Huang, Y. Nanoclay Suspension-Enabled Extrusion Bioprinting of Three-Dimensional Soft Structures. J. Manuf. Sci. Eng. 2021, 143 (12), 1–9.

(30) Karyappa, R.; Hashimoto, M. Freeform Polymer Precipitation in Microparticulate Gels. ACS Appl. Polym. Mater. 2021, 3 (2), 908–919.

(31) Bhattacharjee, T.; Zehnder, S. M.; Rowe, K. G.; Jain, S.; Nixon, R. M.; Sawyer, W. G.; Angelini, T. E. Writing in the Granular Gel Medium. Sci. Adv. 2015, 1 (8), 1–7.

(32) Abdollahi, S.; Markvicka, E. J.; Majidi, C.; Feinberg, A. W. 3D Printing Silicone Elastomer for Patient-Specific Wearable Pulse Oximeter. Adv. Healthc. Mater. 2020, 9 (15).

(33) Jin, Y.; Compaan, A.; Bhattacharjee, T.; Huang, Y. Granular Gel Support-Enabled Extrusion of Three-Dimensional Alginate and Cellular Structures. Biofabrication 2016, 8 (2).

(34) Yang, S.; Tang, H.; Feng, C.; Shi, J.; Yang, J. The Research on Multi-Material 3D Vascularized Network Integrated Printing Technology. Micromachines 2020, 11 (3), 1–13.

(35) Basu, A.; Saha, A.; Goodman, C.; Shafranek, R. T.; Nelson, A. Catalytically Initiated Gel-in-Gel Printing of Composite Hydrogels. ACS Appl. Mater. Interfaces 2017, 9 (46), 40898–40904.

(36) Cidonio, G.; Cooke, M.; Glinka, M.; Dawson, J. I.; Grover, L.; Oreffo, R. O. C. Printing Bone in a Gel: Using Nanocomposite Bioink to Print Functionalised Bone Scaffolds. Mater. Today Bio 2019, 4 (September), 100028.

(37) Compaan, A. M.; Song, K.; Huang, Y. Gellan Fluid Gel as a Versatile Support Bath Material for Fluid Extrusion Bioprinting. ACS Appl. Mater. Interfaces 2019.

(38) Mirdamadi, E.; Tashman, J. W.; Shiwarski, D. J.; Palchesko, R. N.; Feinberg, A. W. FRESH 3D Bioprinting a Full-Size Model of the Human Heart. ACS Biomater. Sci. Eng. 2020, 6 (11), 6453–6459.

(39) Jeon, O.; Lee, Y. Bin; Jeong, H.; Lee, S. J.; Wells, D.; Alsberg, E. Individual Cell-Only Bioink and Photocurable Supporting Medium for 3D Printing and Generation of Engineered Tissues with Complex Geometries. Mater. Horizons 2019, 6 (8), 1625–1631.

(40) Hinton, T. J.; Hudson, A.; Pusch, K.; Lee, A.; Feinberg, A. W. 3D Printing PDMS Elastomer in a Hydrophilic Support Bath via Freeform Reversible Embedding. ACS Biomater. Sci. Eng. 2016, 2 (10), 1781–1786.

(41) Afghah, F.; Altunbek, M.; Dikyol, C.; Koc, B. Preparation and Characterization of Nanoclay-Hydrogel Composite Support-Bath for Bioprinting of Complex Structures. Sci. Rep. 2020, 10 (1), 1–13.

(42) Colly, A.; Marquette, C.; Courtial, E. J. Poloxamer/Poly(Ethylene Glycol) Self-Healing Hydrogel for High-Precision Freeform Reversible Embedding of Suspended Hydrogel. Langmuir 2021, 37 (14), 4154–4162.

(43) Tang, E. L.; Wang, L.; Han, Y. F. Space Debris Positioning Based on Two-Dimensional PVDF Piezoelectric Film Sensor. Adv. Sp. Res. 2019, 63 (8), 2410–2421.

(44) Zhu, P.; Wang, Y.; Wang, Y.; Mao, H.; Zhang, Q.; Deng, Y. Flexible 3D Architectured Piezo/Thermoelectric Bimodal Tactile Sensor Array for E-Skin Application. Adv. Energy Mater. 2020, 10 (39), 1–8.

(45) Cho, G.; Jeong, K.; Paik, M. J.; Kwun, Y.; Sung, M. Performance Evaluation of Textile-Based Electrodes and Motion Sensors for Smart Clothing. IEEE Sens. J. 2011, 11 (12), 3183–3193.

(46) Mokhtari, F.; Shamshirsaz, M.; Latifi, M.; Foroughi, J. Nanofibers-Based Piezoelectric Energy Harvester for Self-Powered Wearable Technologies. Polymers (Basel). 2020, 12 (11), 1–15.

(47) Haghiashtiani, G.; Greminger, M. A. Fabrication, Polarization, and Characterization of PVDF Matrix Composites for Integrated Structural Load Sensing. 2015.

(48) Lu, X.; Qu, H.; Skorobogatiy, M. Piezoelectric Microstructured Fibers via Drawing of Multimaterial Preforms. Sci. Rep. 2017, 7 (1), 1–12.

(49) Lu, X.; Qu, H.; Skorobogatiy, M. Piezoelectric Micro- and Nanostructured Fibers Fabricated from Thermoplastic Nanocomposites Using a Fiber Drawing Technique: Comparative Study and Potential Applications. ACS Nano 2017, 11 (2), 2103–2114.

(50) Bodkhe, S.; Noonan, C.; Gosselin, F. P.; Therriault, D. Coextrusion of Multifunctional Smart Sensors. Adv. Eng. Mater. 2018, 20 (10), 1800206.

(51) Xu, C.; Quinn, B.; Lebel, L. L.; Therriault, D.; L'espérance, G. Multi-Material Direct Ink Writing (DIW) for Complex 3D Metallic Structures with Removable Supports. ACS Appl. Mater. Interfaces 2019, 11 (8), 8499–8506.

(52) Kokkinis, D.; Schaffner, M.; Studart, A. R. Multimaterial Magnetically Assisted 3D Printing of Composite Materials. Nat. Commun. 2015, 6.

(53) Skylar-Scott, M. A.; Mueller, J.; Visser, C. W.; Lewis, J. A. Voxelated Soft Matter via Multimaterial Multinozzle 3D Printing. Nature 2019, 575 (7782), 330–335.

(54) Yan, A.; Yuan, X.; Li, Z.; Yang, J.; Ren, K.; Dong, S. 3D-Printed Flexible, Multilayered Ceramic-Polymer Composite Grid with Integrated Structural-Self-Sensing Function. Sensors Actuators A Phys. 2021, 332, 113187.

(55) Liu, C.; Le, L.; Zhang, M.; Ding, J. Tunable Large-Scale Compressive Strain Sensor Based on Carbon Nanotube/Polydimethylsiloxane Foam Composites by Additive Manufacturing. Adv. Eng. Mater. 2021, 2101337, 1–9.

(56) Ozbolat, V.; Dey, M.; Ayan, B.; Povilianskas, A.; Demirel, M. C.; Ozbolat, I. T. 3D Printing of PDMS Improves Its Mechanical and Cell Adhesion Properties. ACS Biomater. Sci. Eng. 2018, 4 (2), 682–693.

(57) Bruneaux, J.; Therriault, D.; Heuzey, M. C. Micro-Extrusion of Organic Inks for Direct-Write Assembly. J. Micromechanics Microengineering 2008, 18 (11).

(58) Augusto, P. E. D.; Falguera, V.; Cristianini, M.; Ibarz, A. Rheological Behavior of Tomato Juice: Steady-State Shear and Time-Dependent Modeling. Food Bioprocess Technol. 2012, 5 (5), 1715–1723.

(59) Beran, T.; Mulholland, T.; Henning, F.; Rudolph, N.; Osswald, T. A. Nozzle Clogging Factors during Fused Filament Fabrication of Spherical Particle Filled Polymers. Addit. Manuf. 2018, 23 (May), 206–214.

(60) Brzeski, D.; Hia, I. L.; Chauvette, J. F.; Farahani, R. D.; Piccirelli, N.; Ross, A.; Therriault, D. Design of Thermoset Composites for High-Speed Additive Manufacturing of Lightweight Sound Absorbing Micro-Scaffolds. Addit. Manuf. 2021, 47 (May), 102245.

(61) Chauvette, J. F.; Brzeski, D.; Hia, I. L.; Farahani, R. D.; Piccirelli, N.; Therriault, D. High-Speed Multinozzle Additive Manufacturing and Extrusion Modeling of Large-Scale Microscaffold Networks. Addit. Manuf. 2021, 47 (June), 10229.

CHAPTER 7 GENERAL DISCUSSION

As discussed in Chapter 4, the piezoelectric F_β of the as-printed PVDF films is pretty low (~39%). The stretching process increases the F_β to 65% (R=4), while it limits the possibilities of 3D printing PVDF-based piezoelectric devices with complex 3D shapes. PVDF can be indirectly used in two ways: one way is to print a multi-layer film with alternating piezoelectric PVDF layers and conductive composite layers, followed by stretching the precursor to a thinner multi-layer PVDF film with electrodes. The other way is to be used as the flexible matrix of the piezoceramic composite materials, the resulting piezoelectric performance of the composite will be the sum of PVDF and high piezoelectric ceramic fillers. PVDF is a common choice for fabricating flexible piezoelectric devices but has limited stretchability. Flexible and stretchable piezoelectric devices are in great demand for wearable sensors and energy harvesters, soft robots and smart artificial skins. Therefore, in Chapter 5 and 6, we developed flexible polymer-based piezoceramic composites (TPU/PZT and PDMS/PZT) and fabricated them into 3D piezoelectric devices with integrated electrodes through multi-material 3D printing technology.

In Chapter 5, we designed and fabricated four types of 3D flexible piezoelectric composite lattices with integrated electrodes (and one fully dense solid for benchmark) using the developed piezoelectric composite filament and the commercial conductive composite filament through a multi-material FFF 3D printing technique. The piezoelectric voltage output of the OT lattice and FD sample under the same maximum applied force were compared by experimental and FEA methods. The simulation results are a little different from the experimental results most probably due to the manufacturing defects arises from the additive manufacturing process. The print quality could be improved in two ways: one way is to improve the diameter uniformity of the developed piezoelectric composite filament by in-situ monitoring the filament fabrication process using a triple-axis laser scanner. Another way is to improve the capability of the FFF 3D printer to print flexible and stretchable filament. For example, we can add force sensors to control the clamping force of the two filament feeding screws on the FFF 3D printer. Adding filament guide tubes between the feeding screws to the FFF nozzle can also reduce the possibilities of the flexible filament being bent in the loading process. In addition, OT lattice has twice higher voltage output than FD sample. Other possible piezoelectric lattice structures could be investigated and compared with the high-performance OT lattice. The size of the designed lattices is $4 \times 4 \times 1$ unit cell in this

work. We could further stack them in the vertical direction to make thicker lattices with potentially higher piezoelectric performance. The OT multi-material piezoelectric composite shoe sole developed in this work have the advantages of high flexibility, high voltage output and durability. This concept can be applied to other piezoelectric sensing and energy harvesting applications such as energy harvesting mattresses and keyboards, robot hands with the function of force detection. A proper energy harvesting circuit can be built to enhance the energy harvesting efficiency of the shoe sole. The energy harvesting efficiency of the shoe sole can be then evaluated by charging batteries or powering wearable devices using the collected energy. However, the multi-material FFF 3D printing technique finds difficulties in fabricating conformal or freeform piezoelectric structures, which have led to the supporting fluid-assisted multi-material freeform DIW 3D printing technology as discussed in Chapter 6.

The multi-layer planar, conformal non-planar and freeform flexible piezoelectric composite sensors with integrated electrodes developed in Chapter 6 are a first proof-of-concept of introducing multi-material freeform and conformal 3D printing technique using a supporting fluid to fabricate piezoelectric materials. The freeform spiral-hexagon was tested in compression mode, other operating modes (shearing and tension) can be investigated. Geometrically more complex freeform structures should be designed to optimize the piezoelectric performance while being lightweight. Supporting fluid-assisted 3D printing technique has been widely used in biomedical fields to fabricate complex-shaped human tissues and organs. There is a great potential to add a third printing head for printing biomaterials in our method to achieve embedded 3D printing of piezoelectric sensors in human tissues. In addition, supporting fluid-assisted multi-material 3D printing technique could be extended to fabricate other smart materials such as triboelectric materials and shape memory alloys along with piezoelectric materials to achieve multifunctionalities. There are also some limitations of this technique: (1) The thermoset-based PDMS composite inks need to be heated in the oven for 24 hours for curing. The curing process is time-consuming. (2) The silver flakes for making the conductive ink are expensive. Other cheaper conductive particles can be incorporated into polymer such as carbon-based conductive fillers (e.g., carbon black and multi-walled carbon nanotubes). (3) The size of the structures is limited by the size of the supporting fluid container and the volume of the syringe (3 ml).

CHAPTER 8 CONCLUSION AND RECOMMANDATIONS

8.1 Conclusion

In this dissertation, the 3D flexible piezoelectric composite devices with co-fabricated electrodes were successfully fabricated through multi-material 3D printing technology. The following conclusions are drawn from this work:

- In Chapter 4, the piezoelectric coefficient d_{33} of the FFF printed PVDF films has been enhanced to ~10-100 times higher than the reported values [80], [119] by means of the proper stretching and poling processes. The good piezoelectric performance (d_{33} = 7.29 pC/N) of the fabricated PVDF films were demonstrated in two sensing applications (cantilever bending and compression test), and one energy harvesting application. However, the stretching process limits the possibilities of using PVDF to fabricate 3D piezoelectric devices with complex geometries through multi-material 3D printing technique.
- In Chapter 5, four types of 3D piezoelectric composite lattices (and one fully dense solid used as a benchmark) with electrodes were designed and fabricated with the developed TPU/30vol%PZT composite filament and the commercial conductive TPU/carbon black composite filament based on multi-material FFF 3D printing technique. The piezoelectric voltage output of the lattices was compared by means of experimental and FEA results. Under the same maximum applied force, OT lattice generated twice as much voltage as the FD sample. As a demonstrator, an original multi-material OT piezoelectric composite shoe sole was fabricated and tested by human stomping test and the cyclic compression test. The test results show that the multi-material OT piezoelectric composite shoe sole has a high voltage output, flexibility and durability.
- In Chapter 6, a multi-layer planar film, a conformal non-planar hemisphere, and a freeform spiral-hexagon piezoelectric composite structures with electrodes were fabricated through the multi-material DIW freeform 3D printing process in a supporting fluid. The PDMS/30vol%PZT and PDMS/25vol%Ag composite inks with the appropriate rheological, mechanical, piezoelectric or conductive properties were developed. The developed mineral oil/fumed silica microgel supporting fluid with the proper yield stress

stably supported the printed filaments. The piezoelectric performance of the three demonstrators were consistent with the applied stress under tension or compression tests.

8.2 Recommendations

Future research is recommended in the following aspects:

- Although the geometry of the FFF printed PVDF is limited to 2D film as a result of the stretching step in Chapter 4, we could further print multi-layer film with alternating piezoelectric PVDF layers and conductive composite layers using the multi-material FFF 3D printing technique and then stretch it to a thinner piezoelectric multi-layer film with electrodes. To solve the problem that the electrodes of the commercial PVDF films tend to wear or detach from the PVDF films with time.
- The filament quality of the developed piezoelectric TPU/PZT composite filament in Chapter 5 could be further improved by controlling the diameter uniformity of the filament in the filament extrusion process using a triple-axis laser micrometer.
- The FFF 3D printer should be improved for printing flexible or stretchable filaments, for example, by adding force sensor to control the shear force between the two filament feeding gears.
- Other potential lattice configurations could be designed by simulation and fabricated to be compared with the four types of 3D piezoelectric composite lattices discussed in Chapter 5.
- Finite element analysis (FEA) method using tools such as ANSYS should be developed in which users can design, amplify, or suppress any piezoelectric coefficient modes of 3D piezoelectric structures for specific application, not only in compression or tension modes, could also in shear or bending modes.
- The multi-material freeform 3D printing technique developed in Chapter 6 could be further used to achieve embedded 3D printing of piezoelectric devices with electrodes in the components as assembled structures.

- The developed stretchable piezoelectric composite materials can be fabricated into other functional structures. For example, to be used as the material of the microstructured fibers with sacrificial bonds and coiling loops in the “spider web” developed by Zou *et al.* So the piezoelectric composite-based microstructured fibers can not only dissipate the impact energy, but also generate a real-time piezoelectric signal to indicate the locations of the impact without the need of external power source [120].
- The developed multi-material 3D printing technique could be further used to fabricate other smart materials along with the piezoelectric materials, for example, shape memory materials, triboelectric materials to achieve multifunctional properties in the future advanced materials.

REFERENCES

[1] H. Cui *et al.*, "Three-dimensional printing of piezoelectric materials with designed anisotropy and directional response," *Nat. Mater.*, vol. 18, no. 3, pp. 234–241, Mar. 2019.

[2] M. Yoichi, "Applications of piezoelectric actuator," *Spec. Issue Electron. Devices*, pp. 82–86.

[3] C. Dagdeviren *et al.*, "Recent progress in flexible and stretchable piezoelectric devices for mechanical energy harvesting, sensing and actuation," *Extrem. Mech. Lett.*, vol. 9, pp. 269–281, Dec. 2016.

[4] I. Choudhry, H. R. Khalid, and H. K. Lee, "Flexible piezoelectric transducers for energy harvesting and sensing from human kinematics," *ACS Appl. Electron. Mater.*, vol. 2, no. 10, pp. 3346–3357, 2020.

[5] "Piezo Film Sensors Technical Manual."

[6] Z. Wang *et al.*, "3D-printed flexible, Ag-coated PNN-PZT ceramic-polymer grid-composite for electromechanical energy conversion," *Nano Energy*, vol. 73, no. January, p. 104737, 2020.

[7] J. E. Q. Quinsaat *et al.*, "Stretchable piezoelectric elastic composites for sensors and energy generators," *Compos. Part B Eng.*, vol. 198, no. April, 2020.

[8] C. Luo *et al.*, "A Flexible Lead-Free BaTiO3/PDMS/C Composite Nanogenerator as a Piezoelectric Energy Harvester," *Energy Technol.*, vol. 6, no. 5, pp. 922–927, 2018.

[9] Q. Zheng, H. Zhang, H. Mi, Z. Cai, Z. Ma, and S. Gong, "High-performance flexible piezoelectric nanogenerators consisting of porous cellulose nanofibril (CNF)/poly(dimethylsiloxane) (PDMS) aerogel films," *Nano Energy*, vol. 26, pp. 504–512, 2016.

[10] T. J. Hinton, A. Hudson, K. Pusch, A. Lee, and A. W. Feinberg, "3D Printing PDMS Elastomer in a Hydrophilic Support Bath via Freeform Reversible Embedding," *ACS Biomater. Sci. Eng.*, vol. 2, no. 10, pp. 1781–1786, 2016.

[11] X. Lu, H. Qu, and M. Skorobogatiy, "Piezoelectric Micro- and Nanostructured Fibers Fabricated from Thermoplastic Nanocomposites Using a Fiber Drawing Technique:

Comparative Study and Potential Applications," *ACS Nano*, vol. 11, no. 2, pp. 2103–2114, 2017.

[12] P. Zhu, Y. Wang, Y. Wang, H. Mao, Q. Zhang, and Y. Deng, "Flexible 3D Architectured Piezo/Thermoelectric Bimodal Tactile Sensor Array for E-Skin Application," *Adv. Energy Mater.*, vol. 10, no. 39, pp. 1–8, 2020.

[13] G. Petrossian, C. J. Hohimer, and A. Ameli, "Highly-loaded thermoplastic polyurethane/lead zirconate titanate composite foams with low permittivity fabricated using expandable microspheres," *Polymers (Basel).*, vol. 11, no. 2, 2019.

[14] A. Sotov, A. Kantyukov, A. Popovich, and V. Sufiiarov, "LCD-SLA 3D printing of BaTiO3 piezoelectric ceramics," *Ceram. Int.*, vol. 47, no. 21, pp. 30358–30366, 2021.

[15] D. Yao *et al.*, "Achieving the Upper Bound of Piezoelectric Response in Tunable, Wearable 3D Printed Nanocomposites," *Adv. Funct. Mater.*, vol. 1903866, p. 1903866, 2019.

[16] S. Bodkhe, P. S. M. Rajesh, F. P. Gosselin, and D. Therriault, "Simultaneous 3D Printing and Poling of PVDF and Its Nanocomposites," *ACS Appl. Energy Mater.*, vol. 1, no. 6, pp. 2474–2482, Jun. 2018.

[17] S. Bodkhe, G. Turcot, F. P. Gosselin, and D. Therriault, "One-Step Solvent Evaporation-Assisted 3D Printing of Piezoelectric PVDF Nanocomposite Structures," *ACS Appl. Mater. Interfaces*, vol. 9, no. 24, pp. 20833–20842, Jun. 2017.

[18] H. Kim, T. Fernando, M. Li, Y. Lin, and T.-L. B. Tseng, "Fabrication and characterization of 3D printed BaTiO 3 /PVDF nanocomposites," 2018.

[19] N. W. S. Pinargote, A. Smirnov, N. Peretyagin, A. Seleznev, and P. Peretyagin, "Direct ink writing technology (3d printing) of graphene-based ceramic nanocomposites: A review," *Nanomaterials*, vol. 10, no. 7, pp. 1–48, 2020.

[20] S. Bodkhe, C. Noonan, F. P. Gosselin, and D. Therriault, "Coextrusion of Multifunctional Smart Sensors," *Adv. Eng. Mater.*, vol. 20, no. 10, p. 1800206, Oct. 2018.

[21] X. Zhou *et al.*, "All 3D-printed stretchable piezoelectric nanogenerator with non-protruding kirigami structure," *Nano Energy*, vol. 72, p. 104676, 2020.

[22] A. Yan, X. Yuan, Z. Li, J. Yang, K. Ren, and S. Dong, "3D-printed flexible, multilayered

ceramic-polymer composite grid with integrated structural-self-sensing function," *Sensors Actuators A Phys.*, vol. 332, p. 113187, 2021.

[23] J. Curie and P. Curie, "Development by Pressure of Polar Electricity in Hemihedral Crystals with Inclined Faces," *Bull. la Société minéralogique Fr.*, vol. 3, no. 4, pp. 90–93, 1880.

[24] G. Lippmann, "Principe de la conservation de l'elecricit´e," *Ann Chemie e Phys.*, vol. 24, no. 145, 1881.

[25] J. Curie and P. Curie, "Contractions et dilatations produites par des tensions dans les cristaux hémièdres à faces inclinées," *Comptes Rendus*, vol. 93, pp. 1337–1140, 1881.

[26] L. Huo, D. Chen, Q. Kong, H. Li, and G. Song, "Smart washer - A piezoceramic-based transducer to monitor looseness of bolted connection," *Smart Mater. Struct.*, vol. 26, no. 2, 2017.

[27] Y. jun Li, G. cong Wang, H. yong Cui, S. kun Cao, and X. yu Wang, "Dynamic characteristics and optimization research on PVDF piezoelectric film force sensor for steel ball cold heading machine," *ISA Trans.*, 2019.

[28] C. Covaci and A. Gontean, "Piezoelectric energy harvesting solutions: A review," *Sensors (Switzerland)*, vol. 20, no. 12, pp. 1–37, 2020.

[29] M. Noor-A-Alam, H. J. Kim, and Y. H. Shin, "Dipolar polarization and piezoelectricity of a hexagonal boron nitride sheet decorated with hydrogen and fluorine," *Phys. Chem. Chem. Phys.*, vol. 16, no. 14, pp. 6575–6582, 2014.

[30] B. Li, J. E. Blendell, and K. J. Bowman, "Temperature-dependent poling behavior of lead-free BZT-BCT piezoelectrics," *J. Am. Ceram. Soc.*, vol. 94, no. 10, pp. 3192–3194, 2011.

[31] P. Fulay and J.-K. Lee, "Ferroelectrics, Piezoelectrics, and Pyroelectrics," *Electron. Magn. Opt. Mater.*, pp. 317–380, 2021.

[32] A. Jbaily and R. W. Yeung, "Piezoelectric devices for ocean energy: a brief survey," *J. Ocean Eng. Mar. Energy*, vol. 1, no. 1, pp. 101–118, 2015.

[33] L. H. Kang, D. O. Lee, and J. H. Han, "A measurement method for piezoelectric material properties under longitudinal compressive stress - A compression test method for thin piezoelectric materials," *Meas. Sci. Technol.*, vol. 22, no. 6, 2011.

[34] I. Kanno, “Piezoelectric thin films for MEMS applications,” *Integr. Microsystems Electron. Photonics, Biotechnol.*, pp. 679–698, 2017.

[35] A. American and N. Standard, “An American National Standard: IEEE Standard on Piezoelectricity,” *IEEE Trans. Sonics Ultrason.*, vol. 31, no. 2, pp. 8–10, 1984.

[36] E. R. Cholleti, “A Review on 3D printing of piezoelectric materials,” *IOP Conf. Ser. Mater. Sci. Eng.*, vol. 455, no. 1, 2018.

[37] “Physical and piezoelectric properties of APC Matreials technical report: APC 850,” 2020.

[38] J. Gao, D. Xue, W. Liu, C. Zhou, and X. Ren, “Recent progress on BaTiO3-based piezoelectric ceramics for actuator applications,” *Actuators*, vol. 6, no. 3, 2017.

[39] L. Xie, G. Wang, C. Jiang, F. Yu, and X. Zhao, “Properties and applications of flexible poly(Vinylidene fluoride)-based piezoelectric materials,” *Crystals*, vol. 11, no. 6, pp. 1–21, 2021.

[40] H. Kawai, “The Piezoelectricity of Poly (vinylidene Fluoride),” *Jpn. J. Appl. Phys.*, vol. 8, no. 7, p. 975, 1969.

[41] W. W. Lando and J. B. Doll, “The polymorphism of poly(vinylidene fluoride) IV. The structure of high-pressure-crystallized poly(vinylidene fluoride),” *J. Macromol. Sci. Part B*, vol. 4, no. 4, pp. 889–896, 1970.

[42] V. Sencadas, R. Gregorio, and S. Lanceros-Méndez, “α to β phase transformation and microestructural changes of PVDF films induced by uniaxial stretch,” *J. Macromol. Sci. Part B Phys.*, vol. 48, no. 3, pp. 514–525, 2009.

[43] R. Gregorio, “Determination of the α, β, and γ crystalline phases of poly(vinylidene fluoride) films prepared at different conditions,” *J. Appl. Polym. Sci.*, vol. 100, no. 4, pp. 3272–3279, 2006.

[44] Z. Yin, B. Tian, Q. Zhu, and C. Duan, “Characterization and application of PVDF and its copolymer films prepared by spin-coating and langmuir-blodgett method,” *Polymers (Basel).*, vol. 11, no. 12, 2019.

[45] Q. Gao and J. I. Scheinbeim, “Dipolar intermolecular interactions, structural development, and electromechanical properties in ferroelectric polymer blends of nylon-11 and

poly(vinylidene fluoride),” *Macromolecules*, vol. 33, no. 20, pp. 7564–7572, 2000.

[46] N. A. Shepelin *et al.*, “New developments in composites, copolymer technologies and processing techniques for flexible fluoropolymer piezoelectric generators for efficient energy harvesting,” *Energy Environ. Sci.*, vol. 12, no. 4, pp. 1143–1176, 2019.

[47] D. Vatansever, E. Siores, and T. Shah, “Alternative Resources for Renewable Energy: Piezoelectric and Photovoltaic Smart Structures,” p. 13, 2012.

[48] S. H. Lee, Y. C. Choi, M. S. Kim, K. M. Ryu, and Y. G. Jeong, “Fabrication and Characterization of Piezoelectric Composite Nanofibers Based on Poly(vinylidene fluoride-co-hexafluoropropylene) and Barium Titanate Nanoparticle,” *Fibers Polym.*, vol. 21, no. 3, pp. 473–479, 2020.

[49] R. Gregorio, and M. Cestari, “Effect of crystallization temperature on the crystalline phase content and morphology of poly(vinylidene fluoride),” *J. Polym. Sci. Part B Polym. Phys.*, vol. 32, no. 5, pp. 859–870, 1994.

[50] P. Martins, A. C. Lopes, and S. Lanceros-Mendez, “Electroactive phases of poly(vinylidene fluoride): Determination, processing and applications,” *Prog. Polym. Sci.*, vol. 39, no. 4, pp. 683–706, 2014.

[51] T. L. Jordan and N. Langley, “Piezoelectric Ceramics Characterization,” 2001.

[52] K. R. Rashmi, A. Jayarama, N. Navin Bappalige, and R. Pinto, “A Review on Vibration Based Piezoelectric Energy Harvesters,” *Sahyadri Int. J. Res.*, vol. 3, no. 1, pp. 47–56, 2017.

[53] M. Kimura, A. Ando, and Y. Sakabe, “2 - Lead zirconate titanate-based piezo-ceramics Author links open overlay panel,” *Adv. piezoelectric Mater.*, pp. 89–110, 2010.

[54] T. Siponkoski, M. Nelo, H. Jantunen, and J. Juuti, “A printable P(VDF-TrFE)-PZT Composite with Very High Piezoelectric Coefficient,” *Appl. Mater. Today*, vol. 20, 2020.

[55] W. K. Sakamoto, P. Marin-Franch, and D. K. Das-Gupta, “Characterization and application of PZT/PU and graphite doped PZT/PU composite,” *Sensors Actuators, A Phys.*, vol. 100, no. 2–3, pp. 165–174, 2002.

[56] S. K. Sharma, H. Gaur, M. Kulkarni, G. Patil, B. Bhattacharya, and A. Sharma, “PZT-PDMS composite for active damping of vibrations,” *Compos. Sci. Technol.*, vol. 77, pp. 42–51,

2013.

[57] I. Babu and G. de With, “Highly flexible piezoelectric 0-3 PZT-PDMS composites with high filler content,” *Compos. Sci. Technol.*, vol. 91, pp. 91–97, 2014.

[58] K. K. Sappati and S. Bhadra, “Flexible Piezoelectric 0-3 PZT-PDMS Thin Film for Tactile Sensing,” *IEEE Sens. J.*, vol. 20, no. 9, pp. 4610–4617, 2020.

[59] N. Chamankar, R. Khajavi, A. A. Yousefi, A. Rashidi, and F. Golestanifard, “A flexible piezoelectric pressure sensor based on PVDF nanocomposite fibers doped with PZT particles for energy harvesting applications,” *Ceram. Int.*, vol. 46, no. 12, pp. 19669–19681, 2020.

[60] A. Yazdani, H. D. Manesh, and S. M. Zebarjad, “Piezoelectric properties and damping behavior of highly loaded PZT/polyurethane particulate composites,” *Ceram. Int.*, 2021.

[61] O. B. Ferreira, R. S. Venkat, J. Adam, and C. Boller, “Development of the Fabrication Process and Characterization of Piezoelectric BaTiO 3 / Epoxy Composite Used for Coated Ultrasonic Transducer Patterns in Structural Health Monitoring,” no. January, pp. 1–9, 2016.

[62] Y. Zhuang *et al.*, “Flexible composites with Ce-doped BaTiO3/P(VDF-TrFE) nanofibers for piezoelectric device,” *Compos. Sci. Technol.*, vol. 200, no. July, p. 108386, 2020.

[63] Y. Yang *et al.*, “Flexible piezoelectric pressure sensor based on polydopamine-modified BaTiO3/PVDF composite film for human motion monitoring,” *Sensors Actuators, A Phys.*, vol. 301, p. 111789, 2020.

[64] H. Park, D. Y. Hyeon, M. Jung, K. Il Park, and J. Park, “Piezoelectric BaTiO3 microclusters and embossed ZnSnO3 microspheres-based monolayer for highly-efficient and flexible composite generator,” *Compos. Part B Eng.*, vol. 203, no. September, p. 108476, 2020.

[65] S. H. Shin, Y. H. Kim, M. H. Lee, J. Y. Jung, and J. Nah, “Hemispherically aggregated BaTiO3 nanoparticle composite thin film for high-performance flexible piezoelectric nanogenerator,” *ACS Nano*, vol. 8, no. 3, pp. 2766–2773, 2014.

[66] E. L. Tang, L. Wang, and Y. F. Han, “Space debris positioning based on two-dimensional PVDF piezoelectric film sensor,” *Adv. Sp. Res.*, vol. 63, no. 8, pp. 2410–2421, 2019.

[67] G. Cho, K. Jeong, M. J. Paik, Y. Kwun, and M. Sung, “Performance evaluation of textile-

based electrodes and motion sensors for smart clothing," *IEEE Sens. J.*, vol. 11, no. 12, pp. 3183–3193, 2011.

[68] F. Mokhtari, M. Shamshirsaz, M. Latifi, and J. Foroughi, "Nanofibers-based piezoelectric energy harvester for self-powered wearable technologies," *Polymers (Basel).*, vol. 12, no. 11, pp. 1–15, 2020.

[69] G. Haghiashtiani and M. A. Greminger, "Fabrication, polarization, and characterization of PVDF matrix composites for integrated structural load sensing," 2015.

[70] S. Das Mahapatra *et al.*, "Piezoelectric Materials for Energy Harvesting and Sensing Applications: Roadmap for Future Smart Materials," *Adv. Sci.*, vol. 8, no. 17, 2021.

[71] E. Nilsson, A. Lund, C. Jonasson, C. Johansson, and B. Hagström, "Poling and characterization of piezoelectric polymer fibers for use in textile sensors," *Sensors Actuators, A Phys.*, vol. 201, pp. 477–486, 2013.

[72] R. Subir, *An introduction to high voltage engineering*, 2nd Ed. 2013.

[73] S. K. Mahadeva, J. Berring, K. Walus, and B. Stoeber, "Effect of poling time and grid voltage on phase transition and piezoelectricity of poly(vinyledene fluoride) thin films using corona poling," *J. Phys. D. Appl. Phys.*, vol. 46, no. 28, 2013.

[74] G. W. Day, C. A. Hamilton, R. L. Peterson, R. J. Phelan, and L. O. Mullen, "Effects of poling conditions on responsivity and uniformity of polarization of PVF2 pyroelectric detectors," *Appl. Phys. Lett.*, vol. 24, no. 10, pp. 456–458, 1974.

[75] J. Diani and K. Gall, "Finite Strain 3D Thermoviscoelastic Constitutive Model," *Society*, pp. 1–10, 2006.

[76] Y. P. Su, L. N. Sim, X. Li, H. G. L. Coster, and T. H. Chong, "Anti-fouling piezoelectric PVDF membrane: Effect of morphology on dielectric and piezoelectric properties," *J. Memb. Sci.*, vol. 620, no. July 2020, p. 118818, 2021.

[77] R. Senthil Kumar, T. Sarathi, K. K. Venkataraman, and A. Bhattacharyya, "Enhanced piezoelectric properties of polyvinylidene fluoride nanofibers using carbon nanofiber and electrical poling," *Mater. Lett.*, vol. 255, p. 126515, 2019.

[78] B. Mohammadi, A. A. Yousefi, and S. M. Bellah, "Effect of tensile strain rate and elongation

on crystalline structure and piezoelectric properties of PVDF thin films," *Polym. Test.*, vol. 26, no. 1, pp. 42–50, 2007.

[79] E. Gross, E. Gross, and E. Gross, "Simultaneous stretching and corona poling of PVDF films," *J. Phys. D. Appl. Phys.*, no. 1969, pp. 261–281, 1990.

[80] D. A. Porter, T. V. T. Hoang, and T. A. Berfield, "Effects of in-situ poling and process parameters on fused filament fabrication printed PVDF sheet mechanical and electrical properties," *Addit. Manuf.*, vol. 13, pp. 81–92, 2017.

[81] A. Kumar and M. M. Perlman, "Simultaneous stretching and corona poling of PVDF and P(VDF-TriFE) films. II," *J. Phys. D. Appl. Phys.*, vol. 26, no. 3, pp. 469–473, 1993.

[82] Y. Huan, Y. Liu, and Y. Yang, "Simultaneous Stretching and Static Electric Field Poling of Poly(vinylidene fluoride-hexafluoropropylene) Copolymer Films," *Polym. Eng. Sci.*, pp. 1630–1633, 2007.

[83] S. Eßlinger, P. Neumeister, A. Schönecker, M. Hoffman, A. Studer, and M. Hinterstein, "In Situ Neutron Diffraction Studies on Poling of the Hard PZT Ceramic PIC181," *Adv. Eng. Mater.*, vol. 21, no. 7, pp. 1–10, 2019.

[84] D. Waller, T. Iqbal, and A. Safari, "Poling of Lead Zirconate Titanate Ceramics and Flexible Piezoelectric Composites by the Corona Discharge Technique," *J. Am. Ceram. Soc.*, vol. 72, no. 2, pp. 322–324, 1989.

[85] K. Arlt and M. Wegener, "Piezoelectric PZT / PVDF-copolymer 0-3 composites: Aspects on film preparation and electrical poling," *IEEE Trans. Dielectr. Electr. Insul.*, vol. 17, no. 4, pp. 1178–1184, 2010.

[86] S. Bairagi and S. W. Ali, "A hybrid piezoelectric nanogenerator comprising of KNN/ZnO nanorods incorporated PVDF electrospun nanocomposite webs," *Int. J. Energy Res.*, vol. 44, no. 7, pp. 5545–5563, 2020.

[87] D. A. Porter, T. V. T. Hoang, and T. A. Berfield, "Effects of in-situ poling and process parameters on fused filament fabrication printed PVDF sheet mechanical and electrical properties," *Addit. Manuf.*, vol. 13, pp. 81–92, Jan. 2017.

[88] A. Salimi and A. A. Yousefi, "Conformational changes and phase transformation

mechanisms in PVDF solution-cast films," *J. Polym. Sci. Part B Polym. Phys.*, vol. 42, no. 18, pp. 3487–3495, 2004.

[89] T. Lei, L. Yu, L. Wang, F. Yang, and D. Sun, "Predicting polymorphism of electrospun polyvinylidene fluoride membranes by their morphologies," *J. Macromol. Sci. Part B Phys.*, vol. 54, no. 1, pp. 91–101, 2015.

[90] A. N. Nguyen *et al.*, "Spin coating and micro-patterning optimization of composite thin films based on PVDF," *Materials (Basel).*, vol. 13, no. 6, pp. 1–18, 2020.

[91] A. Formhals, "Process and apparatus for preparing artificial threads," 1934.

[92] Z. Andrzej, *Fundamentals of fibre formation: the science of fibre spinning and drawing*. 1976.

[93] Z. H. Liu, C. T. Pan, L. W. Lin, and H. W. Lai, "Piezoelectric properties of PVDF/MWCNT nanofiber using near-field electrospinning," *Sensors Actuators, A Phys.*, vol. 193, pp. 13–24, 2013.

[94] X. X. He *et al.*, "Near-Field Electrospinning: Progress and Applications," *J. Phys. Chem. C*, vol. 121, no. 16, pp. 8663–8678, 2017.

[95] Z. H. Liu, C. T. Pan, L. W. Lin, J. C. Huang, and Z. Y. Ou, "Direct-write PVDF nonwoven fiber fabric energy harvesters via the hollow cylindrical near-field electrospinning process," *Smart Mater. Struct.*, vol. 23, no. 2, 2014.

[96] C. T. Pan *et al.*, "Near-field electrospinning enhances the energy harvesting of hollow PVDF piezoelectric fibers," *RSC Adv.*, vol. 5, no. 103, pp. 85073–85081, 2015.

[97] W. E. King and G. L. Bowlin, "Near-field electrospinning and melt electrowriting of biomedical polymers—progress and limitations," *Polymers (Basel).*, vol. 13, no. 7, pp. 1–23, 2021.

[98] C. T. Pan, K. C. Tsai, S. Y. Wang, C. K. Yen, and Y. L. Lin, "Large-area piezoelectric PVDF fibers fabricated by near-field electrospinning with multi-spinneret structures," *Micromachines*, vol. 8, no. 4, pp. 1–16, 2017.

[99] Z. He, F. Rault, M. Lewandowski, E. Mohsenzadeh, and F. Salaün, "Electrospun PVDF nanofibers for piezoelectric applications: A review of the influence of electrospinning

parameters on the β phase and crystallinity enhancement," *Polymers (Basel).*, vol. 13, no. 2, pp. 1–23, 2021.

[100] H. Na, P. Chen, and S.-C. Wong, "Adhesion Energy of Electrospun PVDF," *Procedia Mater. Sci.*, vol. 1, no. July 2014, pp. 13–18, 2012.

[101] N. Moussaif and G. Groeninckx, "Nanocomposites based on layered silicate and miscible PVDF/PMMA blends: Melt preparation, nanophase morphology and rheological behaviour," *Polymer (Guildf).*, vol. 44, no. 26, pp. 7899–7906, 2003.

[102] S. Men, Z. Gao, R. Wen, J. Tang, and J. M. Zhang, "Effects of annealing time on physical and mechanical properties of PVDF microporous membranes by a melt extrusion-stretching process," *Polym. Adv. Technol.*, vol. 32, no. 6, pp. 2397–2408, 2021.

[103] Y. Bian, R. Liu, X. Huang, J. Hong, H. Huang, and S. Hui, "Design and fabrication of a metal core PVDF fiber for an air flow sensor," *Smart Mater. Struct.*, vol. 24, no. 10, 2015.

[104] X. Lu, H. Qu, and M. Skorobogatiy, "Piezoelectric microstructured fibers via drawing of multimaterial preforms," *Sci. Rep.*, vol. 7, no. 1, pp. 1–12, 2017.

[105] R. L. Hadimani *et al.*, "Continuous production of piezoelectric PVDF fibre for e-textile applications," *Smart Mater. Struct.*, vol. 22, no. 7, 2013.

[106] "Piezoelectricity, APC International, Ltd. https://www.americanpiezo.com/knowledge-center/piezo-theory/piezoelectricity.html." .

[107] V. L. Stuber *et al.*, "Flexible Lead-Free Piezoelectric Composite Materials for Energy Harvesting Applications," *Energy Technol.*, vol. 7, no. 1, pp. 177–185, 2019.

[108] Gokhare Vinod G., Raut D. N., and Shinde D. K., "A Review paper on 3D-Printing Aspects and Various Processes Used in the 3D-Printing ," *Int. J. Eng. Res. Technol.*, vol. 6, no. 06, pp. 953–958, 2017.

[109] Z. Wang *et al.*, "3D-printed flexible, Ag-coated PNN-PZT ceramic-polymer grid-composite for electromechanical energy conversion," *Nano Energy*, vol. 73, no. March, p. 104737, 2020.

[110] H. Kim, F. Torres, Y. Wu, D. Villagran, Y. Lin, and T.-L. Tseng, "Integrated 3D printing and corona poling process of PVDF piezoelectric films for pressure sensor application,"

Smart Mater. Struct., vol. 26, no. 8, p. 085027, 2017.

[111] H. Cui *et al.*, "Three-dimensional printing of piezoelectric materials with designed anisotropy and directional response," *Nat. Mater.*, vol. 18, no. 3, pp. 234–241, Mar. 2019.

[112] H. Kim, T. Fernando, M. Li, Y. Lin, and T. L. B. Tseng, "Fabrication and characterization of 3D printed BaTiO3/PVDF nanocomposites," *J. Compos. Mater.*, vol. 52, no. 2, pp. 197–206, 2018.

[113] C. Lee and J. A. Tarbutton, "Electric Poling-assisted Additive Manufacturing Process for Lead-free Piezoelectric Device Fabrication," *Procedia Manuf.*, vol. 1, pp. 320–326, 2015.

[114] H. Wei *et al.*, "Direct 3D Printing of Hybrid Nanofiber-Based Nanocomposites for Highly Conductive and Shape Memory Applications," *ACS Appl. Mater. Interfaces*, vol. 11, no. 27, pp. 24523–24532, 2019.

[115] Q. Wu, S. Zou, F. P. Gosselin, D. Therriault, and M. C. Heuzey, "3D printing of a self-healing nanocomposite for stretchable sensors," *J. Mater. Chem. C*, vol. 6, no. 45, pp. 12180–12186, 2018.

[116] S. Zou, D. Therriault, and F. P. Gosselin, "Spiderweb-Inspired, Transparent, Impact-Absorbing Composite," *Cell Reports Phys. Sci.*, vol. 1, no. 11, p. 100240, 2020.

[117] V. Truxova, J. Safka, M. Seidl, I. Kovalenko, L. Volesky, and M. Ackermann, "Ceramic 3d printing: Comparison of SLA and DLP technologies," *MM Sci. J.*, vol. 2020, no. June, pp. 3905–3911, 2020.

[118] E. Gkartzou, E. P. Koumoulos, and C. A. Charitidis, "Production and 3D printing processing of bio-based thermoplastic filament," *Manuf. Rev.*, vol. 4, 2017.

[119] H. Kim, "Integrated 3D printing and corona poling process of PVDF piezoelectric films for pressure sensor application," 2017.

[120] S. Zou, D. Therriault, and F. P. Gosselin, "Spiderweb-Inspired, Transparent, Impact-Absorbing Composite," *Cell Reports Phys. Sci.*, vol. 1, no. 11, 2020.